Search for Supersymmetry in opposite-sign same-flavour dilepton events with the CMS detector in proton-proton collisions at $\sqrt{s} = 8$ TeV

Von der Fakultät für Mathematik, Informatik und Naturwissenschaften der RWTH Aachen University zur Erlangung des akademischen Grades eines Doktors der Naturwissenschaften genehmigte Dissertation

vorgelegt von
Jan-Frederik Schulte, M.Sc.
aus Münster

Berichter:
Prof. Dr. Lutz Feld
Prof. Dr. Michael Krämer

Termin der mündlichen Prüfung: xx.xx.2015

Diese Dissertation ist auf den Internetseiten der Hochschulbibliothek online verfügbar.

Zusammenfassung

Abstract

Contents

1. Introduction

2. The Standard Model and its extension to Supersymmetry

2.1. The Standard Model of particle physics

2.2. Motivation for extending the Standard Model and Supersymmetry

2.3. Production of lepton pairs in supersymmetric models

2.4. Kinematic edges in the dilepton invariant mass spectrum

3. Experimental setup

3.1. The CERN Large Hadron Collider

The Large Hadron Collider (LHC) [1], located at CERN near Geneva and stretching far into the french countryside, is capable of colliding protons and lead ions at higher energies than any of its predecessors. Also the instantaneous luminosity delivered to the experiments exceeds that of any previous machine at the energy frontier. It was constructed in the tunnel formerly inhabited by the LEP electron-positron collider in $100\,\mathrm{m}$ depths below the surface with a circumference $27\,\mathrm{km}$. It was designed to collide protons at a centre-of-mass energy of $\sqrt{s} = 14\,\mathrm{TeV}$ with instantaneous luminosities of $10^{34}\,\mathrm{s}^{-1}\mathrm{m}^{-2}$.

The LHC consists of eight arcs, as shown in Figure 3.1, where superconducting dipole magnets are used to provide a magnetic field of up to $8.3\,\mathrm{T}$ at the highest planned energies to bend the charged particles along the curvature of the tunnel, while quadrupole and other specialised magnets are used to focus the beams. In straight segments between these arcs, LHC infrastructure and the experiments are located. The infrastructure components include the cooling facilities necessary to reach a temperature of $1.9\,\mathrm{K}$ around the ring, the superconducting cavities in which the protons are accelerated by standing electromagnetic waves, collimators for beam cleaning and the beam dump, where the beam is ejected from the LHC at the end of fills. In the other four straight segments the beam is brought into collisions, which are studied by the four large experiments at the LHC. Of these, CMS [2] and ATLAS [3] are multi-purpose detectors with a diverse physics program, while ALICE [3] and LHCb [4] are more narrowly focused on heavy ion collisions and flavour physics, respectively.

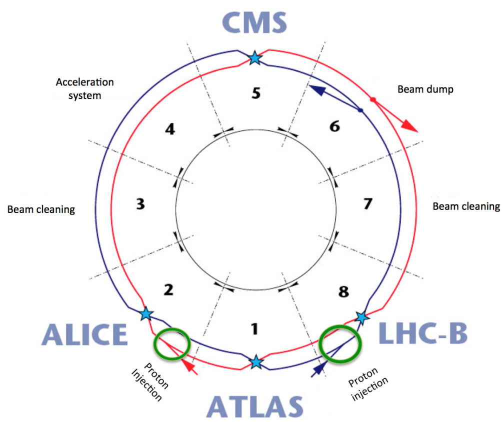

Figure 3.1.: Schematic view of the LHC with its eight arcs. The four interaction points, where the experiments are located, are marked with blue stars. Other important parts of the LHC infrastructure are also indicated [5].

The protons circulating the LHC are injected at an energy of $450\,\mathrm{GeV}$ after running trough a chain of pre-accelerators, the Linac2, the Proton Synchroton Booster (PSB), the Proton Synchrotron (PS) and the Super Proton Synchrotron (SPS). The proton beams are separated into bunches of about 10^{11} particles. Though being $25\,\mathrm{ns}$ by design, corresponding to up to 2808 bunches in the LHC, the smallest spacing between to bunches in time was $50\,\mathrm{ns}$ throughout the running in 2012 and most of 2011. In these running conditions, after three years of running in the years 2010 to 2012, constituting the so called Run I of the LHC, a centre-of-mass energy of $\sqrt{s} = 8\,\mathrm{TeV}$ has been reached. The instantaneous luminosities delivered to the experiments reached a maximum of $7.7 \cdot 10^{33}\,\mathrm{s}^{-1}\mathrm{m}^{-2}$ in late 2012, as can be seen on the left side of Figure 3.2. The integrated luminosity delivered to the CMS experiments in 2012 was $23.3\,\mathrm{fb}^{-1}$, exceeding that of 2011 by almost a factor of four [6], as shown on the right side of Figure 3.2.

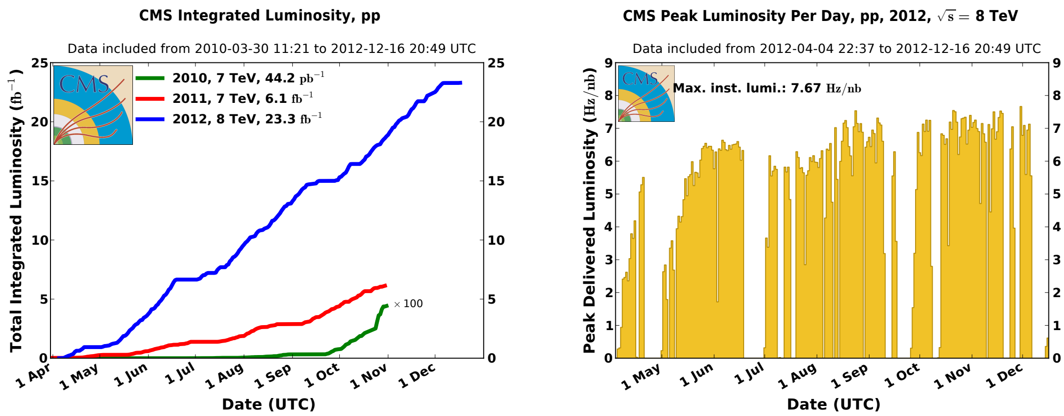

Figure 3.2.: Development of instantaneous (left) and integrated (right) luminosity delivered to the CMS experiment. The left plots shows the results for all three years of data taking, while the right one only shows the 2012 data taking.

3.2. The CMS detector

Located in one of the four intersections of the LHC beams, the CMS detector is designed to measure the resulting collisions to high precision. Key ingredients are a high precision measurements of the properties of single particles as well as a good coverage of the 4π solid angle. The central element of the CMS detector is a superconducting solenoid. Cooled to $4.45\,\mathrm{K}$, it is able to produce a homogeneous magnetic field of $3.8\,\mathrm{T}$, which allows to measure the momentum of charged particle by bending their trajectories. As shown in Figure 3.3, the different components of the detector are layered in cylindrical shapes around the interaction point. The magnet encompasses most of the main subdetectors, namely the tracking system which measures the trajectories of charged particles and the electromagnetic and hadron calorimeters, designed to measure the energy of particles. Located outside of the volume of the solenoid are the iron return yoke and muon detectors. This cylindrical structure is complemented on both sides by endcaps, which close the solid angle in the direction of the beams and are partly located outside the volume of the solenoid. The different components are described in more detail in the following.

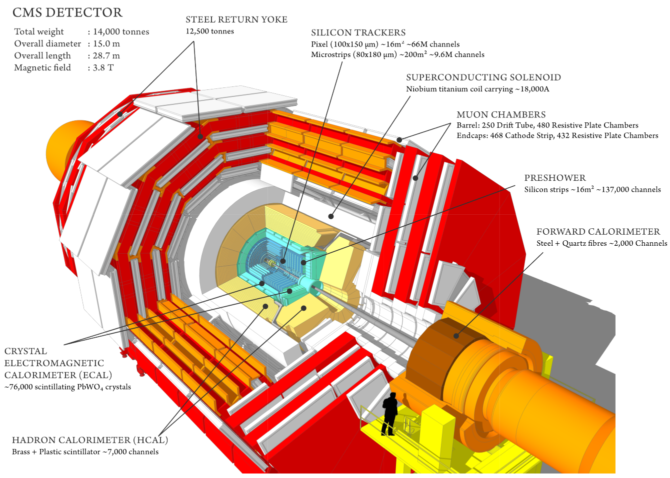

Figure 3.3.: Schematic view of the CMS detector [7]. From the inside out, the tracking system is shown in blue, the electromagnetic calorimeter in green, the hadron calorimeter in light yellow, the superconducting solenoid in white, the return yoke in red and the muon system again in white.

3.2.1. The tracking system

The trajectory of charged particles can be determined by measuring the signal of the ionization they cause when traversing matter. The tracking system of the CMS detector consists of many layers of silicon pixels and strips. Combining the points at which a charged particle traverses the different layers, the trajectory of this particle can be measured. The bending of this trajectory under the influence of the magnetic field allows to determine the momentum of the particle. The tracking system has a diameter of $2.5\,\mathrm{m}$ and a length of $5.8\,\mathrm{m}$, corresponding to a geometric coverage of $|\eta| < 2.5$. The tracking detector consists, as shown in Figure 3.4, of the pixel detector (PIXEL) surrounded by various components of the silicon strip tracker.

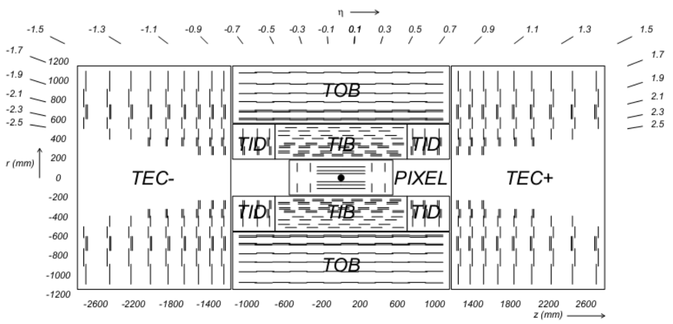

Figure 3.4.: Schematic view of the CMS tracking detector. The innermost part shows the pixel detector (PIXEL), surrounded by the tracker inner barrel (TIB) and tracker inner discs (TID). The outermost parts of the tracking detector are the tracker outer barrel (TOB) and the two tracker endcaps (TEC+ and TEC-).

The silicon pixel detector

The innermost part of the tracking system in the pixel detector, which consists of three layers in the barrel region at radii between $4.4\,\mathrm{cm}$ and $10.2\,\mathrm{cm}$, complemented by two discs perpendicular to the beam axis, located at $|z| = 34.5\,\mathrm{cm}$ and $|z| = 46.5\,\mathrm{cm}$. As the particle density is highest close to the interaction point, a high granularity is needed to maintain a low occupancy of the pixel detector. Therefore the pixel detector consists of roughly 66 million pixels with a combined active area of about $1\,\mathrm{m}^2$. Each pixel has a size of $150 \times 100\,\mathrm{\mu m}^2$. The analogue readout of the pixels allows to combine the measurements of neighbouring pixels, bringing the spatial resolution down to 15 to $20\,\mathrm{\mu m}$. This is especially important for the reconstruction of the interaction vertices and the tagging of the secondary vertices from the decay of b-hadrons.

The silicon strip detector

Further away from the interaction point, between $20\,\mathrm{cm}$ and $116\,\mathrm{cm}$, the granularity of the tracking system is reduced. Silicon strip detectors are used, structured in four layers of the tracker inner barrel (TIB), complemented on each side with three discs of the tracker inner discs (TID). All this is surrounded by the six layers of the tracker outer barrel (TOB). The tracker endcaps (TECs) consist of nine discs each. The individual strips have a length of about $10\,\mathrm{cm}$ and a pitch between $80\,\mathrm{\mu m}$ in the two inner layers of the TIB and $183\,\mathrm{\mu m}$ in the four inner layers of the TOB. The single point resolution in TIB and TOB depends on the layout of the specific layer and varies between $23\,\mathrm{\mu m}$ and $53\,\mathrm{\mu m}$.

Stereo modules, constructed by placing two modules back to back, rotated by $100\,\mathrm{mrad}$, are placed in the first two layers of both TIB and TOB, the first two discs of TID and the first two and the fifth discs of the TECs. These allow for 2-D measurements, with a precision of the z position measurement of $230\,\mathrm{\mu m}$ in TIB and $530\,\mathrm{\mu m}$ in TOB.

For high momentum tracks of about $100\,\mathrm{GeV}$ in the region of $|\eta| < 1.6$ a p_{T} resolution of 1-2% is achieved, while the impact parameter of these tracks can be measured with a resolution of about $10\,\mathrm{\mu m}$.

Compared to other tracking technologies, an all silicon tracking system as used in CMS consists of significantly more material. The material budget lies between 0.4 and 1.8 radiation length X_0, as shown in Figure 3.5. For light charged particles such as electrons this leads to a significant probability to emit bremsstrahlung in while traversing the tracking detector, which has to be taken into account in the reconstruction of particles.

3.2.2. The electromagnetic calorimeter

The electromagnetic calorimeter (ECAL) measures the energy of electrons and photons. It uses lead tungstate ($PbWO_4$) crystals both as absorber and active material. The electromagnetic shower induced by the electron or photon leads to the emission of scintillation light in the crystal, which is measured at the end of the crystals by avalanche photo diodes (APDs) in

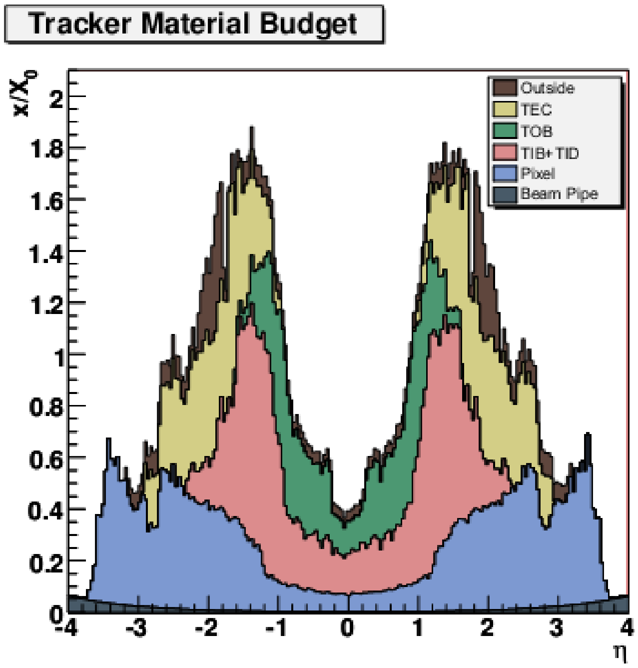

Figure 3.5.: Material budget of the CMS tracking detector in units of radiation length X_0 as a function of η.

the barrel segment of the ECAL and more radiation hard vacuum photo triods (VTPs) in the endcap region. The choice of lead tungstate was driven by the need for a material that is at the same time dense ($8.28\,\mathrm{g/cm^3}$), has a small MoliĂ¨re radius ($2.2\,\mathrm{cm}$) and is fast. About 80% of the scintillation light is emitted after $25\,\mathrm{ns}$, which is the time between two LHC bunch crossing under design conditions. The structure of the ECAL is shown in Figure 3.6. The ECAL barrel (EB) covers the region of $|\eta| < 1.479$ and consists of 61200 crystals. They have a size of $2.2 \times 2.2\,\mathrm{cm}^2$ at the front and $2.6 \times 2.6\,\mathrm{cm}^2$ at the back, with a length of $23\,\mathrm{cm}$, corresponding to 25.8 X_0. In the ECAL endcaps (EE), consisting of 7324 crystal each, they are slightly larger ($2.862 \times 2.862\,\mathrm{cm}^2$ to $3.0 \times 3.0\,\mathrm{cm}^2$) and shorter ($22\,\mathrm{cm}$, corresponding to 24.7 X_0). The EEs extend the geometric coverage of the ECAL to $|\eta| = 3.0$.

In the region of $1.653 < |\eta| < 2.6$ a preshower detector, consisting of two layers of silicon strips and two layers of lead absorber, is installed to distinguish between prompt photons and those from the decay $\pi^0 \to \gamma\gamma$. The strips, oriented perpendicular to each other, have a pitch of $2\,\mathrm{mm}$, allowing to resolve the two showers of the photons from the π^0.

The production of scintillation photons per energy deposit is temperature depend. Therefore the ECAL is kept at a temperature of $18 \pm 0.05\,^\circ\mathrm{C}$, where it is about 4.5 photons per MeV.

The typical resolution of the ECAL is parametrized as

$$\left(\frac{\sigma}{E}\right)^2 = \left(\frac{2.8\%}{\sqrt{E}}\right)^2 + \left(\frac{0.12}{E}\right)^2 + (0.30\%)^2, \tag{3.1}$$

with three terms describing different sources of uncertainty. The first term includes statistical

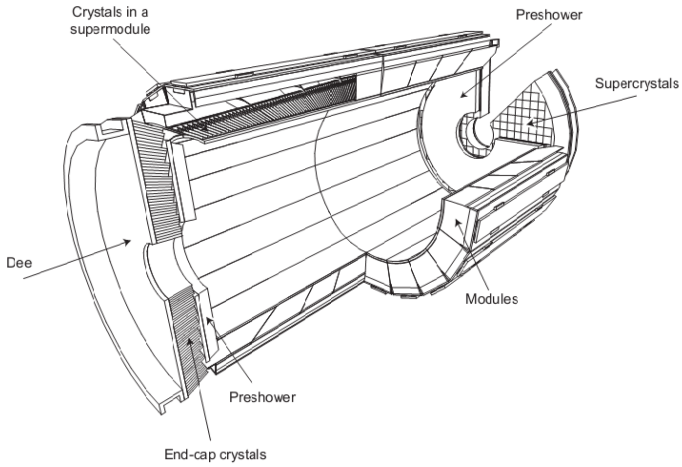

Figure 3.6.: Schematic view of the CMS ECAL.

fluctuation in the production of scintillation light as well as the energy distribution over several crystals. The second term covers such sources of noise as electronic noise or pileup. The constant term accounts for other sources of uncertainties such as calibration errors. The size of the different contributions has been confirmed in test beam measurements [8].

3.2.3. The hadron calorimeter

The hadron calorimeter (HCAL) measures the energy of charged and neutral hadrons. In the barrel region of the detector it is situated between the back face of the ECAL and the coil of the solenoid, at radii between $1.7\,\mathrm{m}$ and $2.95\,\mathrm{m}$, limiting the amount of material that can be used in its construction. Therefore additional detectors are placed outside of the volume of the magnet, forming the hadron outer calorimeter (HO). The HCAL barrel (HB) is complemented on each side by a HCAL endcap (HE) and the geometric coverage is extended to high values of $|\eta|$ by dedicated forward calorimeters (HF). The placement of these subdetectors relative to the other components of CMS are shown in Figure 3.7.

The HCAL barrel and outer detectors (HB and HO)

The HB covers the geometric region $|\eta| \leq 1.3$. It is constructed as a sandwich calorimeter, consisting of plastic scintillator as the active material. For the absorber material, the fourteen inner layers of the HB are made from brass, while steel is used for the front and back plates of the HB to increase the stability of the construction. The scintillator is divided in 144 segments in ϕ and 32 segments in η, resulting in a spatial granularity of 0.087 in both η and ϕ. The scintillation light produced in the active material is transported to hybrid photo diodes using scintillating fibres. As all layers of one tower in η and ϕ are read out by the the same photo diode, there is no segmentation in the readout in r, except for the two towers closest to the HE on each side. The material of the ECAL in front of the HB corresponds to about 1.1

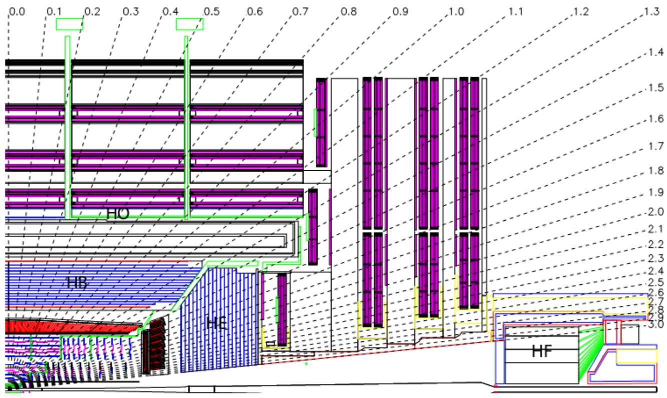

Figure 3.7.: Schematic view of the CMS HCAL.

interaction length λ_i. The absorber material of the HB itself amounts to only 5.82 λ_i at $\eta = 0$, which increases to 10.6 λ_i at $|\eta| = 1.3$. To measure the energy of jets not contained in the HB, the HO is placed outside the vacuum containment of the solenoid. It consists of one additional layer of scintillator, with the magnet acting as absorber, except for most central part of the detector, where one additional layer of steel absorber and scintillator are installed. Hereby the material budget of the HCAL is increased to at least 10 λ_i over the whole barrel region.

The HCAL endcaps (HE)

The HE extends the geometric coverage of the HCAL up to $|\eta| = 3.0$, coinciding with that of the EEs. It is constructed from the the combination of brass absorber and plastic scintillator as the HB and for the region $1.3 \leq |\eta| \leq 1.6$ also retains the $\Delta\eta \times \Delta\phi = 0.087 \times 0.087$ granularity in η and ϕ. For $|\eta| \geq 1.6$ the segmentation is coarser, resulting a granularity of $\Delta\eta \times \Delta\phi \approx 0.17 \times 0.17$. This structure again corresponds to about 10 λ_i. The longitudinal segmentation of the readout of the towers differs based on the location of the tower. The two towers closest to the beam line are read out in three segments, while most others are read out in two segments. The two towers overlapping with HB are read out without longitudinal segmentation. Multipixel hybrid photo diodes have been chosen for the readout due to their low sensitivity to magnetic fields.

The hadron forward calorimeter (HF)

Of all subdetectors of CMS, the HF covers the highest values of $|\eta|$, reaching up to values of $|\eta| = 5.2$. This close to the beam pipe radiation hardness is the key feature of the design, as nearly 90% of the energy deposited in the detector as the result of a proton-proton interaction is allotted to the HF. It is constructed as two $3.5\,\mathrm{m}$ long cylinders with a radius of $1.3\,\mathrm{m}$, located at $|z| = 11.2\,\mathrm{m}$. The first $1.65\,\mathrm{m}$ consist of plates of steel with a thickness of $5\,\mathrm{mm}$, again corresponding to about 10 λ_i. The active material are quartz fibres, which are inserted into grooves in the steel plates. The particles created in showers in the absorber emit Cherenkov radiation in the fibres, which is detected by photomultiplier tubes at the end of the fibres. As the Cherenkov threshold is lowest for electrons, at $190\,\mathrm{keV}$, the HF is more sensitive towards electromagnetic than hadronic showers. To separate the two, half of the fibres start only at a depth of $22\,\mathrm{cm}$ inside the absorber. As the electromagnetic shower develop faster, they deposit most of their energy before this point, which distinguishes them from hadronic showers.

3.2.4. The muon system

Muons are in general not stopped by any of the subdetectors of the CMS detector inside the solenoid. Therefore they can be measured with high precision in a clean environment outside of it. The muon detectors are therefore placed inside the return yoke of the magnet, both for the muon barrel (MB), covering up to $|\eta| = 1.2$ and muon endcap (ME) detectors, placed between $|\eta| = 0.9$ and $|\eta| = 2.4$. Being placed so far away from the interaction point, the muon detector have to cover a large area, which requires them to be rather inexpensive compared to other technologies used in the construction of CMS. Three different types of gaseous detectors are used to provide at the same time identification, p_{T} measurement and triggering for muons. In the barrel region, drift tubes (DT) are used as the main muon detectors, while in the endcaps cathode strip chambers (CSC) are used because they are faster and better equipped to deal with the larger and inhomogeneous magnetic field in this region of the detector. To provide a very fast muon tagging for the trigger, resistive plate chamber (RPC) complement the other two technologies in both the barrel and the endcaps.

Drift tubes (DT)

In the barrel, the TD chambers, each made of 2 or 3 super layers, which in turns are made up of four layers of TDs, are grouped together into four muon stations. Of these the first three contain 2 groups of 4 layers of chambers measuring in the $r - \phi$ plane and one group measuring the z coordinate. In the last muon station only the groups measuring in $r - \phi$ are present. The chambers in each chamber are offset by half of the width of a cell with respect to the next layer to not leave dead spots in the geometric coverage. The DT system consists of about 172000 sensitive wires. The drift tubes are filled with a mixture of 85% Ar and 15% CO_2, and their structure is shown in Figure 3.8 The $r\phi$ resolution of a single layer of DT is about $250\,\mu\mathrm{m}$, so that one chamber reaches a precision of $100\,\mu\mathrm{m}$.

Cathode strip chambers (CSC)

The CSC are multiwire proportional chambers, consisting of 6 planes of anode wires interleaved with 7 panels of cathode strips. The chambers have trapezoidal shape and are arranged in four discs around the beam axis, each further segmented into two or three rings. The cathode strips measure the ϕ coordinate while the anode wires measure the radial coordinate. Figure 3.9

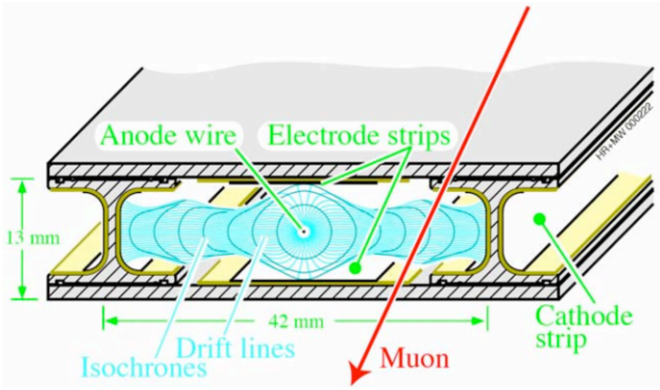

Figure 3.8.: Schematic view of one DT.

shows the structure of one chamber on the left side and the creation of a signal due to a amplification of the initial ionization in an avalanche close to the anode wire.

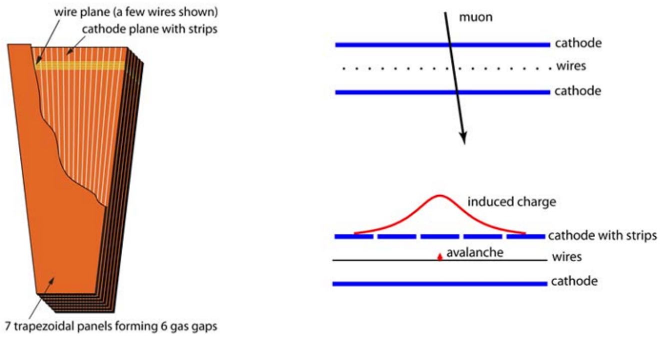

Figure 3.9.: Schematic view of one CSC (left) and the creation of a signal (right).

Resistive plate chambers (RPC)

The RPCs consist of three layers of Bakelite, which form two small gas filled gaps and between which high voltage is applied. The amplification of the initial signal is very fast in this configuration, with drift times of about $5\,\mathrm{ns}$. Therefore this technology is well suited to associate muon candidates to the LHC bunch crossings. In the barrel region six layers of RPCs are installed, while three layers are used in the endcaps for $|\eta| \leq 1.6$.

Momentum resolution

The p_T resolution of the muon system alone was expected to be about 10% for muons with p_T up to $200\,\mathrm{GeV}$. Combined with the information from the inner tracking system, a resolution of about 1% was expected to be achieved in the central region of $|\eta| \leq 0.8$ for a p_T of $10\,\mathrm{GeV}$, increasing to about 2% for a p_T of $200\,\mathrm{GeV}$.

The p_{T} resolution for muons has been measured using data collected in 2010 [9]. Using the muon system alone, resolutions better than 10% have been found for the barrel region for muons with $p_{\mathrm{T}} > 15\,\mathrm{GeV}$. The muon resolution improves when combining the information from the muon system with those from the inner tracking system. The precision of the tracking system dominates for a wide p_{T} range and averaging over η and ϕ resolutions of (1.8±0.3(stat.))% at $\mathrm{p_T} = 30\,\mathrm{GeV}$ to (2.3±0.3(stat.))% at $\mathrm{p_T} = 50\,\mathrm{GeV}$ have been achieved.

3.3. Trigger and data acquisition

If the LHC is operated at the design bunch spacing of $25\,\mathrm{ns}$, bunch crossings occur with a rate of about $40\,\mathrm{MHz}$ in the interactions points. Even is this has been reduced by at least factor of two during Run I of the LHC because of the increased bunch spacing, event rates of this magnitude can not be handled by the available means of data processing. The total event rate is therefore reduced by a factor of about 10^6 by two subsequent trigger systems. The Level-1 (L1) trigger consists of programmable electronics, allowing for an coarse reconstruction of physics objects in the calorimeters and the muon system. This system reduces to event rate to a maximum of $100\,\mathrm{kHz}$. Following an L1 accept (L1A), the CMS data acquisition system (DAQ) collects the event information from the readout of the different subdetectors and passes it one to the High-Level trigger (HLT). The HLT is a software trigger and has access to the full detector readout [10]. It can perform a full reconstruction of the events to apply approximate versions of the algorithms used in offline data analysis. It accepts events at a rate of a few $10^2\,\mathrm{Hz}$.

Level-1 trigger (L1)

The output of the different subdetectors are stored in pipelined buffers inside the readout electronics. This limits the time between the bunch crossing and the distribution of the L1 accept to the subsystems to $3.2\,\mathrm{\mu s}$. The L1 is therefore constructed from mostly custom-built programmable electronics either directly inside the detector or located close by in the underground facilities. As the readout of the tracker and track reconstruction are feasible on this time scale only calorimeter and muon system information are used. The L1 system is divided into local, regional and global components, as shown in Figure 3.10.

The calorimeter trigger the local component are the Trigger Primitive Generators (TPGs). For $|\eta| \leq 1.74$ they have an (η, ϕ)-coverage of 0.087×0.087, corresponding to one HCAL tower and a 5×5 matrix of ECAL crystals in front of it. The TPGs communicate the energy deposits in the trigger tower and the number of the bunch crossing to the Regional Calorimeter Trigger. One calorimeter region consists of 4×4 trigger towers. Candidates for electrons or photons (e/γ) are formed by by selecting the towers with the highest E_T in the ECAL. Based on information about the energy distribution inside the ECAL tower, the ratio of energy in ECAL and HCAL in the trigger tower and the overall distribution of energy in the neighbouring trigger towers the candidates are classified as isolated or non-isolated. Per region four isolated and four non-isolated e/γ candidates, the transverse energy sums of the trigger towers and information to identify τ leptons and muons via their minimum ionizing particle (MIP) signature and isolation are passed to the Global Calorimeter Trigger (GCT). The GCT performs a simple jet clustering algorithm and is able to calculate per event observables such as the number of jets, the total and missing transverse energy and sum of the transverse energy of all jets above a certain threshold (H_T). These information are delivered to the global trigger

In the muon trigger all three detector components (DT,CSC, and RPC) contribute. In the local trigger, the DT chambers deliver track segments in the ϕ-projection and hit patterns in the η-projection, while the CSCs produce three-dimensional track segments. Both use timing information to associate this information with the bunch crossing. In the regional trigger, DT and CSC information are processed in separate track finders, which produce muon candidates. These are ordered as a function of p_{T} and track track quality and up to four candidates are delivered to the global muon trigger from each track finder. The RPCs also deliver muon candidates. With their excellent timing resolution of about $1\,\mathrm{ns}$ they deliver an unambiguous association of the muon candidates to the correct bunch crossing. The global muon trigger receives up to four muon candidates each from the DTs, the CSCs and the barrel and endcap RPCs. The information consists of p_{T}, η, ϕ and information on the quality of the muon reconstruction. Candidates from the RPCs are matched with the ones from DT and CSC and, if matches are found, merged into single candidates. Unmatched candidates with low quality are suppressed. The track of the candidates is extrapolated back into the calorimeters to add the MIP and isolation information from the regional calorimeter trigger. The four best muon candidates are forwarded to the global trigger.

The global trigger collects the information from the global muon and global calorimeter trigger. Up to 128 trigger algorithms can be performed on the trigger objects at the same time, the most basic being simple p_{T} thresholds. If the criteria of one of the algorithms is met by the event, it is accepted by the L1 trigger and a signal is sent to the DAQ to read out the event.

Data acquisition system (DAQ)

Following an L1 accept the DAQ receives the information from the different subdetectors split in about 650 data sources, each delivering about 2 kB of data. These event fragments are assembled into whole events by the event builder. The event is then sent to one Filter Unit in the Event Filter, where the HLT software is running. The DAQ has to deal with input rates of up to $100\,\mathrm{kHz}$ and consists of 8 nearly independent slices, each able to take input at a rate of $12.5\,\mathrm{kHz}$. The DAQ includes a back-pressure system, which automatically throttles the L1 trigger in the case where the input rate exceeds what can be processed by the DAQ. This introduces dead times in the detector readout but prevents data corruption and buffer overflows. To fully utilize the capacities of the trigger system and the DAQ, trigger thresholds can be adapted during data taking. The shortest time scale on which the thresholds are kept constant is called lumi section and is defined as 2^{20} LHC orbits, corresponding to about $93\,\mathrm{s}$. The structure of the DAQ is shown in Figure 3.10.

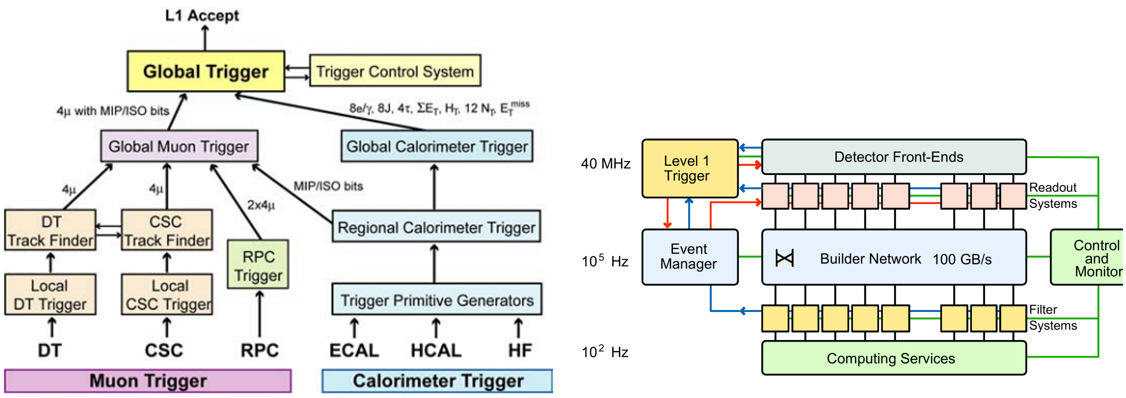

Figure 3.10.: Structure of the CMS Level-1 trigger (left) and data acquisition system (DAQ) (right)

High level trigger (HLT)

The HLT software is run on a dedicated computing element, the Event Filter Farm, located in the CMS service caverns. During the data taking in 2012 it consisted of about 13200 processor cores [11], allowing for a processing time of about $150\,\mathrm{ms}$ at a input rate of $100\,\mathrm{kHz}$. The HLT system reduces input data rates of up to $100\,\mathrm{GB/s}$ to several hundred $\mathrm{MB/s}$, which are sent to the CERN computer centre for storage. As a full event reconstruction can be performed at HLT level, even if it is often restricted to small regions of the detector for timing reasons, much more complex quantities can be used to separate potentially interesting signatures from the large backgrounds. However, approximate methods have to be used sometimes to maintain an acceptable processing time per event. Also, some calibration and alignment methods can only be performed after the data taking, making the HLT less precise compared to the offline reconstruction. While a large variety of triggers is used by CMS to select different kinds of events, this description will focus on the ones most relevant to this analysis.

The most important signal and control samples are collected with dileptson triggers. In general, they select events that contain two leptons (electrons or muons), of which one is required to have a reconstructed transverse momentum p_T of at least $17\,\mathrm{GeV}$, while for the second this is relaxed to $8\,\mathrm{GeV}$. In general, the lepton with the higher (lower) p_T is referred to as the leading (trailing) lepton. While the algorithms employed to reconstruct muons and electrons are the some among all possible combinations of leptons, the triggers used for preselection at L1 level differ in their thresholds [12]. The dielectron HLT is based on the so called L1 seed `L1_DoubleEG_13_7` and the dimuon on an logical OR of `L1_DoubleMu_10_Open` and `L1_DoubleMu_10_3p5`. To select events with an electron and a muon, two HLTs are employed, one with the electron and one with the muon as the leading lepton. The L1 seeds are a logical OR of `L1_Mu3p5_EG12` and `L1_MuOpen_EG12`, and `L1_Mu12_EG7`, respectively. The numbers refer to the p_T or E_T thresholds of the muon and e/γ candidates in GeV, while `Open` indicates a threshold of $0\,\mathrm{GeV}$. As the algorithms to reconstruct physics objects at HLT level are so similar to those used offline, no dedicated description is given here.

4. Data analysis and event selection

4.1. Object reconstruction

The physics objects relevant to this analysis are electrons, muons, jets and the missing transverse energy $E_{\mathrm{T}}^{\mathrm{miss}}$. Here the reconstruction of these objects from the information provided by the CMS detector is described. While the electron and muon candidates used here are reconstructed independent of each other with dedicated algorithms, jets and $E_{\mathrm{T}}^{\mathrm{miss}}$ are provided by the particle flow (PF) algorithm. It combines information from all subdetectors to achieve a consistent description of the full event.

4.1.1. Muon reconstruction and selection

The track of a muon is reconstructed separately in the inner tracker and the muon system, resulting in a *tracker track* and a *standalone muon*.

Tracks in the inner tracker are reconstructed using a method called Combinatorial Track Finder (CTF) [13], which performs pattern recognition and track fitting employing a Kalman filter technique [14]. The track is described by a five-dimensional state vector, whose initial parameters are taken from track seeds, determined from three hits or two hits and a vertex constraint in the pixel detector or the innermost layers of the strip detector. The state vector is extrapolated to the next tracker layer taking into account uncertainties and energy losses due to interactions with the tracker. If tracker hits are found in the modules where they are expected from the extrapolation, they are added to the track candidate. If no hits are found, a ghost hit is added to the track to account for inefficiencies in the hit reconstruction. A track fit is then performed to all hits associated with the track candidate, using again Kalman filtering and smoothing. This procedure is performed iteratively, each time removing the hits already associated to a track candidate and relaxing the requirements on the track seeds to allow for reconstruction of track with low p_{T} or not originating from the primary interaction. In the reconstruction of the data taken in 2012, seven iterations were performed [15].

For the reconstruction of *standalone muons* in the muon system, the hits inside the individual muon chambers are fitted to generate track segments, providing first estimates of the track parameters under the hypothesis that the muon was created in the interaction region and was travelling through the muon system from the inside out. These segments are used as starting points for a track reconstruction using all hits from the DTs, CSCs and RPCs, again using the Kalman filtering technique [16].

Tracker tracks are promoted to *tracker muons* when they can be matched to a track segment in the muon detector. *Standalone muons* are matched to tracks from the inner tracker. If a compatible track is found a combined fit to all hits of the track and the *standalone muon*

Criterion	Selection
Acceptance	
p_T	$> 10\,\mathrm{GeV}$
$\lvert\eta\rvert$	< 2.4
Muon ID	
Required to be a	*tracker muon*
	global muon
	particle flow muon
Track quality	
χ^2/N_{dof}	< 10
valid muon hits	> 0
matched stations	> 1
valid pixel hits	> 0
tracker layers with hits	> 6
Impact parameter	
$d0 = \sqrt{dx^2 + dy^2}$	$< 0.02\,\mathrm{cm}$
dz	$< 0.1\,\mathrm{cm}$

Table 4.1.: Summary of requirements of the muon selection.

is performed, resulting in a *global muon*. The PF algorithm applies further selection requirements to the reconstructed *global* and *track muons*, introducing a fourth category, the *particle flow muon* [17].

Muons selected in this analysis are required to be reconstructed as *tracker*, *global* and *particle flow* muons. The χ^2 per degrees of freedom of the track fit must not exceed 10. Several requirements on the information available for the different track fits are made: At least one muon chamber hit must be included in the track fit of the *global muon*. For the fit of the *tracker muon* at least one hit in the pixel detector and six layers with hits in the strip detector have to be available. Also the track from the inner tracker has to be matched to at least two track segments in the muon chambers. To ensure that the muon originates from the primary interaction and to suppress backgrounds from cosmic muons the impact parameter of the track with respect to the primary vertex must not exceed $0.02\,\mathrm{cm}$ in the x-y plane and $0.1\,\mathrm{cm}$ in z direction. Selected are muons with a p_T larger than $10\,\mathrm{GeV}$ and $\lvert\eta\rvert$ less than 2.4. The muon selection is summarized in Table 4.1.

4.1.2. Electron reconstruction and selection

The signature of an electron in the CMS detector is a track reconstructed by the tracking detectors that leads to a matching cluster of energy reconstructed in the ECAL. In practice this is complicated by the large material budget of the tracking detectors, resulting in a high probability of an electron to loose energy in form of bremsstrahlung. About 35% of all electrons loose more than 70% of their energy and for 10% the energy loss exceeds 95% [18]. The reconstruction is further complicated by the large solenoidal magnetic field, which bends the electron's trajectory away from the radiated photons, leading to a spread of the energy in ϕ direction. This has to be taken into account both in the tracking algorithms and the clustering of the energy deposits in the ECAL.

In the ECAL two different algorithms are used to group the energy deposits into clusters and clusters of clusters, called super clusters (SCs), in the barrel and endcap regions of the detector. Both are designed to group together the energy deposits of the electron itself and those of the bremsstrahlung photons. In the of $1.6 < |\eta| < 2.6$ the preshower is located in front of the ECAL and electrons will deposit a fraction of their energy there. The energy deposited in the strips of the preshower between an SC in the ECAL and the primary vertex is summed and added to the energy of this SC [19]. ADD SC position calculation and electron charge! CHANGE ALL REFS TO EGM-13-001 once submitted to journal!

In the track reconstruction with Kalman filters as discussed above energy losses due to interactions of the particles with the tracker material are considered to be Gaussian. For electrons, however, this is not sufficient because the dominant energy loss due to bremsstrahlung is a non-gaussian contribution. Electron candidate tracks are therefore fitted with a Gaussian Sum Filtern (GSF) algorithm [20], which models the non-Gaussian components as a sum of Gaussian distributions. GSF tracking is initiated in two ways. *ECAL driven seeding* requires the presence of a track seed that matches the position of an SC when extrapolating backwards from the ECAL to track [18]. Alternatively, *tracker driven seeding* is started by tracks that either match the position of ECAL clusters when extrapolated to the ECAL surface, covering the case of no bremsstrahlung, or are of poor quality with only few associated hits [13]. The GSF track and the energy measurement in the ECAL are combined into the final electron candidate.

Electrons are selected requiring p_{T} larger than $10\,\mathrm{GeV}$ and $|\eta| < 2.5$. The gap region between ECAL barrel and endcaps of $1.442 < |\eta| < 1.566$ is exluded. To suppress background from muons that radiate photons electrons with a distance of $\Delta R = \sqrt{\Delta\phi^2 + \Delta\eta^2}$ to the nearest *global* or *tracker muon* less than 0.1 are rejected. Backgrounds from photon conversion, decays of heavy flavour quarks or charged hadrons are suppressed by a set of selection criteria. The matching of track and supercluster is quantified by the differences between the supercluster position and the parameters of the track extraploated from the vertex to the ECAL surface in $\Delta\phi$ and $\Delta\eta$. As the energy of the electron is contained in the ECAL, the ratio of hadronic energy deposited in the HCAL behind the electron candidate must be small. The energy spread in the ECAL due to bremsstrahlung occurs in ϕ direction. Therefore no significant spread of the energy in η, parametrized as

$$\sigma_{i\eta i\eta} = \frac{\sum_i^{5\times 5} w_i \cdot (\eta_i - \bar{\eta}_{5\times 5})^2}{\sum_i^{5\times 5} w_i}, \tag{4.1}$$

$$w_i = max(0, 4.7 + ln(\frac{E_i}{E_{5\times 5}})), \tag{4.2}$$

is expected, where for 5×5 crystals around the seed crystal the distance in η from the mean η of the cluster is summed, weighted by the energy deposit in each crystal. For a well measured electron there is good agreement between the energy deposited in the ECAL

Criterion	Selection at HLT		Selection at Analysis Level	
	EB	EE	EB	EE
Acceptance				
p_{T}	trigger dependent		$> 10\,\mathrm{GeV}$	
$\lvert\eta\rvert$	< 2.5		< 2.5, excluding $1.442 < \lvert\eta\rvert < 1.566$	
ID variables				
$\lvert\Delta\eta\rvert$	0.01	0.01	0.007	0.009
$\lvert\Delta\phi\rvert$	0.15	0.10	0.15	0.10
$\sigma_{i\eta i\eta}$	0.011	0.031	0.01	0.03
H/E	0.10	0.075	0.12	0.10
$\lvert\frac{1}{E} - \frac{1}{p}\rvert$	-		0.05	0.05
Conversion rejection				
missing pixel hits	-		≤ 1	≤ 1
vertex fit probability	-		$< 10^{-6}$	$< 10^{-6}$
Impact parameter				
$d0 = \sqrt{dx^2 + dy^2}$	-		$< 0.02\,\mathrm{cm}$	$< 0.02\,\mathrm{cm}$
dz	-		$< 0.1\,\mathrm{cm}$	$< 0.1\,\mathrm{cm}$

Table 4.2.: Summary of requirements of the electron selection.

and the track momentum measured at the vertex. Therefore the value of $\lvert\frac{1}{E} - \frac{1}{p}\rvert$ must be small. Requirements on the impact parameter of the track with the respect to the vertex are made. Two requirements are applied to reject electrons from converted photons. Only one pixel layer with missing hit is allowed, rejecting most conversions occurring after the first layer of the pixel detectors. To reject also conversion in this first layer and in the beam pipe, vertex fits for the electron track with neighbouring tracks are performed in order to reconstruct the point of conversion. For a prompt electron, the probability of these fits is low. Some of these requirements are already applied on HLT level. In order to select electrons for which the trigger is fully efficient, selections at least as strict are applied at analysis level. The specific requirements are listed in Table 4.2, separately for barrel and endcap when appropriate.

4.1.3. Observables reconstructed with Particle Flow

The algorithm

The particle flow (PF) algorithm is designed to combine information from all subdetectors to reconstruct a consistent description of the event, resulting in a list of reconstructed particles. The basic building blocks are PF elements, which are reconstructed in each subdetector separately: Tracks of charged particles in the tracker, energy clusters in the calorimeters and muon tracks in the muon system. A linking algorithm then combines elements into blocks based on their geometrical distance, for example by extrapolating a track into the ECAL and HCAL and searching for compatible clusters. Similarly, calorimeter clusters are linked between the preshower, ECAL, and HCAL and tracks from the tracker are associated with those from the muon system. The reconstruction of *particle candidates* is performed on the elements inside a block. Muons are reconstructed first, followed by electrons, for which, similar to the standard algorithm described above, a refit of the track with the GSF algorithm is performed and bremsstrahlung photons are collected in the ECAL. Lastly, calorimeter clusters compatible with a track are identified as charged hadron, while clusters without a matching track are either categorized as neutral hadrons, or, if no or only small energy deposits in the HCAL exist, as photons [21].

Jets

The jets of particles produced in the hadronization of quarks and gluons are grouped together by clustering algorithms. An anti-k_T algorithm [22], performed using a fast implementation [23, 24], is used in this analysis. Input to the clustering are the *particle candidates* reconstructed by the particle flow algorithm.

The anti-k_T algorithm is a sequential clustering algorithm. Two distance measures are introduced, the first between two particles or pseudo-jets i and j and the second between particle or pseudo-jet i and the beam axis:

$$d_{ij} = min(k_{Ti}^{-2}, k_{Tj}^{-2}) \frac{\Delta_{ij}^2}{R^2}, \tag{4.3}$$

$$d_{iB} = k_{ti}^{-2}, \tag{4.4}$$

with $\Delta_{ij}^2 = (y_i - y_j)^2 + (\phi_i - \phi_j)^2$ and k_{Ti}, y_i, and ϕ_i being the transverse momentum, rapidity and azimuth of a particle. For an entity (particle, pseudo-jet) i all distances are calculated. If the smallest is a d_{ij}, i and j are combined in a new pseudo-jet. If the smallest distance if the distance to the beam d_{iB}, the pseudo-jet is considered a final jet and removed from the list of particles available for clustering. The parameter R governs the size of the resulting jet and is set to 0.5 in this analysis.

The measured jet energy has to be corrected for energy offsets and the non-uniform and non-linear response of the detector. Each component of the jet's four-momentum vector is corrected by a multiplicative factor [25]

$$p_\mu^{cor} = C \cdot p_\mu^{raw}. \tag{4.5}$$

The correction is applied as a sequence of different factors:

$$C = C_{\text{offset}}^{L1}(p_T^{raw}) \cdot C_{MC}^{L2L3}(p'_T, \eta) \cdot C_{rel}^{L2Residual}(\eta) \cdot C_{abs}^{L3Residual}(p''_T). \tag{4.6}$$

The L1 correction, applied to the raw jet, corrects for offsets due to the underlying event and pileup using a jet area approach. The jet area A_j is determined for each jet and the particles in the event are clustered with a k_T jet clustering algorithm with a distance parameter $R = 0.6$, which clusters a large number of soft jets in each event. The median p_T density ρ is then defined as the median of the distribution of p_{T_j}/A_j for all of these jets. Therfore ρ is not influenced by the presence of hard jets from the primary interaction in the event and is a measure for the pileup activity, the underlying event and electronic noise. Jets are then corrected by the factor $C^{L1}_{\text{offset}}(p_T^{raw}) = 1 - \frac{(\rho - <\rho_{UE}>)\cdot A_j}{p_T^{raw}}$, where $<\rho_{UE}>$ is the mean p_T density due to the underlying event, measured in events with no pileup interactions. The L2L3 corrections, derived from Simulation, corrects for the non-linearities and non-uniformities of the detector response to jets of different p_T and η and is applied to the offset-corrected jet. To correct for the differences between Simulation and real data, jets in data events are further corrected for the residual differences between the two.

In this analysis, the p_T of a jet is required to exceed $40\,\mathrm{GeV}$ and jets are required to lie inside the fiducial volume of the ECAL of $|\eta| < 3.0$. A set of loose quality selections is applied to suppress jets reconstructed because of detector noise, ensuring that the jet is reconstructed in more than one subdetector and has more than one constituent. As the jet clustering is performed using all reconstructed *particle candidates*, jets within $\Delta R = 0.4$ to leptons identified with the criteria described above are rejected.

Because of their long lifetime, b-jets decay at a measurable distance from their production vertex, allowing for the reconstruction of a secondary vertex. In this analysis the *combined secondary vertex* (CSV) algorithm is used. Likelihood ratios based on a variety of variables characterizing the secondary vertices and the tracks inside the jet are used to construct a single discriminator. If it's value exceeds a given threshold, the jet is tagged as originating from a b-quark [26]. The performance of the b-tagging algorithms have been measured on the $\sqrt{s} = 8\,\mathrm{TeV}$ dataset [27]. The average identification efficiency as a function of the discriminator value is shown on the left side of Figure 4.1. For the medium working point of 0.679, chosen in this analysis, the efficiency is about 70% while the probability to misidentify a jet originating from a light quark as a b-jet is between 1% and 3%, depending on the p_T of the jet, as shown on the right side of Figure 4.1. In this analysis b-jets are considered with a p_T larger than $30\,\mathrm{GeV}$ and $|\eta| < 2.4$.

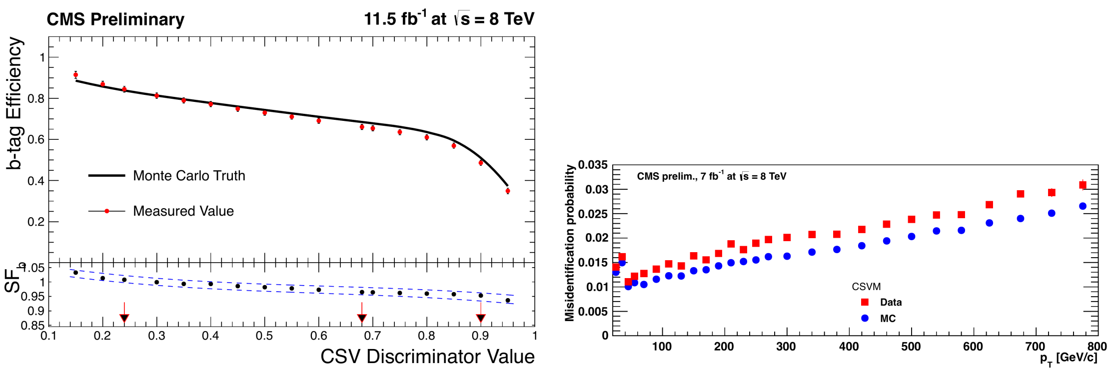

Figure 4.1.: Performance of the CSV b-tagging algorithm. Shown is the identification efficiency as a function of the discriminator value (left) and the probability of misidentifying a jet originating from a light quark as a b-jet (right) [27].

Missing transverse energy

As the transverse momenta of the initial partons are negligible compared to their large momenta in beam direction, the sum of the transverse momenta of all particles produced in the interaction is essentially zero because of conservation of momentum. For the reconstructed event this is not necessarily the case, leading to a missing transverse energy ($E_{\mathrm{T}}^{\mathrm{miss}}$) different from zero. The measurements in the detector have a finite resolution and are subject to detector noise and are subject to gaps in the detector acceptance. Also, particles that are only weakly interacting, such as neutrinos, are not detected by CMS and cause an imbalance of the transverse momentum sum. As this imbalance is the only experimental signature of this class of particles, a good $E_{\mathrm{T}}^{\mathrm{miss}}$ resolution is a key factor for the discovery of processes that include the production of new weakly interaction particles.

Several algorithms have been developed in CMS to reconstruct $E_{\mathrm{T}}^{\mathrm{miss}}$ [28]. Calorimetric (Calo) $\vec{E}_{\mathrm{T}}^{\mathrm{miss}}$ is calculated as the negative vector sum of the energy deposits in each calorimeter tower. The small energy deposits from muons are replaced by the p_{T} measurements of muons. A further correction is introduced in the track-corrected (TC) $\vec{E}_{\mathrm{T}}^{\mathrm{miss}}$. For well reconstructed tracks, the track measurement is more precise than the measurement of a hadron's energy in the HCAL. Therefore, for tracks not associated with an electron or muon, the track measurement is used in the calculation of $\vec{E}_{\mathrm{T}}^{\mathrm{miss}}$. The energy deposit in the calorimeter is excluded, based on a model of the calorimeter response, treating all hadrons as pions. In contrast to these subdetector-based approaches, the event description of the particle flow algorithm can be used to calculate $\vec{E}_{\mathrm{T}}^{\mathrm{miss}}$. It is defined as the negative vector sum over the p_{T} vectors of all particle flow candidates:

$$\vec{E}_{\mathrm{T}}^{\mathrm{miss}} = - \sum_{\text{PF candidates}} \vec{p}_T^{\,i}. \tag{4.7}$$

Comparing the resolution for the $E_{\mathrm{T}}^{\mathrm{miss}}$ components in x and y direction, as shown in Figure 4.2 for the data collected in 2011, PF $E_{\mathrm{T}}^{\mathrm{miss}}$ performs best of the three algorithms and is therefore used in this analysis.

Several corrections can be applied to the calculation of $E_{\mathrm{T}}^{\mathrm{miss}}$. The *type-I* corrections propagate the corrections to the jet energy to the $E_{\mathrm{T}}^{\mathrm{miss}}$ calculation for all jets with p_{T} larger than $10\,\mathrm{GeV}$ and with less than 90% of their energy deposited in the ECAL. The effects of pileup on the $E_{\mathrm{T}}^{\mathrm{miss}}$ reconstruction can be mitigated by applying *type-0* corrections, which are calculated on minimum bias events to parametrize the effects of such interactions on $E_{\mathrm{T}}^{\mathrm{miss}}$. Further corrections can be applied to correct for modulations of the $E_{\mathrm{T}}^{\mathrm{miss}}$ in ϕ [29]. As this analysis searches for events with a large genuine $E_{\mathrm{T}}^{\mathrm{miss}}$ and is therefore not very sensitive to $E_{\mathrm{T}}^{\mathrm{miss}}$ introduced by resolution effect, none of these corrections are applied. However, *type-I* corrected PF $E_{\mathrm{T}}^{\mathrm{miss}}$ is considered as a cross check.

Lepton isolation

While the lepton selection criteria described above are sufficient to reject backgrounds from particles misidentified as leptons, the do not suppress real leptons not originating from the primary interaction. As these are often produced in decay of heavy flavour quarks inside a

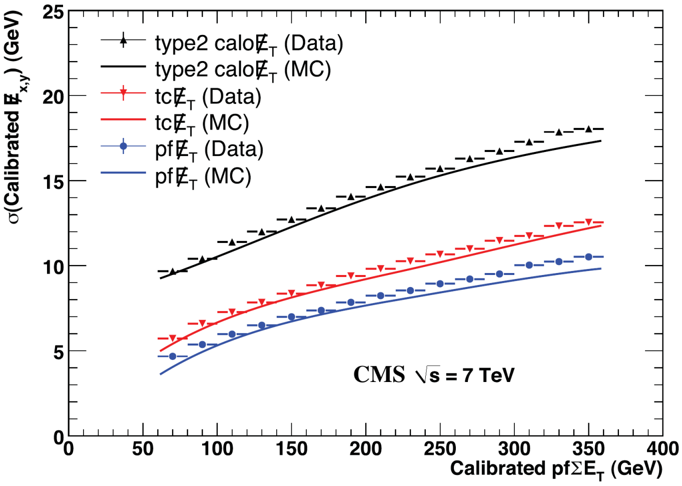

Figure 4.2.: Calibrated $E_{\mathrm{T}}^{\mathrm{miss}}$ resolution as a function of the sum of the E_{T} of all particle flow candidates in an event. Shown are Calo $E_{\mathrm{T}}^{\mathrm{miss}}$ in black, TC $E_{\mathrm{T}}^{\mathrm{miss}}$ in red and PF $E_{\mathrm{T}}^{\mathrm{miss}}$ in blue [28].

jet, are more suitable criterion is to consider the amount of activity in the detector close to the lepton candidate, called lepton isolation. In this analysis, particle based isolation is used. For this the energy deposited by charged hadron, neutral hadron, and photon particle flow candidates in a cone of $\Delta R = 0.3$ around the lepton is summed:

$$\text{Iso} = \sum_{\text{charged hadrons}} E_T + \sum_{\text{neutral hadrons}} E_T + \sum_{\text{photons}} E_T. \tag{4.8}$$

The calculation of the isolation is distorted by pileup if PF candidates originating from pileup interactions lie within the cone and are counted in the isolation sum. This is easily remedied for charged hadrons, as those originating from a pileup vertex can be excluded from the calculation. For neutral hadrons and photons there is no track that can be associated to a vertex and a direct identification as pileup particles is not possible. Different approaches are pursued to correct for this contribution for electrons and muons. In both cases an estimate for the contribution of neutral pileup is subtracted from the isolation sum, which changes to:

$$\text{Iso} = \sum_{\text{charged hadrons}} E_T + max(0, \sum_{\text{neutral hadrons}} E_T + \sum_{\text{photons}} E_T - \sum_{\text{neutral PU}} E_T). \tag{4.9}$$

For electrons the correction is similar to the L1 offset correction for jets described above. As a measure for the pileup contribution in the isolation cone the median p_{T} density in the event ρ is multiplied by the effective area of the electron in the detector, which is calculated in bins of η. The pileup correction is therefore defined as $\sum_{\text{neutral PU}} E_T = \rho \cdot A^{eff}_{\text{electron}}$. For muons $\Delta\beta$ corrections are applied. Here it is utilized that on average the contribution of neutral particles from pileup is half that of charged particles, leading to a correction defined as $\sum_{\text{neutral PU}} E_T = 0.5 \cdot \sum_{\text{charged PU}} E_T$. Because of the stochastic nature of these approaches, overcorrection is possible. Therefore, no negative contribution from neutral particles is allowed in equation 4.9. For both electrons and muons the isolation sum must not exceed 15% of the lepton candidate's p_{T}. The distribution

4.2. Event processing and datasets

Events accepted by the HLT are reconstructed using the algorithms described above, implemented in the **CMS S**oft**w**are (CMSSW) framework [30, 31]. While a first reconstruction is performed immediately after it is recorded, making it available to analysis within a few days, the full dataset recorded by CMS in 2012 has been reprocessed in a second reconstruction with updated calibrations and detector alignment in the first months of 2013. The software version used for this purpose was `CMSSW_5_3_7_patch6`. The events are stored in the **A**nalysis **O**bject **D**ata (AOD) format, which contains mostly high level objects, such as electrons and muons, and does not provide access to detailed detector information such as energy deposits, which are not of interest in many analyses. This allows to reduce the event size to $\approx 0.1\,\mathrm{MB}$, compared to about $2\,\mathrm{MB}$ for the raw detector output.

The data processing in this analysis is split into two parts. As a first step, the events in AOD format are processed utilizing the resources of the **W**orldwide **L**HC **C**omputing **G**rid (WLCG) [32, 33], a system of cross-linked computing centres providing storage and computing capacities to the LHC experiments. Datasets stored on grid sites can be accessed through the **C**MS **r**emote **a**nalysis **b**uilder (CRAB) [34]. At this stage, dilepton events are selected based on the identification criteria described above and the properties of the lepton pairs, together with other event characteristics, are stored. This is done with version TO DO: Tag current version and add version number of the `SuSyAachen` framework, which utilizes tools provided within the CMSSW framework, notably the **P**hysics **A**nalysis **T**oolkit (PAT) [35]. All datasets used in this analysis have been processed using `CMSSW_5_3_8_patch3`. Detector calibrations and alignment constant to be used in the processing of events in CMSSW are specified in so called `Global Tags`. The tags used in this analysis are `FT53_V21A_AN6` for data and `START53_V27` for simulation.

The second part consists of all further analysis performed on the events selected in the previous processing. As the event size is much reduced, it can be performed using conventional desktop PCs. Throughout the event processing chain, the ROOT framework [36] for data analysis in particle physics is frequently used. In the final analysis steps, ROOT version `5.34.21` is used.

4.2.1. Primary datasets

Events are sorted into different primary datasets based on the HLT decisions, grouping together events accepted by related triggers. As this allows for events to appear in several of theses datasets, precautions against double counting have to taken when combining different data streams in one analysis. The primary datasets most relevant to this analysis are `DoubleElectron`, `DoubleMu`, and `MuEG`, containing, amongst others, events triggered by the different dilepton triggers. As auxiliary datasets, events from primary datasets triggered by hadronic activity (`HT`,`JetHT`), single leptons (`SingleElectron`,`SingleMu`), and the α_T variableTO DO: Explain α_T,restructure sentence (`HT`,`HTMHT`) are used. Each primary dataset is split into four subsets, labelled `Run2012A to Run2012D`, each run defined by the run period of the LHC between two technical stops. The primary datasets are summarized in Table 4.3, where also the datasetpaths by which the samples can be accessed in the CMS bookkeeping

Primary dataset	purpose	dataset
DoubleElectron	Signal	/DoubleElectron/Run2012A-22Jan2013-v1/AOD /DoubleElectron/Run2012B-22Jan2013-v1/AOD /DoubleElectron/Run2012C-22Jan2013-v1/AOD /DoubleElectron/Run2012D-22Jan2013-v1/AOD
DoubleMu	Signal	/DoubleMu/Run2012A-22Jan2013-v1/AOD /DoubleMuParked/Run2012B-22Jan2013-v1/AOD /DoubleMuParked/Run2012C-22Jan2013-v1/AOD /DoubleMuParked/Run2012D-22Jan2013-v1/AOD
MuEG	Background prediction	/MuEG/Run2012A-22Jan2013-v1/AOD /MuEG/Run2012B-22Jan2013-v1/AOD /MuEG/Run2012C-22Jan2013-v1/AOD /MuEG/Run2012D-22Jan2013-v1/AOD
HT, JetHT	trigger efficiencies	/HT/Run2012A-22Jan2013-v1/AOD /JetHT/Run2012B-22Jan2013-v1/AOD /JetHT/Run2012C-22Jan2013-v1/AOD /JetHT/Run2012D-22Jan2013-v1/AOD
HTMHT	additional trigger studies	/HTMHTParked/Run2012B-22Jan2013-v1/AOD /HTMHTParked/Run2012C-22Jan2013-v1/AOD /HTMHTParked/Run2012D-22Jan2013-v1/AOD
SingleElectron	additional trigger studies	/SingleElectron/Run2012A-22Jan2013-v1/AOD /SingleElectron/Run2012B-22Jan2013-v1/AOD /SingleElectron/Run2012C-22Jan2013-v1/AOD /SingleElectron/Run2012D-22Jan2013-v1/AOD
SingleMu	additional trigger studies	/SingleMu/Run2012A-22Jan2013-v1/AOD /SingleMu/Run2012B-22Jan2013-v1/AOD /SingleMu/Run2012C-22Jan2013-v1/AOD /SingleMu/Run2012D-22Jan2013-v1/AOD

Table 4.3.: List of primary datasets used in the analysis. Additionally, the main purpose of the dataset and datasetpaths in DBS are given.

system (DBS) [37] is given.

4.2.2. Simulated datasets

Simulated datasets of Standard Model processes and SUSY models are used throughout the analysis in the design and validation of methods and the interpretation of the results in terms of potential signals. Dedicated methods are used for the different steps needed to achieve a complete model of the proton-proton interactions and the detector response.

Simulation of the physical processes

Monte Carlo methods are used to generate events according to the properties of physics processes [38]. At the beginning of the description of a process stands the calculation of the cross section for the given hard scattering of fundamental particles, using pertubation theory (see for example [39]). For many Standard Model processes and also some BSM models, calculations in next-to-leading (NLO) or next-to-next-to-leading (NNLO) order have been performed. The automated calculations performed in the event generators used for the simulation in this analysis are however mostly restricted to leading-order (LO) accuracy.

At a hadron collider, the total cross section for a process is given by the cross section for the hard scattering $\hat{\sigma}$, convolved with the parton density functions (PDFs) $f_i^p(x, Q^2)$, which give the probability that a parton i with a fraction x of the proton's momentum at the momentum scale Q^2 of the interaction will take part in the interaction. Considering all possible combinations of partons (three valence quarks, sea quarks and gluons), the total cross section is given by

$$\sigma(pp \to C) = \sum_{i,j} \int dx_1 dx_2 f_i^p(x_1, Q^2) f_j^p(x_2, Q^2) \hat{\sigma}(ij \to C). \tag{4.10}$$

The PDFs have to be inferred from data and have been studied in numerous fixed-target experiments and, most importantly, in deep-inelastic electron-proton scattering at the HERA collider [40]. Different approaches are used by several groups to parametrize the PDFs based on the available data. In the generation of simulated datasets for CMS analyses, the CTEQ6L1 [41] PDF set has been used. To study systematic effects introduced by the choice of PDF set, the NNPDF2.3 [42],MSTW2008 [43], and CT10 [44] PDF sets are used. The dependence of the PDFs on the momentum scale is described by the DGLAP (Dokshitzer, Gribov, Lipatov, Altarelli, Parisi) evolution equations [45, 46, 47], which are used to extrapolate them to the regime of the LHC.

For most processes, Madgraph [48] is used to calculate the hard scattering process, together with additional emissions of partons as part of initial and final state radiation (ISR and FSR). The inclusion of these emissions at matrix element level allows for the modelling of the radiation of hard partons that are well separated from other final state particles. However, this treatment breaks down for soft or collinear emissions, which can in turn be described by dedicated parton shower models. For this, Pythia [49] has been used for all samples relevant to this analysis. To achieve a consistent description of the parton shower, events are rejected in which the parton shower in Pythia produces jets in the phase space already covered by the emissions in Madgraph, using the MLM matching scheme [50].

The production of single top quarks is simulated using Powheg [51, 52, 53] at NLO in pertubative QCD. For these samples, a similar matching of the parton showers in Powheg and Pythia is applied.

The hadronization of colour-charged particles produced in the hard scattering or the parton shower is a non-pertubative processes which can only be described by phenomenological models. The *string fragmentation* model, as used in Pythia, is based on the idea of colour strings connecting the colour-charged particles. The energy stored in the strings increases linearly with the distance between the particles, until the string breaks and a $q\bar{q}$ pair is created, allowing for the formation of colour-singlets. These singlets may in turn break, until there no longer enough energy available to continue with this process [49]. The hadronization model, as well as the description of the underlying event and multi-parton interactions, has to be tuned to best describe existing data. For all samples used in this analysis, the tune $Z2*$ [54] is used.

The decays of τ leptons are simulated with the dedicated software Tauola [55], which includes polarization and spin correlations effects.

To simulate the effects of pileup, several simulated proton-proton interactions from a sample containing mostly soft QCD processes are added to the simulated events, including pileup interactions with a time distance to the event of $\pm 50\,\mathrm{ns}$ to emulate the effects of out-of-time pileup. The distribution of the number of additional interactions had to be estimated before the data taking took place and therefore differs from that contained in the recorded dataset.

Simulation of the detector response

A model of the CMS detector has been created using the GEANT4 toolkit [56]. It allows for a detailed description of the detector geometry and material budget and simulates the interactions of particles with the detector material. It also models the propagation of the particles inside different materials, taking into account for example the magnetic field inside the CMS solenoid. The energy deposits created by the interactions of the particles with the detector are converted into detector hits on which the full event reconstruction is performed. The simulation also includes a modelling of detector noise and dead readout channels.

As this detailed simulation is quite time consuming, a fast simulation of the CMS detector has been developed [57]. Trading some accuracy for large gains in processing time, the fast simulation is used in cases where large numbers of events have to generated, for example in scans of the parameter space of a physics model. Simplifications include for example an approximation of the tracker geometry, where the modelling of millions of individual modules has been replaced by thin cylinders of active and non-active material placed around the interaction point. A charged particle traversing these layers deposits some energy at the point at which it crosses an active layer with a predefined probability. Also the reconstruction algorithms for tracks have been simplified. Similar approaches have been applied to all subdetectors. Also the simulation of detector noise is reduced. An decrease of processing time per event by a factor of ≈ 100 has been observed.

Simulated events are stored in the AODSIM data format, which is identical to the AOD format but also includes Monte Carlo truth information about the simulated particles and their production and decay history. This allows for a processing of simulated datasets with the same software as used in the analysis of data events.

Background Samples

Possible background contributions in the analysis arise from all Standard Model processes producing lepton pairs or one lepton with the possibility for other parts of their signature to be misidentified as a second lepton. The properties of these processes can be studied in simulation. Therefore, a extensive list of simulated processes is considered in the analysis. In many cases, processes are divided into different samples based on the different possible final states. This allows to produce larger sample sizes for decays with small branching fraction without having to generate enormous amounts of more abundant final states. The full list of considered processes is shown in Table 4.4. The samples have to be scaled according to the appropriate integrated luminosity, taking into account the number of generated events and the cross section of the process. The weight is then given by $w = \frac{L \cdot \sigma}{N^{gen}_{events}}$. The top-pair production is normalized to the cross section measured by CMS in the dileptonic decay channel [58]. Cross sections for the production and dileptonic decays of W and Z bosons have been calculated using FEWZ 3.1 [59], including corrections in N(N)LO in electronweak theory (QCD). MCFM 6.6 [60] is used for the calculation of cross sections for diboson production. Cross sections for single top production have been calculated at approx. NNLO [61]. Cross sections at NLO in QCD for triboson production have been calculated using aMC@NLO [62], while for $t\bar{t}$ production in association with one additional vector boson, MCFM 6.6 has been used [63], while for $t\bar{t}WW$ the cross section calculated by Madgraph is used. The cross section for top-pair production in association with a photon has been measured by CMS [64].

Signal Samples

4.3. Event selection

A series of selection criteria are applied to the events to select signal-like topologies and reduce the contributions from Standard Model backgrounds to the final sample. Also requirements are defined to select control regions enriched in certain SM processes for the purpose of background prediction and the validation of methods. Additionally, events are reject that exhibit signs of detector noise or are otherwise not suited for analysis.

4.3.1. Event cleaning

As a first step in the selection of reconstructed events, a series of quality requirements is applied. The quality of the data recorded by the CMS detector is assessed in several automated or manual steps, summarised as *Data quality monitoring (DQM)* [65]. For each lumi section this results in a binary decision, flagging it as either *good* or *bad*, accepting only those lumi sections for which all subdetectors were fully operational during data taking and no known problems occurred in the reconstruction of the events.

To reject non-collision events, vertex information is used. To reconstruct vertices, tracks fulfilling certain quality requirements are clustered into vertices with a deterministic annealing algorithm [66, 13]. The vertex position is fitted using an adaptive vertex fitter [67], where a weight w_i between 0 and 1 is assigned to every track, based on the likelihood of that track being correctly associated with the vertex. The presence of at least one primary vertex is required whose distance to the interaction point is less than $24\,\mathrm{cm}$ in z direction and $2\,\mathrm{cm}$ in

category	process	generator	cross section [pb]	processed events	weight
$t\bar{t}$	$t\bar{t} \to b\bar{b}l\nu l\nu$	Madgraph	22.40	11952631	0.04
	$t\bar{t} \to b\bar{b}q\bar{q}l\nu$	Madgraph	88.60	24913744	0.07
	$t\bar{t} \to b\bar{b}q\bar{q}q\bar{q}$	Madgraph	88.80	31172356	0.06
Drell-Yan	$Z/\gamma^* \to l^+l^-$ 10 GeV $< m_{ll} <$ 50 GeV	Madgraph	876.80	7132223	2.43
	$Z/\gamma^* \to l^+l^-$ $m_{ll} >$ 50 GeV	Madgraph	3532.80	30000624	2.33
W	$W \to l\nu$	Madgraph	37509.00	55996720	13.26
WW,WZ,ZZ	$ZZ \to l^+l^-q\bar{q}$	Madgraph	2.45	1936727	0.03
	$ZZ \to l^+l^-\nu\nu$	Madgraph	0.36	954911	0.01
	$ZZ \to l^+l^-l^+l^-$	Madgraph	0.18	4789250	0.00
	$WZ \to l\nu l^+l^-$	Madgraph	1.06	2017979	0.01
	$WZ \to qq'l^+l^-$	Madgraph	2.32	3205557	0.01
	$WW \to l\nu l\nu$	Madgraph	5.81	1933235	0.06
single top	t s-Channel	Powheg	3.79	259961	0.29
	t t-Channel	Powheg	56.40	3746457	0.30
	t tW-Channel	Powheg	11.10	497658	0.44
	$\bar{t}$ s-Channel	Powheg	1.76	139974	0.25
	$\bar{t}$ t-Channel	Powheg	30.70	1935072	0.31
	$\bar{t}$ tW-Channel	Powheg	11.10	493460	0.45
Other SM	WWW	Madgraph	0.08	220549	0.01
	$WW\gamma$	Madgraph	0.53	215121	0.05
	WWZ	Madgraph	0.06	222234	0.01
	WZZ	Madgraph	0.02	219835	0.00
	$t\bar{t}\gamma$	Madgraph	2.17	71598	0.60
	$t\bar{t}W$	Madgraph	0.23	196046	0.02
	$t\bar{t}Z$	Madgraph	0.21	210160	0.02
	$t\bar{t}WW$	Madgraph	0.00	217820	0.00
$t\bar{t}$ Systematics	$t\bar{t}$	Madgraph	227.00	6923750	0.65
	$t\bar{t}$, $m_{top} =$ 166.5 GeV	Madgraph	227.00	4469095	1.01
	$t\bar{t}$, $m_{top} =$ 169.5 GeV	Madgraph	227.00	5202817	0.86
	$t\bar{t}$, $m_{top} =$ 175.5 GeV	Madgraph	227.00	5186494	0.87
	$t\bar{t}$, $m_{top} =$ 178.5 GeV	Madgraph	227.00	4723379	0.95
	$t\bar{t}$, Matching scale up	Madgraph	227.00	5393645	0.83
	$t\bar{t}$, Matching scale down	Madgraph	227.00	5467170	0.82
	$t\bar{t}$, Factorization scale up	Madgraph	227.00	5009488	0.90
	$t\bar{t}$, Factorization scale down	Madgraph	227.00	5377388	0.84

Table 4.4.: Simulated datasets used in the analysis. The samples are grouped by physics processes and information about the generator, the cross section of the processes, the number of processed events, and the resulting weight used to scale the simulation to the recorded luminosity are given.

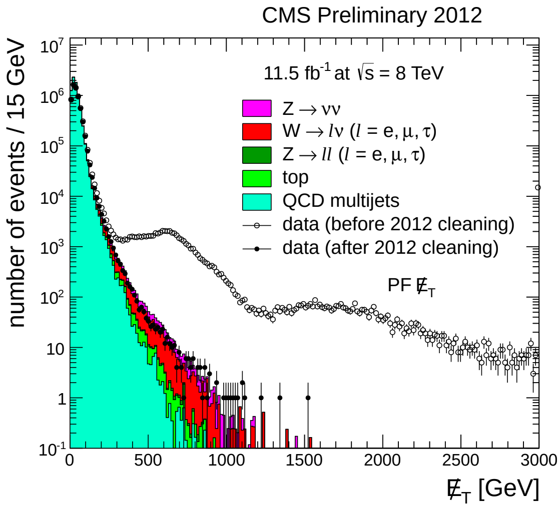

Figure 4.3.: Distribution of $E_{\mathrm{T}}^{\mathrm{miss}}$ in dijet events in 2012 data. The open data points show all events, while the black points show the data after application of $E_{\mathrm{T}}^{\mathrm{miss}}$ filters. Simulated Standard Model processes are shown as filled histograms. [29].

the x-y plane. Also the number of degrees of freedom, defined as [13]:

$$n_{dof} = -3 + 2 \sum_{i=1}^{N_{tracks}} w_i, \tag{4.11}$$

is required to be greater than four.

As it relies on the balance of all reconstructed objects, $E_{\mathrm{T}}^{\mathrm{miss}}$ is especially sensitive to distortions of the event reconstruction by noise or particles not originating from the proton proton collisions. Several sources of these distortions have been identified during the data taking and filters have been developed in CMS to reject events matching their signatures [29]. This includes filters for signal produced by interactions of the beam with gas molecules in the beam pipe or of protons in the beam halo with the LHC infrastructure, anomalous noise in the HCAL or ECAL, dead ECAL cells, calibration lasers mistakenly firing during collision events, or failures of the tracking algorithms. The effect of these filters on the tails of the $E_{\mathrm{T}}^{\mathrm{miss}}$ distribution in dijet events is shown in Figure 4.3, where it can be seen that it is dominated by events that are rejected by the filters for $E_{\mathrm{T}}^{\mathrm{miss}}$ larger than $300\,\mathrm{GeV}$.

4.3.2. Inclusive dilepton selection

Events are selected containing two isolated leptons with opposite electric charge, p_{T} larger than $20\,\mathrm{GeV}$, and $|\eta|$ smaller than 2.4. The choice of the isolation requirement of 15% of the lepton p_{T} is illustrated on the left side of Figure 4.4, where the distribution of the relative isolation is shown for the trailing lepton in $t\bar{t}$ simulation. Using the MC truth information the sample is split into prompt leptons originating from W boson decays, leptons originating from heavy flavour hadron decays inside b-quark jets, and jets misreconstructed as leptons. The prompt leptons are concentrated at very low values, but a long tail extends to much higher values. The leptons from heavy flavour decays are less well isolated, with a broad maximum of the distribution between 0.5 and 1. Misreconstructed leptons are spread more evenly between high and low values of isolation. The cut value of 0.15 allows for a strong suppression of non-prompt leptons while a high efficiency is retained for prompt leptons. The isolation efficiency as a function of the number of reconstructed vertices is shown on the right side of Figure 4.4 separately for prompt electrons and muons in $t\bar{t}$ and $Z+\text{jets}$ events. The efficiency in $Z+\text{jets}$ evens is about 5 percentage points higher in $Z+\text{jets}$ events compared to the more hadronic environment of $t\bar{t}$ events. While the efficiency shows only a slight dependency on the number of vertices and therefore on the amount of pileup, whereas for muons a more strong decrease of efficiency is observed for high numbers of vertices. However, for $t\bar{t}$ events this is much less pronounced, as the efficiency is already diminished by the higher number of jets in this environment. The good separation of prompt and non-prompt leptons and the high efficiency for prompt leptons are therefore retained even in the challenging conditions at the LHC.

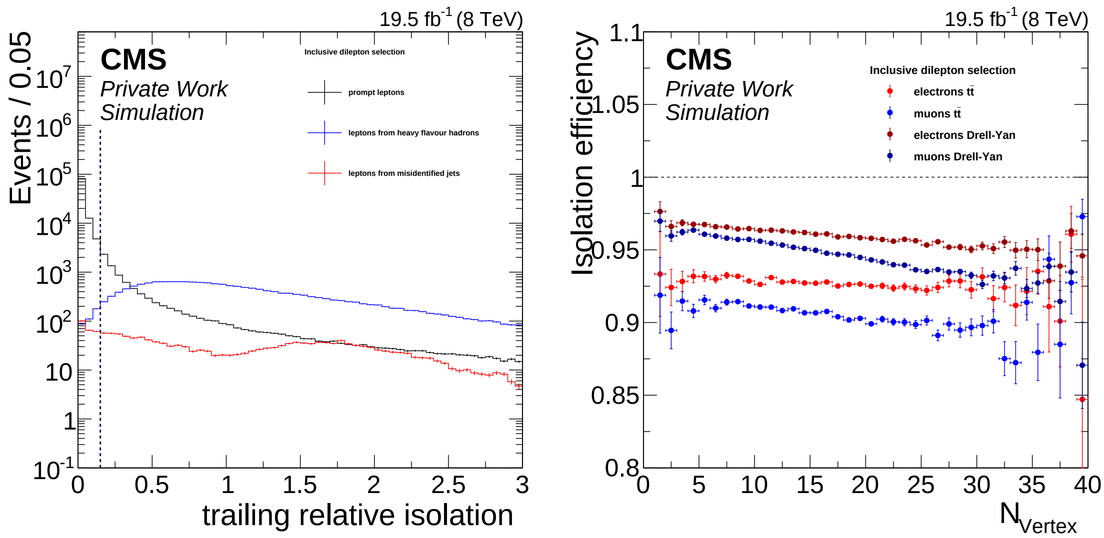

Figure 4.4.: On the left the distribution of the pileup corrected relative isolation of the trailing lepton for prompt leptons, leptons from heavy flavour decays, and misidentified jets in $t\bar{t}$ simulation is shown. On the right side the efficiency for a prompt lepton to pass the isolation requirement is shown as a function on the reconstructed number of vertices for both $t\bar{t}$ and $Z+\text{jets}$ simulation.

The p_T requirement is driven by the thresholds of the dilepton triggers, as discussed in Section **??**, while the $|\eta|$ restriction is imposed by the coverage of the muon system. The acceptance for electrons could in principle be extended to $|\eta| = 2.5$, but is chosen to be the same for both lepton flavours. Lepton pairs are required to be selected by the corresponding trigger, e.g. a pair of electrons has to have fired the dielectron trigger. If there is more than one pair of leptons fulfilling this basic requirements in one event, the pair with the largest sum of lepton p_T is chosen.

As the symmetry between lepton flavours is a key ingredient of the methods to estimate the backgrounds from Standard Model processes, events for which these symmetries are potentially violated are rejected.

As the efficiency to reconstruct electrons is reduced in the overlap region between the barrel and endcap detectors of the ECAL, the relative event yield for events with electrons with $|\eta|$ between 1.4 and 1.6 is reduced compared to those with muons in this range. This distribution of the $|\eta|$ of the leading lepton in $e^{\pm}e^{\mp}$ and $\mu^{\pm}\mu^{\mp}$ events is shown in Figure 4.5 (left), illustrating the greatly increased difference between the event yields for electrons and muons in the overlap region. Events containing a lepton with a pseudorapidity of $1.4 < |\eta| < 1.6$ are therefore rejected. Also an increasing difference between electrons and muons can be seen for events were the leading leptons is in the endcap region of the detector. This is one of the reasons for splitting the event sample in two categories: *central*, where both leptons are reconstructed with $|\eta| < 1.4$ and *forward*, where at least one leptons has to be reconstructed with $|\eta| > 1.6$.

Leptons with small spatial separation can interfere with each other's reconstruction and isolation. These effects are different for electrons and muons, which can be seen in Figure 4.5 (right). The ratio of electrons to muons first rises for lower values of $\Delta R(ll)$ before dropping for values below 0.1. The leptons are therefore required to be separated in $\Delta R(ll)$ by more than 0.3. Some differences between electrons and muons can also be observed for very high values of $\Delta R(ll)$, but they are less pronounced and this region is less populated.

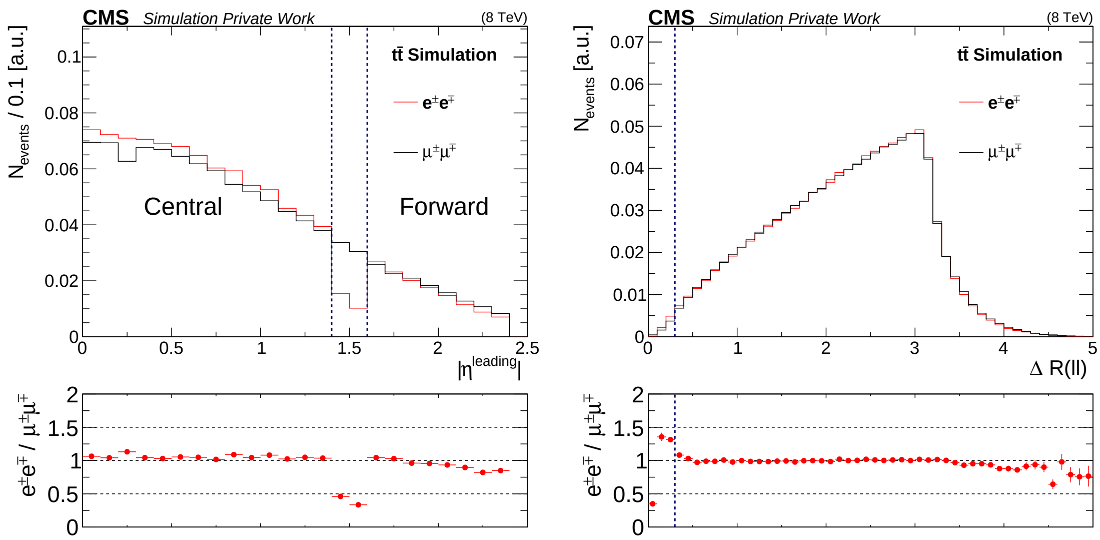

Figure 4.5.: istribution of $|\eta|$ (left) and $\Delta R(ll)$ (right) for the leading lepton for $\mu^{\pm}\mu^{\mp}$ (black dots) and $e^{\pm}e^{\mp}$ (red dots) events in a simulation of $t\bar{t}$ events. Both distributions are normalized to the same area.

As an additional requirement, to avoid possible reconstruction problems events with low lepton momenta and to avoid contamination from dilepton production in the decay of the bottonium resonances, the dilepton invariant mass $m_{\ell\ell}$ is required to be greater than $20\,\mathrm{GeV}$.

4.3.3. Selections in $E_{\mathrm{T}}^{\mathrm{miss}}$ and jet multiplicity

Three subsets of the event sample obtained with the inclusive dilepton selection are defined, resulting in samples enriched in different processes. The variables used in the definitions of these regions are $E_{\mathrm{T}}^{\mathrm{miss}}$ and the number of selected jets N_{jets}. The selections are illustrated in the plots of Figure 4.6, which also show the distribution of $t\bar{t}$ (left) and Drell-Yan (right) events in the $E_{\mathrm{T}}^{\mathrm{miss}}$-$N_{jets}$ plane.

The signal region, in which the search will be performed, is defined by requiring either $N_{jets} \geq 3$ and $E_{\mathrm{T}}^{\mathrm{miss}} > 100\,\mathrm{GeV}$ or $N_{jets} \geq 3$ and $E_{\mathrm{T}}^{\mathrm{miss}} > 100\,\mathrm{GeV}$. This definition allows to select signal events for points in the parameter space where more energy is distributed to the jets and less to the invisible component of the signature and vice versa. At the same time the rejection of background events with both lower N_{jets} and $E_{\mathrm{T}}^{\mathrm{miss}}$ is maintained. A control region dominated by flavour-symmetric processes is defined by selecting events with $N_{jets} = 2$ and $100\,\mathrm{GeV} < E_{\mathrm{T}}^{\mathrm{miss}} < 150\,\mathrm{GeV}$.

To study lepton pairs produced via the Drell-Yan process and to obtain a high statistics sample of leptons for efficiency measurements, events with $N_{jets} \geq 2$ and $E_{\mathrm{T}}^{\mathrm{miss}} < 50\,\mathrm{GeV}$ are selected. The N_{jet} requirement greatly reduces the statistics and the purity of this event sample. However, because of the large cross section of the Drell-Yan process, the event yield is still sufficient for the purposes of this analysis and Drell-Yan events dominate over those from $t\bar{t}$ production by two orders of magnitude. This allows to select events with kinematics close to those of the signal selection in terms of jet multiplicity.

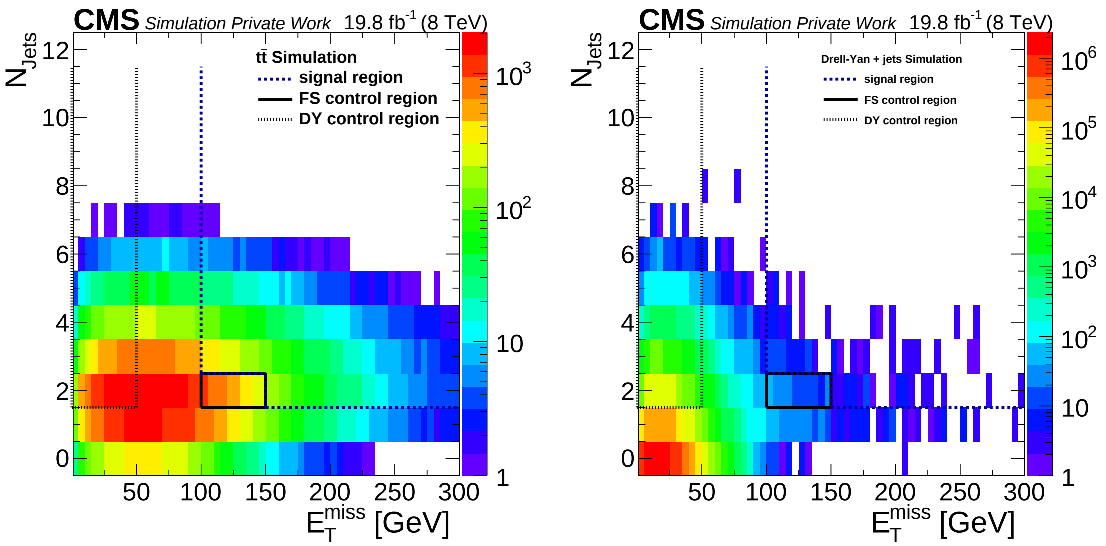

Figure 4.6.: Distribution of backgrounds events in the $E_{\mathrm{T}}^{\mathrm{miss}}$-$N_{jets}$ plane for $t\bar{t}$ (left) and Drell-Yan (right) events from Simulation. The events are weighted according to the cross section of the process and the size of the generated event sample, assuming an integrated luminosity of $19.5 fb^{-1}$. The three regions defined in the plane are indicated by lines.

5. Estimation of Standard Model backgrounds

As indicated in Figure 4.6, different Standard Model processes contribute to the event sample in the signal region. To distinguish a potential signal from these backgrounds, a precise estimation of the background contributions is mandatory. While the simulation of these processes and the response of the CMS detector gives a good description of the data for the majority of the phase space, a large number of uncertainty sources are introduced in the modelling of the physical process and the detector. Therefore a higher precision can be achieved by deriving the background estimates directly from the recorded data. The background processes are categorized as either being flavour-symmetric or as containing the production of a Z boson. A dedicated method is applied for each of the two categories. The different background processes are:

5.1. Flavour-symmetric backgrounds

Processes that are symmetric in the production of same-flavour and opposite-flavour lepton pairs allow for the estimation of their contribution to the SF event sample from the OF one. The most dominant of these processes is the dileptonic decay of top-pair production, where the leptons are produced uncorrelatedly in the decay of the W bosons. Other examples are the decays of two τ leptons, which are in turn produced in the decay of a Z boson or the dileptonic decay of W pairs. Another contribution to this class of backgrounds are misidentified leptons, as will be demonstrated later.

No significant deviation from flavour-symmetry has been observed in the decays of the W boson, with a measured ratio of the branching fractions into $e+\nu$ and $\mu+\nu$ of 1.007 ± 0.021. In the decays of the τ lepton the different masses of electron and muon have a noticeable effect, resulting in a slightly favoured decay into electrons. Here the ratio of branching fractions is 1.0241 ± 0.0032 [38]. As backgrounds with τ leptons are a sub-dominant contribution to the the flavour-symmetric backgrounds, these can be considered to be fully flavour-symmetric on particle level. However, distortions of the flavour-symmetry are introduced by the different efficiencies for triggering, reconstructing, and identifying electrons and muons in CMS. The background estimation from OF events therefore has to include a correction for this deviation, which is applied as a multiplicative factor:

$$N_{SF}^{pred} = R_{\mathsf{SF/OF}} \cdot N_{OF}. \tag{5.1}$$

Similarly, the factors $R_{ee/\mathsf{OF}}$ and $R_{\mu\mu/\mathsf{OF}}$ are used to derive separate background estimates for the $e^{\pm}e^{\mp}$ and $\mu^{\pm}\mu^{\mp}$ channel separately. Two independent methods are utilized to measure $R_{\mathsf{SF/OF}}$ on data. In the first approach is is directly measured as the ratio of SF to OF events

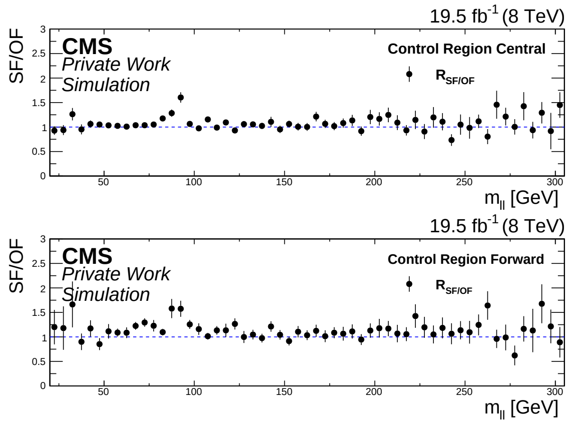

Figure 5.1.: Ratio of SF to OF events as a function of $m_{\ell\ell}$ in the $t\bar{t}$ control region in simulation. Shown are the results for the central (top) and forward (bottom) lepton selection.

in the control region for flavour-symmetric backgrounds. The second approach studies the lepton efficiencies and derives $R_{\mathsf{SF/OF}}$ factorized into the effects of trigger efficiencies and reconstruction and identification efficiencies.

5.1.1. Direct measurement of $R_{\mathsf{SF/OF}}$

The ratio of SF to OF events as a function of $m_{\ell\ell}$ in simulation is shown in Figure 5.1, separately for the central and forward lepton selection. The ratio is very close to on and independent of $m_{\ell\ell}$, except at the Z peak. It can be concluded that an universal factor can be applied for flavour-symmetric backgrounds over the full mass range. To exclude the Z peak from the calculation only events in the mass regions $20\,\mathrm{GeV} < m_{\ell\ell} < 70\,\mathrm{GeV}$ and $m_{\ell\ell} > 120\,\mathrm{GeV}$ are considered. The observed ratio on data as a functions of $m_{\ell\ell}$ is shown in Figure 5.2. Also here no significant dependence on $m_{\ell\ell}$ is observed both in the central and forward signal lepton selection. The numerical results are summarized in Table 5.1 for $R_{\mathsf{SF/OF}}$ as well as $R_{ee/\mathsf{OF}}$ and $R_{\mu\mu/\mathsf{OF}}$. Good agreement between the values measured in data and simulation is observed. The extrapolation of the measured value of $R_{\mathsf{SF/OF}}$ into the signal region is studied in simulation. No deviation of the values measured in the signal region from those obtained in the control region is observed within the statistical uncertainties of the simulation. This uncertainty is therefore assigned as an systematic uncertainty of the method.

5.1.2. Determination of $R_{\mathsf{SF/OF}}$ with the factorization method

Asymmetries between the lepton flavours introduced by differing reconstruction and selection efficiencies can be corrected for if the ratio of efficiencies for muons and electrons $r^*_{\mu e} = \frac{\epsilon_\mu}{\epsilon_e}$ is known. Here and in the following, the * indicates quantities that do not consider the effect of trigger efficiencies. They have therefore to be expressed in terms of the measurable event yields which include these effects. Under the assumption that the efficiencies for the two

Table 5.1.: Observed event yields in the control region and the resulting values of $R_{\mathsf{SF/OF}}$, $R_{ee/\mathsf{OF}}$, and $R_{\mu\mu/\mathsf{OF}}$. The results are shown separately for the central and forward lepton selection and the same quantities derived on simulation are shown for comaprison.

	N_{SF}	N_{OF}	$R_{\mathsf{SF/OF}} \pm \sigma_{stat}$	Transfer factor $\pm\sigma_{stat}$
	Central			
Data	1458	1448	1.007±0.037	–
MC	1410.5	1359.9	1.037±0.015	1.016±0.021
	Forward			
Data	545	537	1.015±0.062	–
MC	538.9	490.6	1.098±0.027	0.996±0.035
	N_{ee}	N_{OF}	$R_{ee/\mathsf{OF}} \pm \sigma_{stat}$	Transfer factor $\pm\sigma_{stat}$
	Central			
Data	663	1448	0.458±0.021	–
MC	614.1	1359.9	0.452±0.008	1.018±0.026
	Forward			
Data	239	537	0.445±0.035	–
MC	217.8	490.6	0.444±0.014	1.023±0.045
	$N_{\mu\mu}$	N_{OF}	$R_{\mu\mu/\mathsf{OF}} \pm \sigma_{stat}$	Transfer factor $\pm\sigma_{stat}$
	Central			
Data	795	1448	0.549±0.024	–
MC	796.3	1359.9	0.586±0.010	1.015±0.026
	Forward			
Data	306	537	0.570±0.041	–
MC	321.1	490.6	0.655±0.019	0.977±0.041

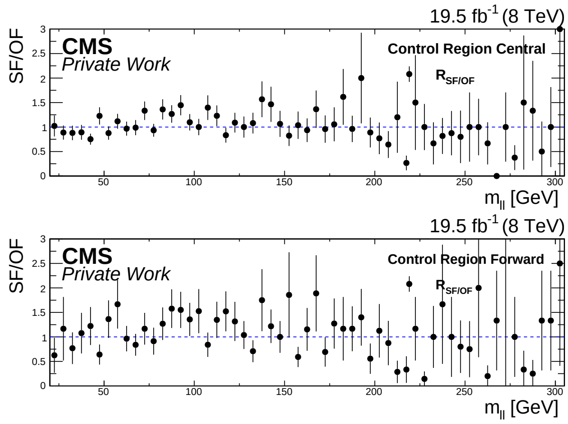

Figure 5.2.: Ratio of SF to OF events as a function of $m_{\ell\ell}$ in the $t\bar{t}$ control region in data. Shown are the results for the central (top) and forward (bottom) lepton selection.

leptons in the event factorize, i.e. $\epsilon_{ll} = \epsilon_l \cdot \epsilon_l$, the number of dielectron and dimuon events can be expressed in terms of the the opposite-flavour yield using the relations

$$N^*_{ee} = \frac{1}{2} \cdot \frac{N^*_{OF}}{r^*_{\mu e}} \tag{5.2}$$

and

$$N^*_{\mu\mu} = \frac{1}{2} \cdot r^*_{\mu e} \cdot N^*_{OF}. \tag{5.3}$$

The combined same-flavour yield is therefore given by

$$N^*_{SF} = \frac{1}{2} \cdot \left(r^*_{\mu e} + \frac{1}{r^*_{\mu e}} \right) N^*_{OF}. \tag{5.4}$$

In practice, all measured quantities are affected by the efficiencies of the different dilepton triggers. The observable SF yield is therefore given by

$$N_{SF} = \epsilon^T_{ee} \cdot N^*_{ee} + \epsilon^T_{\mu\mu} \cdot N^*_{\mu\mu}, \tag{5.5}$$

where ϵ^T_{ll} denotes the trigger efficiency for the given dilepton combination.
The trigger efficiencies also affect the calculation of N^*_{ee} and $N^*_{\mu\mu}$. To take this into account, $r^*_{\mu e}$ is expressed in terms of the measured value $r_{\mu e}$, which is derived from the $e^\pm e^\mp$ and $\mu^\pm\mu^\mp$ event yields in the Drell-Yan control region (see Section 5.1.2) as

$$r_{\mu e} = \sqrt{\frac{N_{\mu\mu}}{N_{ee}}} \approx \sqrt{\frac{\epsilon^2_\mu \epsilon^T_{\mu\mu}}{\epsilon^2_e \epsilon^T_{ee}}} = r^*_{\mu e} \cdot \sqrt{\frac{\epsilon^T_{\mu\mu}}{\epsilon^T_{ee}}}. \tag{5.6}$$

As a final step, it has to be considered, that the measured yield in the OF channel also includes the trigger efficiencies. Therefore, using $N_{OF} = \epsilon^T_{e\mu} \cdot N^*_{OF}$, the final expression for the yields in the same-flavour channels become

$$N_{ee} = \frac{1}{2 r_{\mu e}} \cdot \frac{\sqrt{\epsilon^T_{ee}\epsilon^T_{\mu\mu}}}{\epsilon^T_{e\mu}} N_{OF} = R_{ee/\mathsf{OF}} N_{OF} \tag{5.7}$$

and

$$N_{\mu\mu} = \frac{1}{2} r_{\mu e} \cdot \frac{\sqrt{\epsilon^T_{ee}\epsilon^T_{\mu\mu}}}{\epsilon^T_{e\mu}} N_{OF} = R_{\mu\mu/\mathsf{OF}} N_{OF}. \tag{5.8}$$

Finally, the combined prediction of the SF yield is

$$N_{SF} = \frac{1}{2}\left(r_{\mu e} + \frac{1}{r_{\mu e}}\right) \cdot \frac{\sqrt{\epsilon^T_{ee}\epsilon^T_{\mu\mu}}}{\epsilon^T_{e\mu}} N_{OF} = R_{\mathsf{SF/OF}} N_{OF}. \tag{5.9}$$

The factor $\frac{\sqrt{\epsilon^T_{ee}\epsilon^T_{\mu\mu}}}{\epsilon^T_{e\mu}}$ is denoted R_{T} in the following.

Measurement of $r_{\mu e}$

The measurement of $r_{\mu e}$ is performed in the Drell-Yan control region as the ratio of $\mu^\pm\mu^\mp$ to $e^\pm e^\mp$ events on the Z peak, requiring $60\,\mathrm{GeV} < m_{\ell\ell} < 120\,\mathrm{GeV}$. A comparison of the recorded data to the different contributions from Standard Model processes, estimated from simulation, is shown in Figure 5.3. The Drell-Yan process is the dominating source of events in this selection. Good agreement between data and simulation is observed, indicating a good understanding of this kinematic region by CMS. The results of the calculation of $r_{\mu e}$ are shown

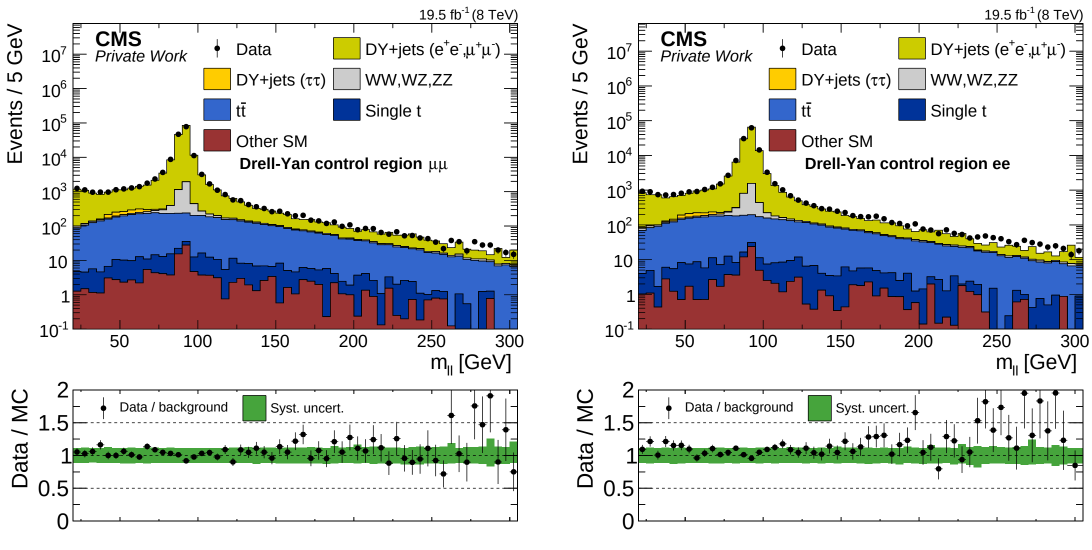

Figure 5.3.: Distribution of $m_{\ell\ell}$ in the Drell-Yan control region for $\mu^\pm\mu^\mp$ events (left) and $e^\pm e^\mp$ events (right). The data is shown as the black dots, while the contributions from Standard Model processes, estimated from simulation, are shown as the stacked histograms.

in Table 5.2. Given are the observed yields for $\mu^\pm\mu^\mp$ and $e^\pm e^\mp$ events and the resulting value of $r_{\mu e}$ with statistical and systematic uncertainties. In the central lepton selection, the $\mu^\pm\mu^\mp$ yield is about 18% higher than the $e^\pm e^\mp$ yield. Similar results are observed on Drell-Yan simulation. For events with leptons in the forward region, a larger asymmetry between muons and electrons is observed, here the $\mu^\pm\mu^\mp$ yield is about 40% higher than the $e^\pm e^\mp$ yield.

Table 5.2.: Result of the calculation of $r_{\mu e}$. Shown are the observed event yields in the Drell–Yan control region for the central and forward lepton selection in the $e^{\pm}e^{\mp}$ and $\mu^{\pm}\mu^{\mp}$ channels and the resulting values of mue. The same quantaties derived from simulation are shown for comparison.

	$N_{\mu\mu}$	N_{ee}	$r_{\mu e} \pm \sigma_{\text{stat.}} \pm \sigma_{\text{syst.}}$
	Central		
Data	98284	83035	1.09±0.01±0.11
MC	99719	82035	1.10±0.00±0.11
	Forward		
Data	62212	44437	1.18±0.01±0.24
MC	66327	45541	1.21±0.00±0.24

The systematic uncertainties assigned to the measured values of $r_{\mu e}$ are 10% for the central and 20% for the forward lepton selection. These values are obtained by studying the dependency of $r_{\mu e}$ on relevant observables. These are on the one hand properties of the lepton pairs, while on the other hand event properties as the jet multiplicity and $E_{\mathrm{T}}^{\mathrm{miss}}$ are studied to ensure the applicability of $r_{\mu e}$ in the signal region. The dependencies of $r_{\mu e}$ on $m_{\ell\ell}$, $E_{\mathrm{T}}^{\mathrm{miss}}$, and N_{jets} are shown in Figure 5.4. Some dependency is observed in the case of $m_{\ell\ell}$, where the values are higher for low $m_{\ell\ell}$ below the Z peak. This can be traced back to a dependency on the p_{T} of the leptons, where the efficiencies for muons have sharper turnons compared to electrons. In data, there is a strong effect visible around the Z peak for forward leptons. This is caused by a systematic shift of the position of the Z peak between electron and muons and is not a general property of $r_{\mu e}$, as is evident from the comparison with $t\bar{t}$ simulation shown in the upper right of Figure 5.4. No strong dependencies can be observed for $E_{\mathrm{T}}^{\mathrm{miss}}$ and N_{jets} within the statistical uncertainties. All observed deviations from the central values are covered by the systematic uncertainties assigned to the measurement. Further information on the dependency studies can be found in Appendix B.

Measurement of R_{T}

The trigger efficiencies are measured utilizing an event sample collected with PF H_T triggers. Lepton pairs corresponding to the flavour combination of the trigger in question are selected. To ensure that only correctly reconstructed events are considered in the calculation of the trigger efficiencies, the events are required to have $H_T > 200\,\mathrm{GeV}$, which corresponds to the lowest threshold applied in one of the PF H_T trigger. To ensure that the factorization method is performed on event samples complete orthogonal to the signal region and the $t\bar{t}$ enriched control region, events with $N_{jets} \geq 2$ and $E_{\mathrm{T}}^{\mathrm{miss}} > 100\,\mathrm{GeV}$ are rejected. As the offline lepton selection has more strict requirements compared to the one applied at HLT level, the dilepton triggers should have accepted all these events. The trigger efficiency is therefore defined as

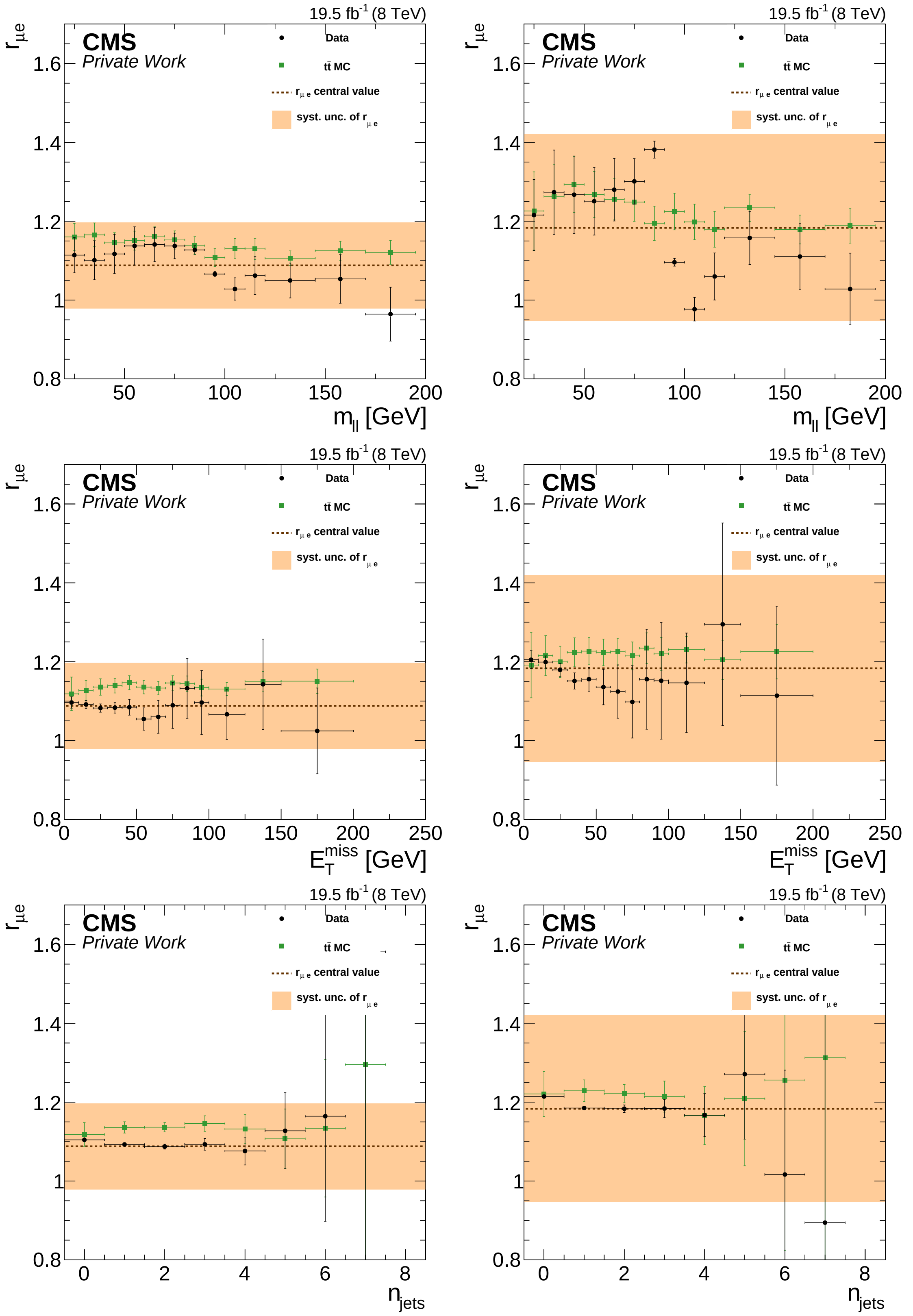

Figure 5.4.: Dependencies of $r_{\mu e}$ on $m_{\ell\ell}$ (top), $E_{\mathrm{T}}^{\mathrm{miss}}$ (middle), and N_{jets} (bottom) for the central (left) and forward (right) lepton selection. The results on data are shown in black while $t\bar{t}$ simulation is shown in green. The central value is shown as a brown dashed line while the systematic uncertainty is shown as an orange band.

the ratio of accepted events by the total number of events:

$$\epsilon_{ll}^{T} = \frac{N_{events}(\text{PF } H_T\text{trigger} \cap \text{dilepton selection} \cap \text{dilepton trigger})}{N_{events}(\text{PF } H_T\text{trigger} \cap \text{dilepton selection})}. \tag{5.10}$$

In the case of $\mu^{\pm}\mu^{\mp}$ and OF events, two triggers are used in the event selection. Therefore their combined efficiency is measured, requesting the logical OR of both. The resulting efficiencies are summarized in Table **??**, separately for the central and forward lepton selection. The trigger efficiencies for $e^{\pm}e^{\mp}$ and $\mu^{\pm}\mu^{\mp}$ are about 97% in both the central and forward selection. The efficiency for OF events is lower, about 95% in the central and 90% in the forward selection. This shows how the flavour symmetry is broken at trigger level by the inclusion of the `HLT_Mu17_TkMu8` trigger, which recovers efficiency for the trailing muon leg of the trigger and is not present in the OF triggers.

Table 5.3.: Triggerefficiency-values for data and MC with OS, $p_T > 20(20)$ GeV and $H_T > 200$ GeV for central and forward region seperated.

	nominator	denominator	$\epsilon_{trigger} \pm \sigma_{stat}$	nominator	denominator	$\epsilon_{trigger} \pm \sigma_{stat}$
	Data					
	Central			Forward		
ee	3592	3692	0.973±0.003	954	980	0.973±0.006
$\mu\mu$	1375	1420	0.968±0.005	547	566	0.966±0.009
eμ	493	521	0.946±0.012	102	114	0.895±0.037
	MC					
	Central			Forward		
ee	2912.8	2994.6	0.973±0.001	943.0	969.9	0.972±0.001
$\mu\mu$	3241.6	3287.9	0.986±0.000	1141.6	1183.4	0.965±0.001
eμ	6279.1	6523.1	0.963±0.000	2138.8	2249.0	0.951±0.001

To asses the systematic uncertainties of the trigger efficiency measurement, potential biases due to the choice of the orthogonal trigger are studied on simulation, using dileptonic $t\bar{t}$ events. On simulation the efficiency can be measured without the requirement of the PF H_T triggers, as no trigger is needed to select the events. The ratio of this true trigger efficiencies to those measured with the PF H_T triggers as a function of $m_{\ell\ell}$ is shown in Figure 5.5, separately for SF and OF events. In both cases all deviations from one are in the order of 0.1% and well compatible with it inside the statistical uncertainties. No bias of the efficiency measurement due to the PF H_T triggers is observed and therefore no systematic uncertainty due to this choice is assigned to the measurement. The turnon of the triggers at low lepton p_{T} is of particular interest because asymmetries between the lepton flavours are more likely to occur in this difficult environment. The dependence of the trigger efficiency on the p_{T} of the trailing lepton can be studied using datasets trigger by single lepton triggers. Triggers with p_{T} thresholds of $24(27)\,\mathrm{GeV}$ for muons (electrons) are available. These thresholds are relatively low for single lepton triggers, resulting in very strict selection criteria having to be applied on HLT level. Dilepton events are selected in which the leading lepton can be matched geometrically to the trigger object that fired the single lepton trigger. The trailing lepton is matched to trigger

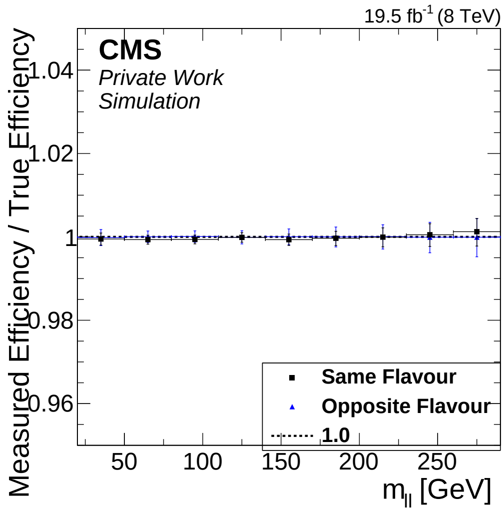

Figure 5.5.: Ratio of true trigger efficiencies to those calculated using the PF H_T triggers separately for SF and OF events.

objects that have fired the trailing leg of the dilepton trigger. The efficiency is defined as the number of events in which such a match can be found to the total number of dilepton events. The resulting efficiency curves are shown in Figure 5.6 for five different trailing lepton trigger legs and combining the central and forward selection. It can be seen that the efficiency for trailing electrons are virtually the same for the dielectron and OF triggers (black and light blue markers). The same is true for trailing muons in the dimuon and OF triggers (brown and dark blue markers). However, the efficiency for trailing muons in the `HLT_Mu17_TkMu8` trigger is significantly higher than those in the trigger paths not using the tracker information, as expected. Trailing muons have a much sharper turnon than trailing electrons, being fully efficient already at a p_{T} of $10\,\mathrm{GeV}$. For electrons the plateau is reached only above $\approx 30\,\mathrm{GeV}$. The turnon is steeper for trailing electrons in the dielectron trigger compared to those in the OF trigger, resulting in an increased deviation from flavour symmetry below $20\,\mathrm{GeV}$. As in the design of the analysis the precision and stability of the background prediction was given priority over lepton acceptance, events with trailing leptons in this p_{T} range are rejected. To asses the systematic uncertainties of the trigger efficiency measurement, the dependency of R_T as used in the calculation of $R_{\mathsf{SF/OF}}$ on different observables is tested. Here a dataset not triggered by α_T triggers is used, as the PF H_T triggers do not provide enough events for these studies. A 5% systematic uncertainty is assigned to each trigger efficiency, resulting in an uncertainty of 6.4% on R_T, covering all observed deviations from the the measured value of R_T within the statistical uncertainties, as shown in Figure5.7. Studies of further variables can be found in Appendix C

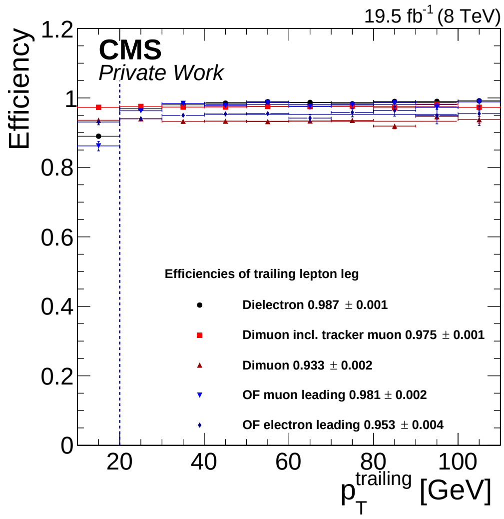

Figure 5.6.: Ratio of true trigger efficiencies to those calculated using the PF H_T triggers separately for SF and OF events.

Results of the factorization method

The results of the factorization methods are summarized in Table 5.4. The factor R_T is calculated from the trigger efficiencies in Table 5.3 as $R_T = \sqrt{\frac{\epsilon^T_{ee} \cdot \epsilon^T_{\mu\mu}}{\epsilon^T_{e\mu}}}$. The resulting correction factors $R_{\mathsf{SF/OF}}$, $R_{ee/\mathsf{OF}}$, and $R_{\mu\mu/\mathsf{OF}}$ are calculated as described in equations 5.7-5.9.

Table 5.4.

	Central		Forward	
	Data	MC	Data	MC
$r_{\mu e}$	1.088±0.109	1.139±0.114	1.183±0.237	1.249±0.250
R_T	1.026±0.066	1.017±0.064	1.084±0.079	1.018±0.065
$R_{\mathsf{SF/OF}}$	1.029±0.067	1.026±0.066	1.099±0.088	1.044±0.081
$R_{ee/\mathsf{OF}}$	0.471±0.116	0.447±0.119	0.458±0.259	0.408±0.256
$R_{\mu\mu/\mathsf{OF}}$	0.558±0.117	0.579±0.122	0.641±0.261	0.636±0.258

As for the direct measurements in the control region, the observed deviations of $R_{\mathsf{SF/OF}}$ from one are small and inside the uncertainties of the method. Because the uncertainty on $r_{\mu e}$ cancels out to a large degree in the calculation $R_{\mathsf{SF/OF}}$, the total uncertainty is dominated by the uncertainty on R_T, while for $R_{ee/\mathsf{OF}}$ and $R_{\mu\mu/\mathsf{OF}}$ the uncertainty of $r_{\mu e}$ is the dominant one. This results in much larger uncertainties on the latter two factors. The dependency of $R_{\mathsf{SF/OF}}$ on $r_{\mu e}$ and R_T is illustrated in Figure 5.8. The measured values of $r_{\mu e}$ and $R_{\mathsf{SF/OF}}$ are shown as straight lines, surrounded by bands indicating their uncertainties. The red line shows the value of $R_{\mathsf{SF/OF}}$ corresponding to a given $r_{\mu e}$, under the assumption that the trigger

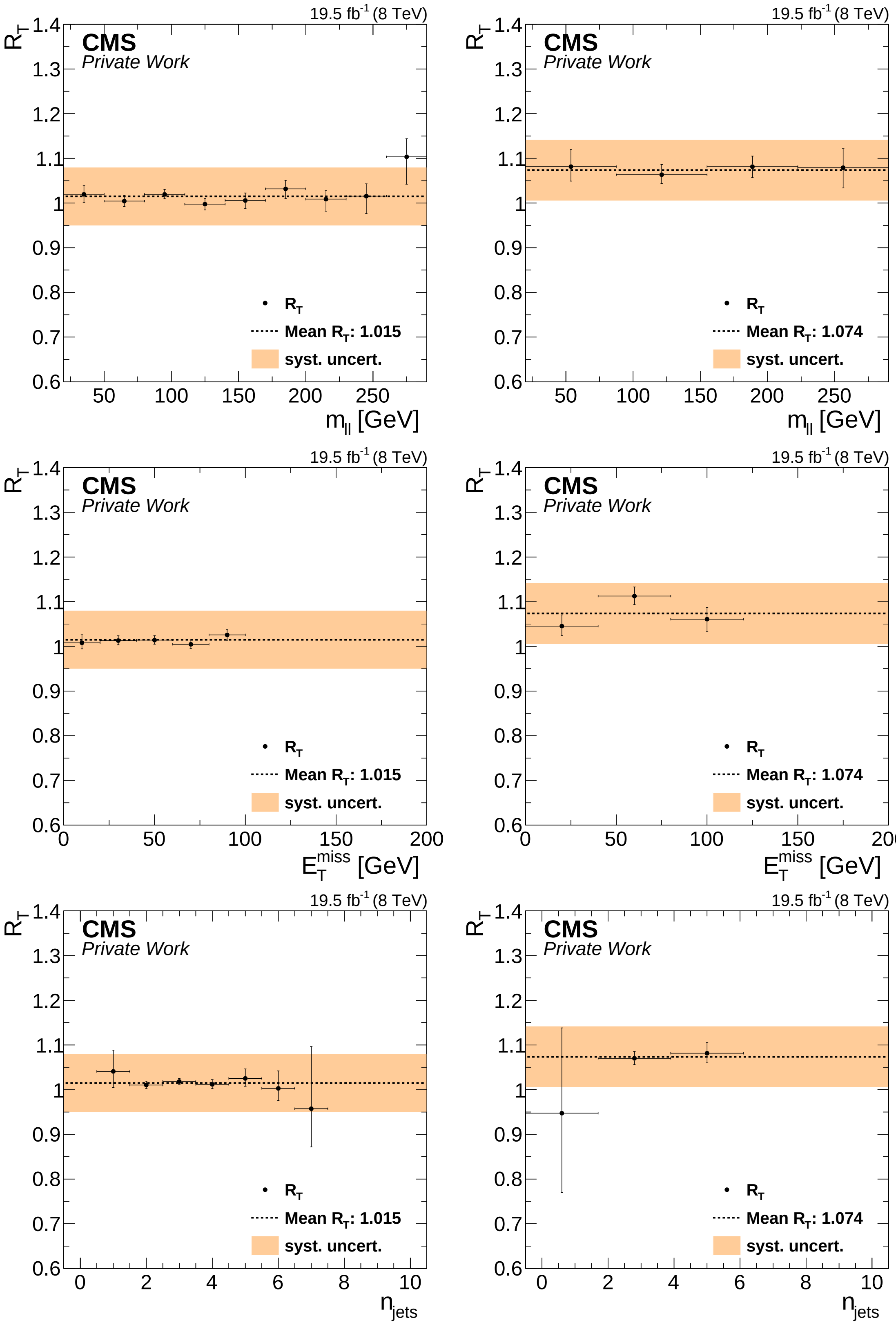

Figure 5.7.: Dependencies of R_T on $m_{\ell\ell}$ (top), $E_{\mathrm{T}}^{\mathrm{miss}}$ (middle), and N_{jets} (bottom) for the central (left) and forward (right) lepton selection. The results on data are shown in black. The central value is shown as a black dashed line while the systematic uncertainty is shown as an orange band.

efficiencies stay constant. The dashed black lines show the impact that the uncertainties on the trigger efficiencies have on the resulting $R_{\mathrm{SF/OF}}$. It can be seen that variations of $r_{\mu e}$ inside its systematic uncertainties have only little effect on $R_{\mathrm{SF/OF}}$, while changes in the trigger efficiencies have a much larger impact.

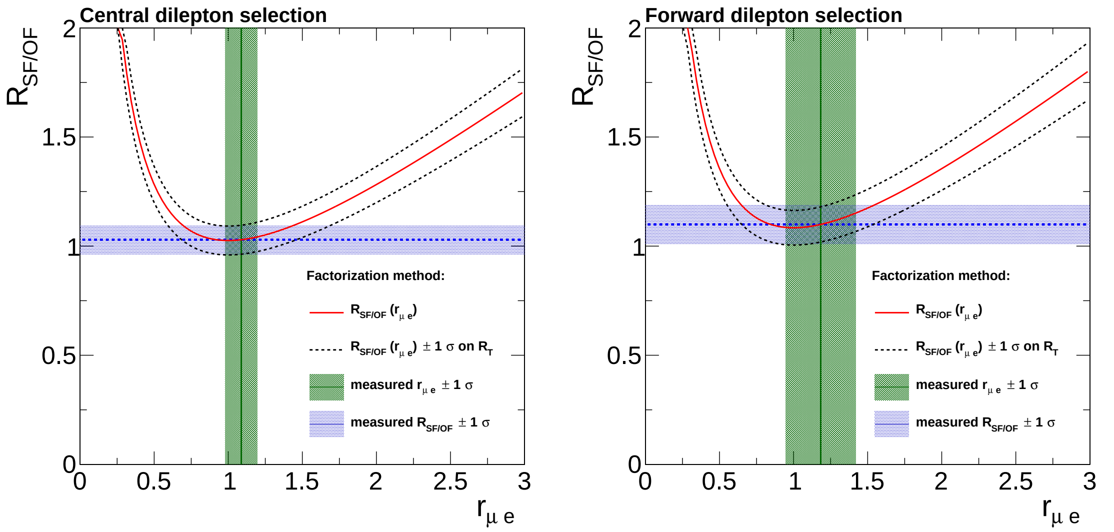

Figure 5.8.: Dependency of $R_{\mathrm{SF/OF}}$ on $r_{\mu e}$ in the factorization method. The measured central values of $R_{\mathrm{SF/OF}}$ and $r_{\mu e}$ and their uncertainty are shown as the blue and green lines and bands. The red line illustrates the value of $R_{\mathrm{SF/OF}}$ for a given $r_{\mu e}$ if R_T is kept constant. The impact of a variation of R_T within its uncertainties on $R_{\mathrm{SF/OF}}$ is shown by the dashed black lines.

5.1.3. Combined correction factors and resulting background estimates

An overview of the resulting corrections factors of the measurement in the control region and the factorization method are shown in Table 5.5. In all cases the results of the two methods agree very well within their uncertainties. Given the fact that they are performed on exclusive datasets and under the assumption that their uncertainties follow a Gaussian distribution, which is justified by the fact that they are either statistical in nature or assigned to cover statistical fluctuations in the dependency studies of $r_{\mu e}$ and R_T, they can be combined using a weighted average.

A precision of about 4% and 6% on the translation from opposite flavour to same flavour is reached in the central and forward dilepton selection, respectively. Separating the lepton flavours, the uncertainty in $R_{ee/\mathrm{OF}}$ and $R_{\mu\mu/\mathrm{OF}}$ is about 6% for central and 9-10% for forward leptons. This increase is caused by the missing cancellation of the uncertainty on $r_{\mu e}$ and the increased statistical uncertainty in the direct measurement in the control region. Given that the weighted average is calculated separately for each flavour combination, $R_{ee/\mathrm{OF}}$ and $R_{\mu\mu/\mathrm{OF}}$ do not add up exactly to $R_{\mathrm{SF/OF}}$, which in turn means that the sum of the background estimates for flavour-symmetric backgrounds in the $e^{\pm}e^{\mp}$ and $\mu^{\pm}\mu^{\mp}$ channels does not equal that in the SF channel. The OF yields in the $m_{\ell\ell}$ bins of the counting experiment together with the resulting background estimates in the different dilepton channels are shown in Table 5.6.

Table 5.5.

	$R_{\mathrm{SF/OF}}$			
	Central		Forward	
	Data	MC	Data	MC
from factorization method	1.029±0.067	1.026±0.066	1.099±0.088	1.044±0.081
from direct measurement	1.007±0.043	1.037±0.015	1.015±0.106	1.098±0.027
weighted avarage	1.013±0.036	1.037±0.015	1.048±0.055	1.099±0.026
	$R_{ee/\mathrm{OF}}$			
	Central		Forward	
	Data	MC	Data	MC
from factorization method	0.471±0.116	0.447±0.119	0.458±0.259	0.408±0.256
from direct measurement	0.458±0.034	0.452±0.008	0.445±0.092	0.444±0.014
weighted avarage	0.459±0.027	0.452±0.008	0.445±0.045	0.444±0.014
	$R_{\mu\mu/\mathrm{OF}}$			
	Central		Forward	
	Data	MC	Data	MC
from factorization method	0.558±0.117	0.579±0.122	0.641±0.261	0.636±0.258
from direct measurement	0.549±0.035	0.586±0.010	0.570±0.095	0.655±0.019
weighted avarage	0.550±0.030	0.586±0.010	0.572±0.050	0.655±0.019

Table 5.6.: Resulting estimates for flavour-symmetric backgrounds. Given is the observed event yield in $e^{\pm}\mu^{\mp}$ events and the resulting estimate after applying the correction, seperately for the SF, $e^{\pm}e^{\mp}$, and $\mu^{\pm}\mu^{\mp}$ channels. Statistical and systematic uncertainties are given separately. Low-mass refers to $20 < m_{\ell\ell} < 70$ GeV, on-Z to $81 < m_{\ell\ell} < 101$ GeV and high-mass to $m_{\ell\ell} > 120$ GeV.

	Low-mass		On-Z		High-mass	
	Central	Forward	Central	Forward	Central	Forward
Observed OF events	737	138	364	131	779	393
Estimate in SF channel	$746 \pm 27 \pm 26$	$144 \pm 12 \pm 7$	$368 \pm 19 \pm 13$	$137 \pm 11 \pm 7$	$789 \pm 28 \pm 28$	$411 \pm 20 \pm 21$
Estimate in $e^{\pm}e^{\mp}$ channel	$337 \pm 12 \pm 19$	$61 \pm 5 \pm 6$	$166 \pm 8 \pm 9$	$58 \pm 5 \pm 5$	$357 \pm 12 \pm 21$	$175 \pm 8 \pm 17$
Estimate in $\mu^{\pm}\mu^{\mp}$ channel	$405 \pm 14 \pm 21$	$79 \pm 6 \pm 6$	$200 \pm 10 \pm 10$	$74 \pm 6 \pm 6$	$428 \pm 15 \pm 23$	$224 \pm 11 \pm 19$

5.1.4. Validation of background estimates

To judge the performance of the estimation methods for flavour-symmetric backgrounds, they are applied to simulation. In Table 5.7 the resulting SF and OF yields after application of the signal selection are shown separately for the central and forward dilepton selection. The OF yields are corrected with the $R_{\text{SF/OF}}$ values derived for MC shown in Table 5.5. For completely flavour-symmetric processes, such as $t\bar{t}$, Drell–Yan production decaying to $\tau\tau$ or single top-quark production, the difference between the SF and OF yields is compatible with zero within the statistical uncertainties of the simulation and the systematic uncertainties of the method. Other systematic uncertainties affecting the simulation are the same for SF and OF lepton pairs and are therefore not considered here.

Table 5.7.: Event yields in the signal region in simulation for both SF and OF lepton pairs. The OF yield is multiplied with $R_{\text{SF/OF}}$ and the uncertainty on the OF yields includes the systematic uncertainty on $R_{\text{SF/OF}}$.

	Central			Forward		
	SF	OF	SF-OF	SF	OF	SF-OF
$t\bar{t}$	2189±9	2183±32	6±34	681±5	680±16	0±17
DY + jets ($e^{\pm}e^{\mp}$,$\mu^{\pm}\mu^{\mp}$)	48±10	0±0	48±10	23±8	3±3	19±8
DY + jets ($\tau\tau$)	71±13	58±11	13±17	14±5	17±6	-3±8
Single t	143±8	137±8	5±11	37±4	43±4	-5±6
WW	63±2	66±2	-3±3	30±1	30±1	0±2
WZ	39±0	8±0	30±0	14±0	3±0	10±0
ZZ	18±0	1±0	17±0	7±0	0±0	6±0
Other SM without Z bosons	66±5	69±5	-3±8	23±3	18±2	5±4
Other SM with Z bosons	23±0	11±0	11±0	6±0	3±0	2±0
Total MC simulation	2664±22	2537±40	126±46	837±12	801±21	36±25

As expected, deviations from flavour-symmetry are observed only for processes containing a Z boson, most notable Drell–Yan production decaying to light leptons, but also WZ or ZZ production and more rare processes like $t\bar{t}$Z production. It can therefore be concluded that the background prediction for flavour-symmetric processes performs well within the uncertainties of the methods presented above. The validity of this cross check is restricted to processes well modelled in simulation. As the modelling of non-prompt leptons is in general less reliable, more detailed studies are performed on data to ensure that flavour-symmetry also holds for the small contribution of non-prompt leptons to the final event selection.

Study of non-prompt leptons

As a preface to studies performed on data, the contribution of non-prompt leptons is examined using MC truth information. A data driven estimate for this contribution is derived from leptons with relaxed isolation criteria.

Non-prompt leptons in simulation The origin of the leptons in the events contribution to the signal selection is studied in simulation by matching the reconstructed lepton to the generated particles with the smallest spatial separation ΔR. The difference in generated and reconstructed p_{T} must not exceed twice the generated p_{T}. The parentage of the matched generated particle is used to determine of the lepton originates from a prompt decay, a heavy flavour decay inside a jet, or a jet that was misreconstructed as a lepton. The contribution of non-prompt leptons to the signal selection is studied in $t\bar{t}$ events, where the two b-jets are a source for leptons from heavy flavour decays.

All events where at least one of the leptons is not matched to a generated electron or muon and/or does not originate directly or via and intermediate τ lepton from a W boson are considered non-prompt. The resulting $m_{\ell\ell}$ distributions are shown in Figure 5.9 for an inclusive dilepton selection on the left and the combined central and forward signal selection on the right. Good agreement between SF and OF pairs can be seen, with a slight tendency towards OF. The event yields are summarized in Table 5.8. It can be seen that the contribution of non-

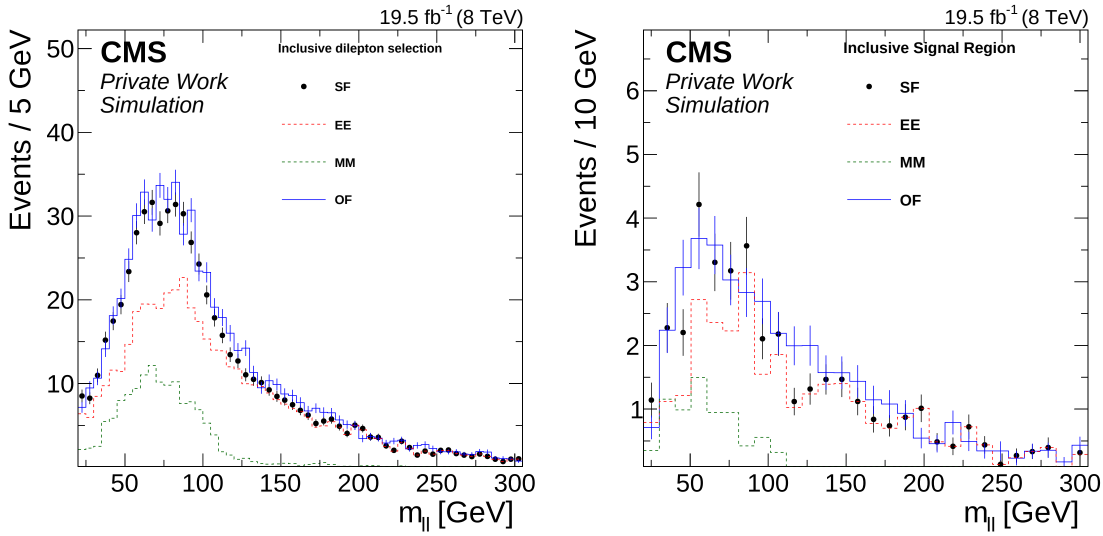

Figure 5.9.: Distribution of $m_{\ell\ell}$ for lepton pairs with at least one non-prompt lepton in simulation for an inclusive dilepton selection (left) and the signal selection (right). The contributions of $e^{\pm}e^{\mp}$, $\mu^{\pm}\mu^{\mp}$, and $e^{\pm}\mu^{\mp}$ pairs are shown as red, green, and blue lines, respectively. The combined SF pairs are shown as the black points.

prompt electrons exceeds that of non-prompt muons. The event yields for SF and OF lepton pairs are very similar, with a slight preference to OF leptons. This indicates that this type of backgrounds is covered by the estimates for flavour-symmetric backgrounds, at least in simulation.

Estimate of non-prompt contributions with tight-to-loose ratios The contribution of non-prompt leptons to the signal selection can be estimated on data from control samples

Table 5.8.: Number of events with non-prompt leptons in an inclusive dilepton selection and the central and forward signal regions for $t\bar{t}$ simulation.

	$e^{\pm}e^{\mp}$	$\mu^{\pm}\mu^{\mp}$	SF	$e^{\pm}\mu^{\mp}$	$R_{\mathrm{SF/OF}}$
Inclusive	456.0±5.2	140.3±3.3	596.2±8.4	637.5±6.3	0.94±0.02
Signal central	20.2±1.0	4.9±0.6	25.0±1.6	26.2±1.2	0.95±0.07
Signal forward	9.8±0.7	2.8±0.5	12.6±1.2	14.2±0.9	0.89±0.10

enriched in non-prompt leptons.**FIXME:** Reference origin of method. Can I cite ANs? These samples are obtained by relaxing the isolation requirements on the leptons from requiring the relative isolation to be < 0.15 to < 1.0. The probability of a prompt or non-prompt lepton that passes this "loose" selection to also pass the default "tight" selection allows to calculate the different contributions of prompt-prompt, prompt-non-prompt and non-prompt-non-prompt dilepton events to the signal selection.

The probability for a non-prompt loose lepton to pass also the tight selection, often referred to as "fake rate" f is calculated in an event sample enriched in non-prompt leptons. It is collected by prescaled low-p_{T} single lepton trigger, see section **FIXME:** add this somewhere. At least one jet with $p_{\mathrm{T}} > 50\,\mathrm{GeV}$ is required. To reject prompt leptons from W + jets events, $E_{\mathrm{T}}^{\mathrm{miss}}$ and the transverse mass of the lepton-$E_{\mathrm{T}}^{\mathrm{miss}}$ system are both required to be $< 20\,\mathrm{GeV}$. The resulting fake rates as a function of lepton p_{T} and η are shown in Figure 5.10. For low p_{T}, the value for electrons is about 0.25 while for muons it is about 0.07. Dependencies on both p_{T} and η are observed. The fake rate is therefore measured and applied as a function of both variables. The increase for higher p_{T} is however understood as arising from an increasing contamination from prompt leptons. Therefore for all leptons with $\mathrm{p_T} > 40\,\mathrm{GeV}$, the values measured between $35\,\mathrm{GeV}$ and $40\,\mathrm{eV}$ are used. Similarly, to calculate the probability of a loose prompt lepton to be also a tight lepton, a sample enriched in prompt lepton is selected by requiring exactly two reconstructed leptons, of which the leading one is required to be a tight lepton which the trailing one is a loose lepton. To further enrich the sample in prompt lepton from Z boson decays, $m_{\ell\ell}$ is required to be within $15\,\mathrm{GeV}$ of the Z boson mass and $E_{\mathrm{T}}^{\mathrm{miss}}$ is required to be $< 20\,\mathrm{GeV}$. The resulting prompt ratios p are shown in Figure 5.11. They are again applied as functions of p_{T} η. The systematic uncertainty assigned to the tight-to-loose ratios in the sources cited above is 50%. As the definition of loose electrons differs from that used in said analyses and modifications have been made to the definition of the control samples in which the ratios are measured, this number is not directly applicable here. As the overall normalization of the non-prompt background is not the focus of this study, the uncertainty is increased to 100%.

Using the measured fake and prompt rates f and p, the contributions of the four possible combination of prompt and non-prompt lepton (prompt-prompt, prompt-non-prompt, non-

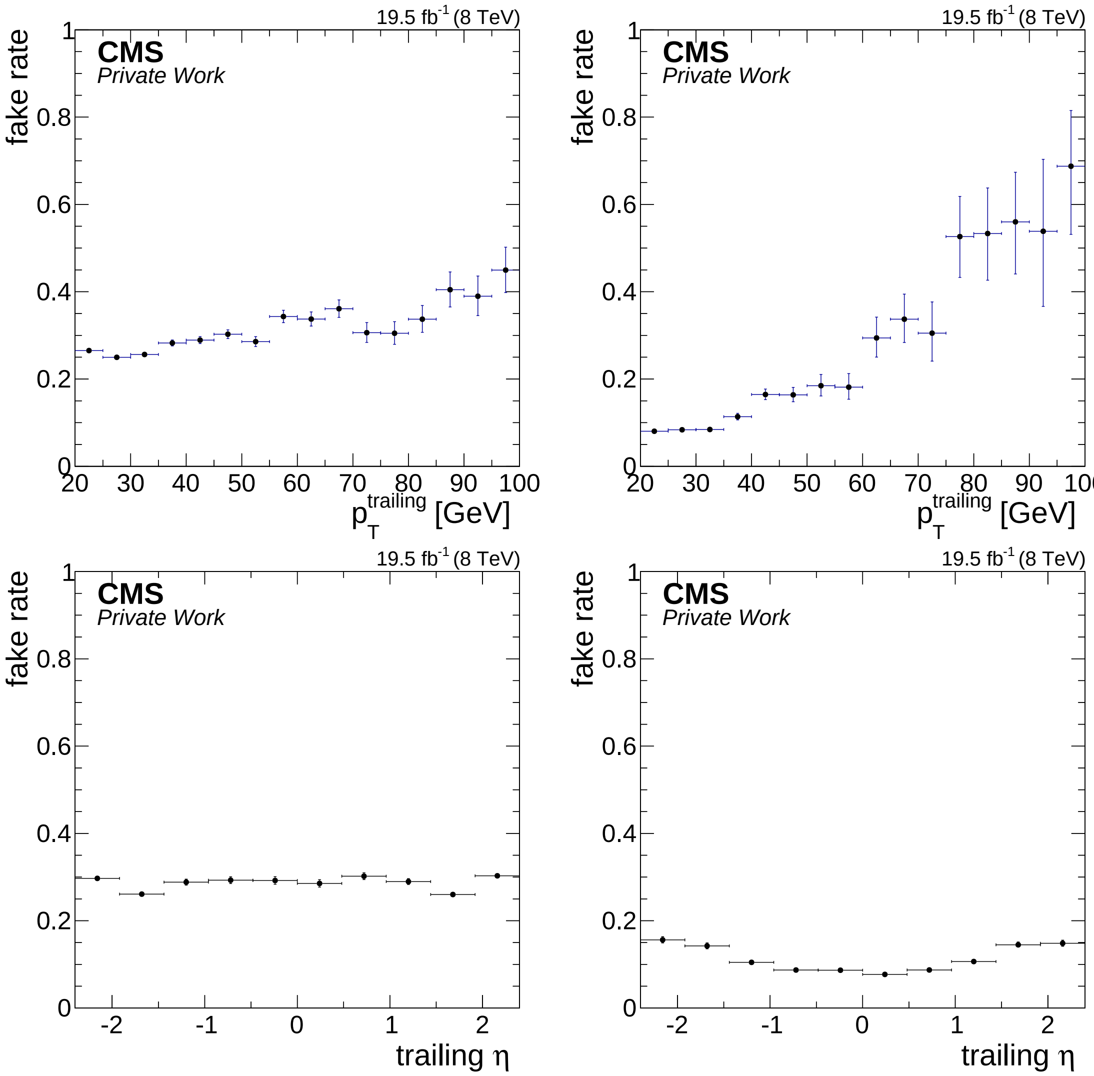

Figure 5.10.: Measured fake rate for electrons (left) and muons (right) as a function of the p_{T} (top) and η (bottom) of the trailing lepton.

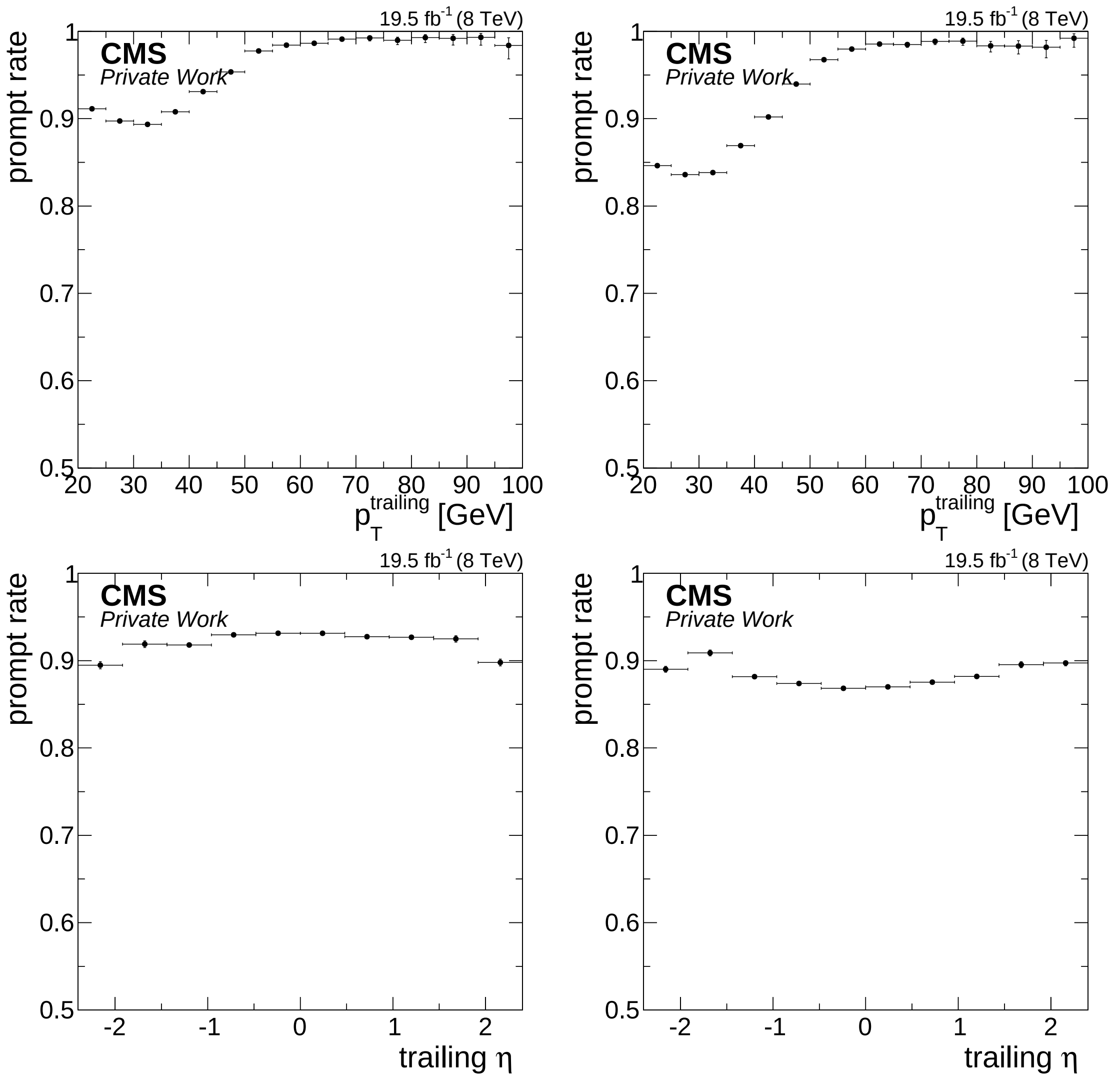

Figure 5.11.: Measured prompt rate for electrons (left) and muons (right) as a function of the p_{T} (top) and η (bottom) of the trailing lepton.

prompt-prompt, and non-prompt-non-prompt) are calculated using the following formulas

$$N_{pp} = N_{tt} \cdot (f_1 - 1)(f2 - 1)p_1p_2 + N_{tl} \cdot (f_1 - 1)f_2p_1p_2 + N_{lt} \cdot (f_2 - 1)f_1p_1p_2 + N_{ll} \cdot f_1f_2p_1p_2,$$
$$N_{pn} = N_{tt} \cdot (f_1 - 1)(1 - p_2)p_1f_2 - N_{tl} \cdot (f_1 - 1)f_2p_1p_2 + N_{lt} \cdot (1 - p_2)f_1p_1f_2 - N_{ll} \cdot f_1f_2p_1p_2,$$
$$N_{np} = N_{tt} \cdot (1 - p_1)(f_2 - 1)f_1p_2 + N_{tl} \cdot (1 - p_1)f_2f_1p_2 - N_{lt} \cdot (f_2 - 1)f_1p_1p_2 - N_{ll} \cdot f_1f_2p_1p_2,$$
$$N_{nn} = N_{tt} \cdot (1 - p_1)(1 - p_2)f_1f_2 - N_{tl} \cdot (1 - p_1)f_2f_1p_2 - N_{lt} \cdot (1 - p_2)f_1p_1f_2 + N_{ll} \cdot f_1f_2p_1p_2,$$

where each of the contributions has to be weighted by $(f_1 - p_1)(f_2 - p_2)$. As the fake and prompt rates depend on p_{T} and η of the leptons, in practice each event is assigned a weight based on whether the leptons are tight and loose and their kinematic properties according to the formulas above. The estimates for N_{pp}, N_{pn}, N_{np}, and N_{nn} are obtained as the sum of these weights. The total contribution of non-prompt backgrounds is than given by the sum of N_{pn}, N_{np}, and N_{nn}. The resulting estimates in the central and forward signal regions are shown in Table 5.9.

Table 5.9.: Results of the estimation of backgrounds with non-prompt leptons using the tight-to-loose ratio.

	$e^{\pm}e^{\mp}$	$\mu^{\pm}\mu^{\mp}$	SF	$e^{\pm}\mu^{\mp}$
	Signal central			
N_{tt}	1257	1450	2707	2326
$N_{lt} + N_{tl}$	247	740	987	812
N_{ll}	11	114	125	50
Non-prompt estimate	44.9±14.8±44.9	34.6±3.8±34.6	79.6±18.6±79.6	86.7±12.4±86.7
	Signal forward			
N_{tt}	405	473	878	827
$N_{lt} + N_{tl}$	130	233	363	234
N_{ll}	6	38	44	32
Non-prompt estiamte	27.3±8.0±27.3	17.9±3.5±17.9	45.1±11.5±45.1	43.4±8.4±43.4

It can be seen that the contribution of non-prompt leptons is small compared to the total number of tight lepton pairs and that the estimates are well compatible between SF and OF events within the statistical uncertainties. This type of backgrounds is therefore accounted for by the background estimates for flavour-symmetric backgrounds.

5.2. Backgrounds containing a Z boson

To estimate the contribution of backgrounds containing a Z boson to the event sample in the signal region, both the Jet-Z-balance (JZB) and $E_{\mathrm{T}}^{\mathrm{miss}}$ templates methods [68] are used. The first studies the balance of the Z boson against the jets in the event. In the $E_{\mathrm{T}}^{\mathrm{miss}}$ template method, the $E_{\mathrm{T}}^{\mathrm{miss}}$ distribution of γ+jets events are used to estimate that of Z+jets events. As the development and application of these methods have not been part of the work covered in this thesis, only a short description will be given.

5.2.1. JZB method

The JZB variable is defined as the balance of the p_{T} of the jets in the event with the p_{T} of the Z candidate. To avoid biases due to jet selection, $\vec{E}_{\mathrm{T}}^{\mathrm{miss}}$ is used as a measure of the hadronic recoil of the Z:

$$\mathrm{JZB} = |\sum_{\mathrm{jets}} \vec{p}_{\mathrm{T}}| - |\vec{p}_{\mathrm{T}}^{\,\mathrm{Z}}| \approx |\vec{E}_{\mathrm{T}}^{\mathrm{miss}} - \vec{p}_{\mathrm{T}}^{\,\mathrm{Z}}| - |\vec{p}_{\mathrm{T}}^{\,\mathrm{Z}}|. \tag{5.11}$$

For SM processes such as $Z+\mathrm{jets}$, where $E_{\mathrm{T}}^{\mathrm{miss}}$ is caused by mismeasurements of the jets, the JZB distribution is symmetric around 0. For BSM processes, where the Z boson is produced correlated with invisible particles, the JZB distribution is expected to be asymmetric, favouring positive sign especially for large values of JZB and by extension high $E_{\mathrm{T}}^{\mathrm{miss}}$. Therefore it is possible to predict the contribution of SM processes containing a Z boson at high $E_{\mathrm{T}}^{\mathrm{miss}}$ from the events in that region with negative values of JZB, after subtraction of flavour-symmetric processes from OF events. The assumption that the JZB distribution is symmetric around 0 for SM processes with only instrumental $E_{\mathrm{T}}^{\mathrm{miss}}$ is studied in MC and 20% systematic uncertainty are assigned.**FIXME:** Add reference to 2012 paper.

5.2.2. $E_{\mathrm{T}}^{\mathrm{miss}}$ templates method

The $E_{\mathrm{T}}^{\mathrm{miss}}$ templates method utilizes the similarity of $Z+\mathrm{jets}$ and $\gamma+\mathrm{jets}$ events, especially mismeasurement as only source of $E_{\mathrm{T}}^{\mathrm{miss}}$. Therefore, after corrections for residual kinematic differences, the contribution of $Z+\mathrm{jets}$ events at high $E_{\mathrm{T}}^{\mathrm{miss}}$ can be estimated from $\gamma+\mathrm{jets}$ events passing the same selection. The dominant systematic uncertainties are assigned based on tests of the method on simulation and are in the order of 15-100% for $E_{\mathrm{T}}^{\mathrm{miss}}$ values falling into the signal selection of this analysis. The large uncertainties for higher $E_{\mathrm{T}}^{\mathrm{miss}}$ values are driven the available MC statistics to validate the method.

In contrast to the JZB method, the $E_{\mathrm{T}}^{\mathrm{miss}}$ templates method does account only for $Z+\mathrm{jets}$ events. Other backgrounds containing Z bosons, such as WZ, ZZ or more rare SM processes like $t\bar{t}Z$ or Triboson production are estimated from simulation and assigned 50% uncertainty.

5.2.3. Extrapolation for off-Z regions

Both methods described above result in background estimates for the on-Z region of 81 GeV $< m_{\ell\ell} <$ 101 GeV. Contributions to the low-Mass and high-Mass selections from off-Shell Z bosons or the Drell–Yan continuum are estimated by applying an extrapolation factor $R_{\mathrm{out/in}}$ to the on-Z prediction. $R_{\mathrm{out/in}}$ is measured in the Drell–Yan control region, separately for the low-Mass and high-Mass region as well as $e^{\pm}e^{\mp}$, $\mu^{\pm}\mu^{\mp}$ and SF leptons. It is defined as the ratio of the event yield in the mass region in question (*out*) by that in the on-Z mass region (*in*), after subtraction of contribution from flavour-symmetric processes from the OF sample:

$$R_{\text{out/in}} = \frac{\mathrm{N}^{\mathrm{SF}}_{\mathrm{out}} - \mathrm{N}^{\mathrm{OF}}_{\mathrm{out}} R_{\text{SF/OF}}}{\mathrm{N}^{\mathrm{SF}}_{\mathrm{in}} - \mathrm{N}^{\mathrm{OF}}_{\mathrm{in}} R_{\text{SF/OF}}}, \tag{5.12}$$

where the SF is substituted for $e^{\pm}e^{\mp}$ or $\mu^{\pm}\mu^{\mp}$ according to the desired lepton flavour. The $m_{\ell\ell}$ distribution in the Drell–Yan control region is shown in Figure 5.12. The resulting values range from about 6-8% for the low-Mass region to 2-3% for the high-Mass region, as summarized in Table 5.10.

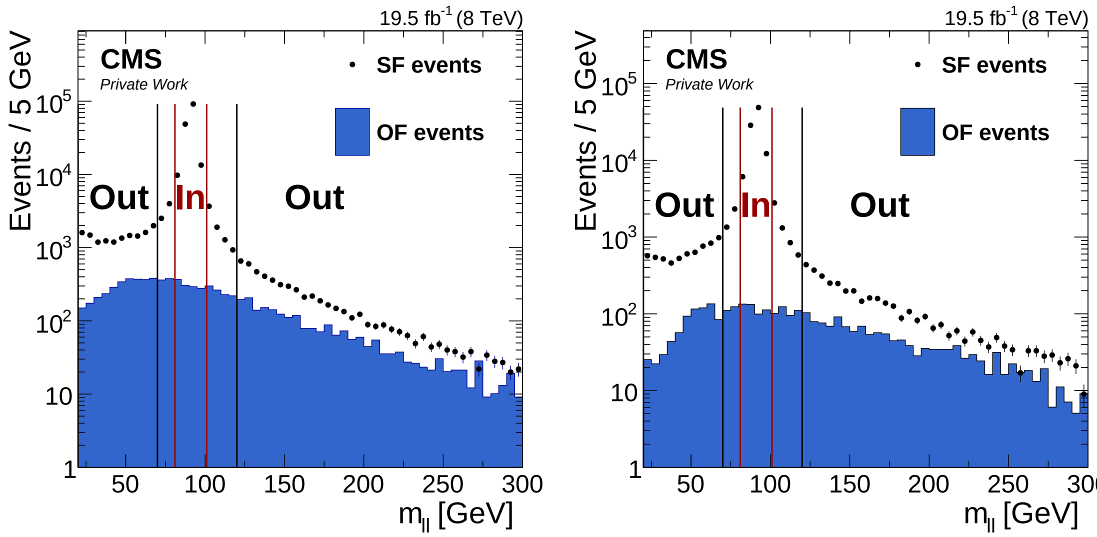

Figure 5.12.: The $m_{\ell\ell}$ distribution in the Drell–Yan control region in the central (left) and forward (right) dielepton selection. SF data is shown as the black points while OF data is shown as the blue histogram. The black lines indicate the boundaries of the two *out* regions and the dark red lines those of the *in* region.

The validity of applying the $R_{\text{out/in}}$ as measured in the Drell–Yan control region in the signal region is checked by studying the behaviour of the quantity as a function of $E_{\mathrm{T}}^{\mathrm{miss}}$ and N_{Jets}. The results for the low-Mass selection and the case of SF leptons is shown in Figure 5.13 for both the central and forward lepton selections. In neither selection a clear dependency on $E_{\mathrm{T}}^{\mathrm{miss}}$ is observed. However, above 70 GeV there is not enough statistics left after subtraction of the flavour-symmetric backgrounds, so it is not possible to judge the behaviour all the way up to the signal region. The value of $R_{\text{out/in}}$ clearly increases with the number of jets. As the requirement on $N_{\text{Jets}}$is the same between the Drell–Yan control region and the signal region, the events do not differ much in terms of jet multiplicity and this dependency does not significantly restrict the applicability of the $R_{\text{out/in}}$ factors in the signal region. In total, an systematic uncertainty of 25% is assigned to cover the observed effects. Consistent results are observed also for the high-Mass region and for the split into $e^{\pm}e^{\mp}$ and $\mu^{\pm}\mu^{\mp}$, as can be seen in Appendix **FIXME:** Make routin appendix and refer to it.

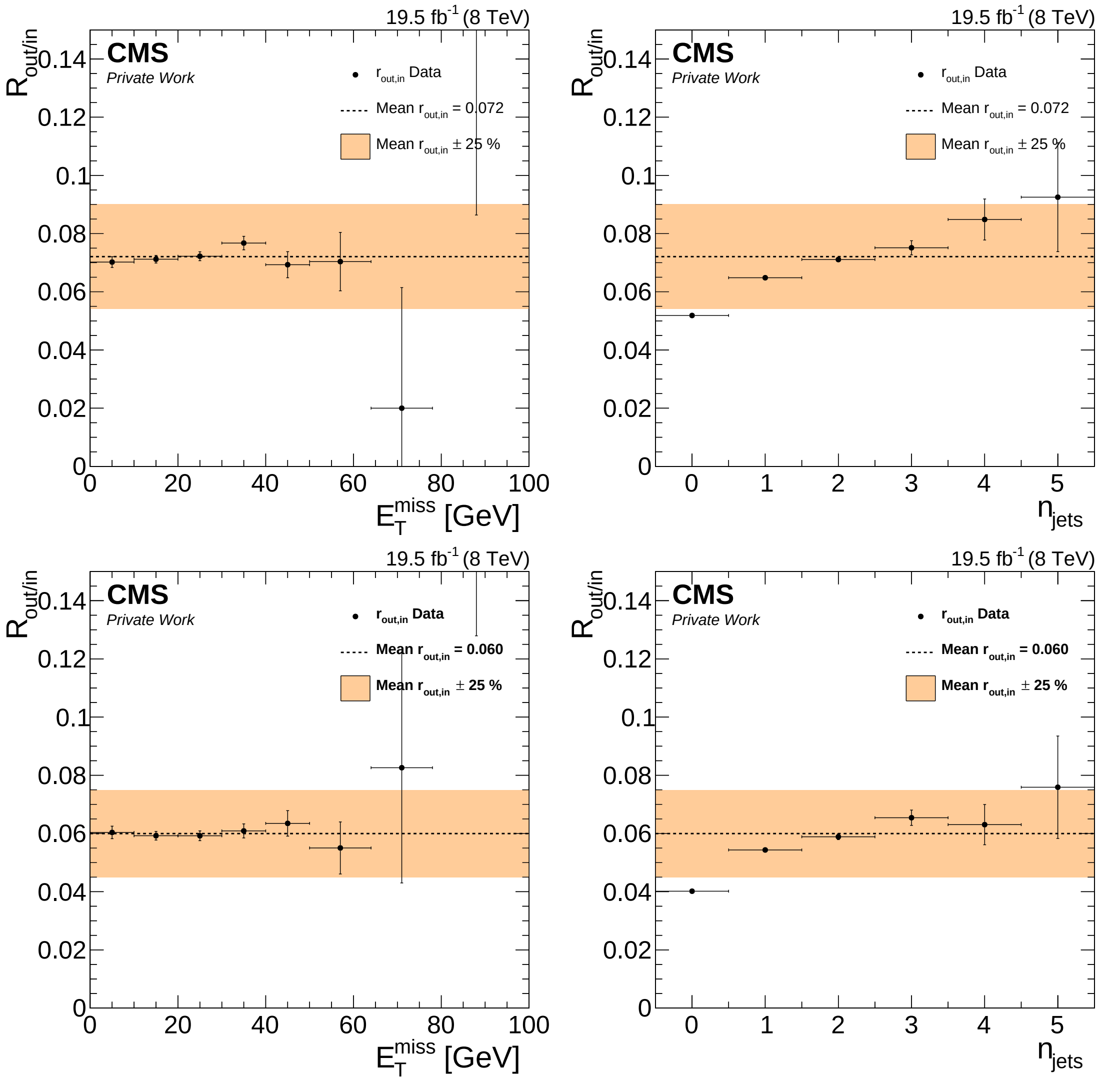

Figure 5.13.: Dependencies of $R_{\text{out/in}}$ on $E_{\mathrm{T}}^{\text{miss}}$ (left) and N_{jets} (right) for the central (top) and forward (bottom) lepton selection. The results on data are shown in black. The central value is shown as a black dashed line while the systematic uncertainty is shown as an orange band.

Table 5.10.

	N_{out}	N_{in}	$R_{\mathrm{out/in}}(SF) \pm \sigma_{stat}$
	Central		
	Low mass		
Data	11608.6±131.7	160645.8±403.9	0.072±0.001±0.018
MC	10725.8±128.7	167291.6±412.0	0.064±0.001±0.016
	high Mass		
Data	3571.3±91.2	160645.8±403.9	0.022±0.001±0.006
MC	3243.0±88.9	167291.6±412.0	0.019±0.001±0.005
	Forward		
	Low mass		
Data	5657.6±84.2	94407.6±308.7	0.060±0.001±0.015
MC	5695.8±85.5	103407.4±323.0	0.055±0.001±0.014
	high Mass		
Data	2672.5±75.8	94407.6±308.7	0.028±0.001±0.007
MC	2459.1±72.3	103407.4±323.0	0.024±0.001±0.006

5.2.4. Resulting background prediction

The predictions for the on-Z region from the JZB and $E_{\mathrm{T}}^{\mathrm{miss}}$ templates methods agree within their uncertainties. As for the $R_{\mathrm{SF/OF}}$ factor, a weighted average is used to combine the two estimates. The results of both methods as well as the combination are shown in Table 5.11. Shown there are also the $R_{\mathrm{out/in}}$ values and the resulting estimates for the low- and high-Mass regions. For this, the on-Z predictions, which are derived on the PromptReco, are scaled by 1.03±0.03 to take into account the slight increase in jet multiplicity in the ReReco dataset.

Table 5.11.: Estimate of the Z background yields in the Z peak region and extrapolation to the signal mass region for the full dataset.

	central		
	$e^{\pm}e^{\mp}$	$\mu^{\pm}\mu^{\mp}$	SF
Z bkgd estimate (JZB)	$57.9 \pm 13.8 \pm 10.1$	$46.1 \pm 13.8 \pm 8.0$	$104 \pm 21 \pm 18$
Z bkgd estimate ($E_{\mathrm{T}}^{\mathrm{miss}}$ templates)	$63.2 \pm 4.3 \pm 15.3$	$69.5 \pm 4.0 \pm 16.9$	$133 \pm 7 \pm 32$
Z bkgd estimate (Combined)	60.7 ± 11.6	56.8 ± 11.7	116 ± 21
$R_{\mathrm{out/in}}$ low-Mass	0.069±0.001±0.017	0.075±0.001±0.019	0.072±0.001±0.018
low-Mass estimate	4.3±1.3	4.4±1.4	8.6±2.7
$R_{\mathrm{out/in}}$ high-Mass	0.025±0.001±0.006	0.020±0.001±0.005	0.022±0.001±0.006
high-Mass estimate	1.5±0.5	1.2±0.4	2.7±0.8
	forward		
	$e^{\pm}e^{\mp}$	$\mu^{\pm}\mu^{\mp}$	SF
Z bkgd estimate (JZB)	$15.6 \pm 8.3 \pm 2.9$	$13.8 \pm 8.3 \pm 2.8$	$29 \pm 11 \pm 6$
Z bkgd estimate (MET templates)	$24.4 \pm 1.8 \pm 6.0$	$32.3 \pm 2.2 \pm 7.9$	$56.9 \pm 3.6 \pm 14.0$
Z bkgd estimate (Combined)	21 ± 5	25 ± 6	42 ± 9
$R_{\mathrm{out/in}}$ low-Mass	0.055±0.001±0.014	0.064±0.001±0.016	0.060±0.001±0.015
low-Mass estimate	1.2±0.4	1.6±0.6	2.6±0.8
$R_{\mathrm{out/in}}$ high-Mass	0.031±0.001±0.008	0.026±0.001±0.007	0.028±0.001±0.007
high-Mass estimate	0.7±0.2	0.7±0.2	1.2±0.4

6. Results of the counting experiment

6.1. Results and further studies

The distribution of the dilepton invariant mass in the central and forward signal regions are shown in Figure 6.1. The resulting event yields are compared to the expectation from SM backgrounds in Table 6.2. A maximum likelihood fit is performed in each region to find the best estimator for the for the difference of expected and observed yield. The significances of deviations of this difference from zero are evaluated using the profile likelihood ratio of the signal and signal+background hypothesis [69]. In general, the observed data is in agreement with the background estimation within about one standard deviation, except for the low-mass region in the central dilepton selection. Here the observed yield exceeds the expectation by 109^{+48}_{-49} events. The size of this excess corresponds to a significance of 2.2 σ.

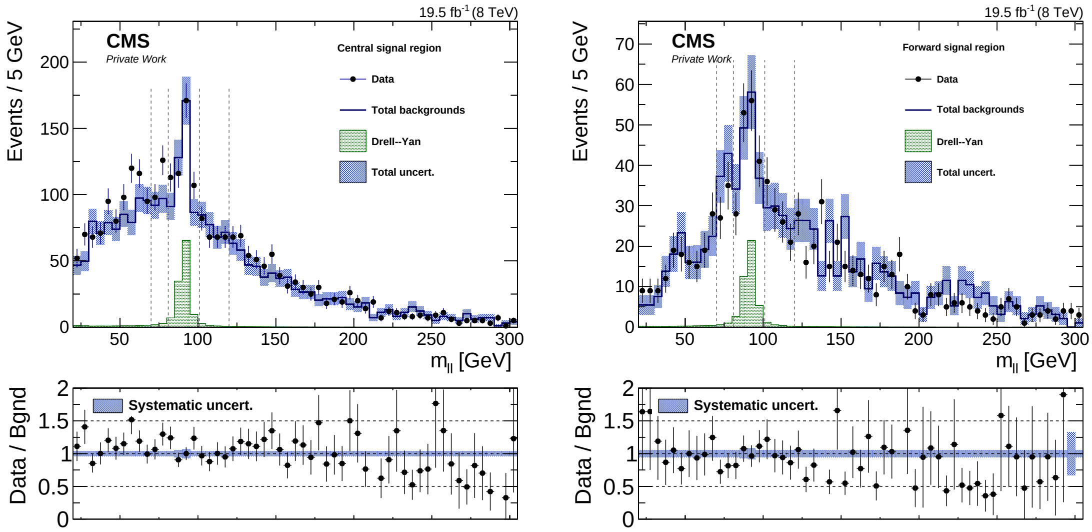

Figure 6.1.: Distribution of $m_{\ell\ell}$ in the signal region for the central (left) and forward (right) dilepton selection. The data is shown as black dots, while the total background prediction from data is shown as a blue histogram. The blue error bars indicate the combined statistical and systematic background uncertainty in each bin. The contribution from backgrounds containing a Z boson is shown as a green histogram. The dashed lines indicates the boundaries of the three mass bins. Beneath the plot the ratio of data to the background prediction is shown. The error bars include the statistical uncertainties of data and background, while the blue band indicates the systematic uncertainties on the background.

In the Tables 6.3 and **??**, the results are shown separately for $e^{\pm}e^{\mp}$ and $\mu^{\pm}\mu^{\mp}$ events. As expected from the fact that $r_{\mu e}$ is larger than one, the yields in the $\mu^{\pm}\mu^{\mp}$ channel are slightly larger than in the $e^{\pm}e^{\mp}$ channel. For the flavour-symmetry backgrounds, and therefore also

Table 6.1.: Results of the edge-search counting experiment for event yields in the signal regions. The statistical and systematic uncertainties are added in quadrature, except for the flavor-symmetric backgrounds. Low-mass refers to $20 < m_{\ell\ell} < 70$ GeV, on-Z to $81 < m_{\ell\ell} < 101$ GeV and high-mass to $m_{\ell\ell} > 120$ GeV.

	Low-mass		On-Z		High-mass	
	Central	Forward	Central	Forward	Central	Forward
Observed	865	154	494	176	849	381
Flavor-symmetric	$746 \pm 27 \pm 26$	$144 \pm 12 \pm 7$	$368 \pm 19 \pm 13$	$137 \pm 11 \pm 7$	$789 \pm 28 \pm 28$	$411 \pm 20 \pm 21$
Drell–Yan	8.6 ± 2.7	2.6 ± 0.8	119 ± 21	43 ± 9	2.7 ± 0.8	1.2 ± 0.4
Total estimated	755 ± 38	147 ± 14	488 ± 31	180 ± 16	792 ± 39	413 ± 30
Observed - estimated	109^{+48}_{-48}	7^{+19}_{-19}	6^{+37}_{-38}	-5^{+21}_{-21}	57^{+49}_{-50}	-32^{+35}_{-37}
Significance	2.2 σ	0.4 σ	0.1 σ	<0.1 σ	1.1 σ	<0.1 σ

for the total background estimates and the difference of observation and estimation, the yields in the $e^{\pm}e^{\mp}$ and $\mu^{\pm}\mu^{\mp}$ channels to not exactly add up to those in the combined SF channel. **FIXME:** Reference explenation once written

Table 6.2.: Results of the edge-search counting experiment for event yields in the signal regions. The statistical and systematic uncertainties are added in quadrature, except for the flavor-symmetric backgrounds. Low-mass refers to $20 < m_{\ell\ell} < 70$ GeV, on-Z to $81 < m_{\ell\ell} < 101$ GeV and high-mass to $m_{\ell\ell} > 120$ GeV.

	Low-mass		On-Z		High-mass	
	Central	Forward	Central	Forward	Central	Forward
Observed	389	53	232	86	401	195
Flavor-symmetric	$337 \pm 12 \pm 19$	$61 \pm 5 \pm 6$	$166 \pm 8 \pm 9$	$58 \pm 5 \pm 5$	$357 \pm 12 \pm 21$	$175 \pm 8 \pm 17$
Drell–Yan	4.3 ± 1.3	1.2 ± 0.4	62 ± 11	21 ± 5	1.5 ± 0.5	0.7 ± 0.2
Total estimated	342 ± 23	62 ± 8	229 ± 17	79 ± 9	358 ± 24	175 ± 19
Observed - estimated	47^{+25}_{-25}	-10^{+9}_{-9}	3^{+21}_{-21}	6^{+12}_{-12}	42^{+25}_{-26}	19^{+18}_{-18}
Significance	1.9 σ	<0.1 σ	0.1 σ	0.5 σ	1.7 σ	1.1 σ

6.2. Interpretation in simplified models

The absence of a clear indication for the existence of SUSY in the results of the counting experiment presented in section 6.1 constrains the validity of supersymmetric models. To quantify the impact these results have on the allowed parameter space, they are interpreted in specific signal scenarios. For this two "simplified models" are used that have been developed for this purpose by Christian Schomakers in the context of his master thesis [70]. In this kind of models, only the subset of sparticles relevant to the studied signature is assumed to be accessible at LHC energies. Also, the branching fractions of the sparticle decays are chosen to produce the desired signature and are often set to 100%. As the interpretation presented here closely follows the procedures developed to obtain the existing results, only a short description is given.

Table 6.3.: Results of the edge-search counting experiment for event yields in the signal regions. The statistical and systematic uncertainties are added in quadrature, except for the flavor-symmetric backgrounds. Low-mass refers to $20 < m_{\ell\ell} < 70$ GeV, on-Z to $81 < m_{\ell\ell} < 101$ GeV and high-mass to $m_{\ell\ell} > 120$ GeV.

	Low-mass		On-Z		High-mass	
	Central	Forward	Central	Forward	Central	Forward
Observed	476	101	262	90	448	186
Flavor-symmetric	$405 \pm 14 \pm 21$	$79 \pm 6 \pm 6$	$200 \pm 10 \pm 10$	$74 \pm 6 \pm 6$	$428 \pm 15 \pm 23$	$224 \pm 11 \pm 19$
Drell–Yan	4.4 ± 1.4	1.6 ± 0.6	58 ± 10	25 ± 6	1.2 ± 0.4	0.7 ± 0.2
Total estimated	409 ± 26	80 ± 9	258 ± 18	100 ± 11	429 ± 27	225 ± 22
Observed - estimated	67^{+29}_{-29}	20^{+13}_{-13}	3^{+22}_{-23}	-11^{+13}_{-13}	19^{+29}_{-29}	-40^{+21}_{-21}
Significance	2.3 σ	1.6 σ	0.2 σ	<0.1 σ	0.6 σ	<0.1 σ

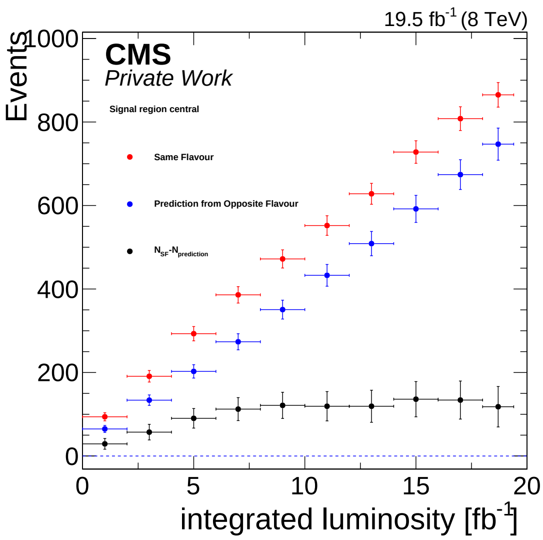

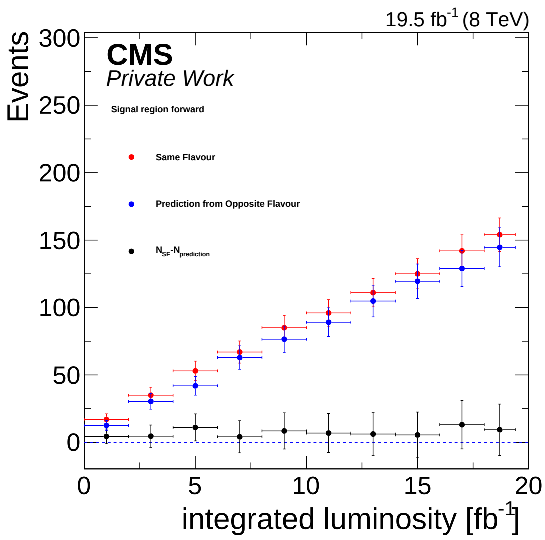

Figure 6.2.: Distribution of $m_{\ell\ell}$ in the signal region for the central (left) and forward (right) dilepton selection. The data is shown as black dots, while the total background prediction from data is shown as a blue histogram. The blue error bars indicate the combined statistical and systematic background uncertainty in each bin. The contribution from backgrounds containing a Z boson is shown as a green histogram. The dashed lines indicates the boundaries of the three mass bins. Beneath the plot the ratio of data to the background prediction is shown. The error bars include the statistical uncertainties of data and background, while the blue band indicates the systematic uncertainties on the background.

Table 6.4.: Results of the counting experiment in the low-mass central signal region for different variations of the event selection. The observed event yield in SF events is compared with the combined estimate from flavour-symmetric and Drell–Yan backgrounds. The estimate for the Drell–Yan backgrounds is obtained by extrapolating the event yield in the on-Z signal region after subtraction of flavour-symmetric backgrounds to the low-mass region using the $R_{\text{out/in}}$ factor.

	SF	Flavour-symmetric	Drell–Yan	Observed - Estimates
		b tagging		
no b-tags	202	188.5±15.4	7.1±2.5	6.3±21.1
≥ 1 b-tags	663	558.4±31.0	1.9±0.7	102.7±40.3
		lepton p_{T} requirement		
$p_{\mathrm{T}} > 20(10)$ GeV	1474	1290.2±58.6	11.4±4.1	172.5±70.1
$p_{\mathrm{T}} > 30(10)$ GeV	1262	1114.8±52.1	11.3±4.1	135.9±63.2
$p_{\mathrm{T}} > 30(20)$ GeV	761	674.0±35.5	9.0±3.3	78.0±45.1
$p_{\mathrm{T}} > 30$ GeV	296	275.7±19.4	6.5±2.3	13.8±26.0
		tight lepton isolation		
rel. isolation < 0.05	572	491.5±28.4	7.1±2.6	73.3±37.2
		pileup		
$N_{\text{vtx}} < 13$	332	289.9±20.0	3.3±1.2	38.8±27.1
$13 \leq N_{\text{vtx}} < 17$	242	212.8±16.5	0.9±0.3	28.3±22.7
$N_{\text{vtx}} \geq 17$	291	244.2±18.0	4.8±1.7	41.9±24.8
		$E_{\mathrm{T}}^{\mathrm{miss}}$ reconstructions		
Calo $E_{\mathrm{T}}^{\mathrm{miss}}$	850	702.3±36.6	26.3±9.4	121.3±47.7
type I corrected PF $E_{\mathrm{T}}^{\mathrm{miss}}$	1034	923.3±45.0	9.4±3.4	101.3±55.4
track corrected $E_{\mathrm{T}}^{\mathrm{miss}}$	850	702.3±36.6	26.3±9.4	121.3±47.7
missing H_{T}	1171	942.5±45.7	50.8±18.1	177.6±59.9
		H_{T}		
100 GeV $< H_{\mathrm{T}} <$ 300 GeV	455	401.3±24.7	1.4±0.5	52.3±32.7
$H_{\mathrm{T}} >$ 300 GeV	410	344.6±22.4	7.5±2.7	57.9±30.3

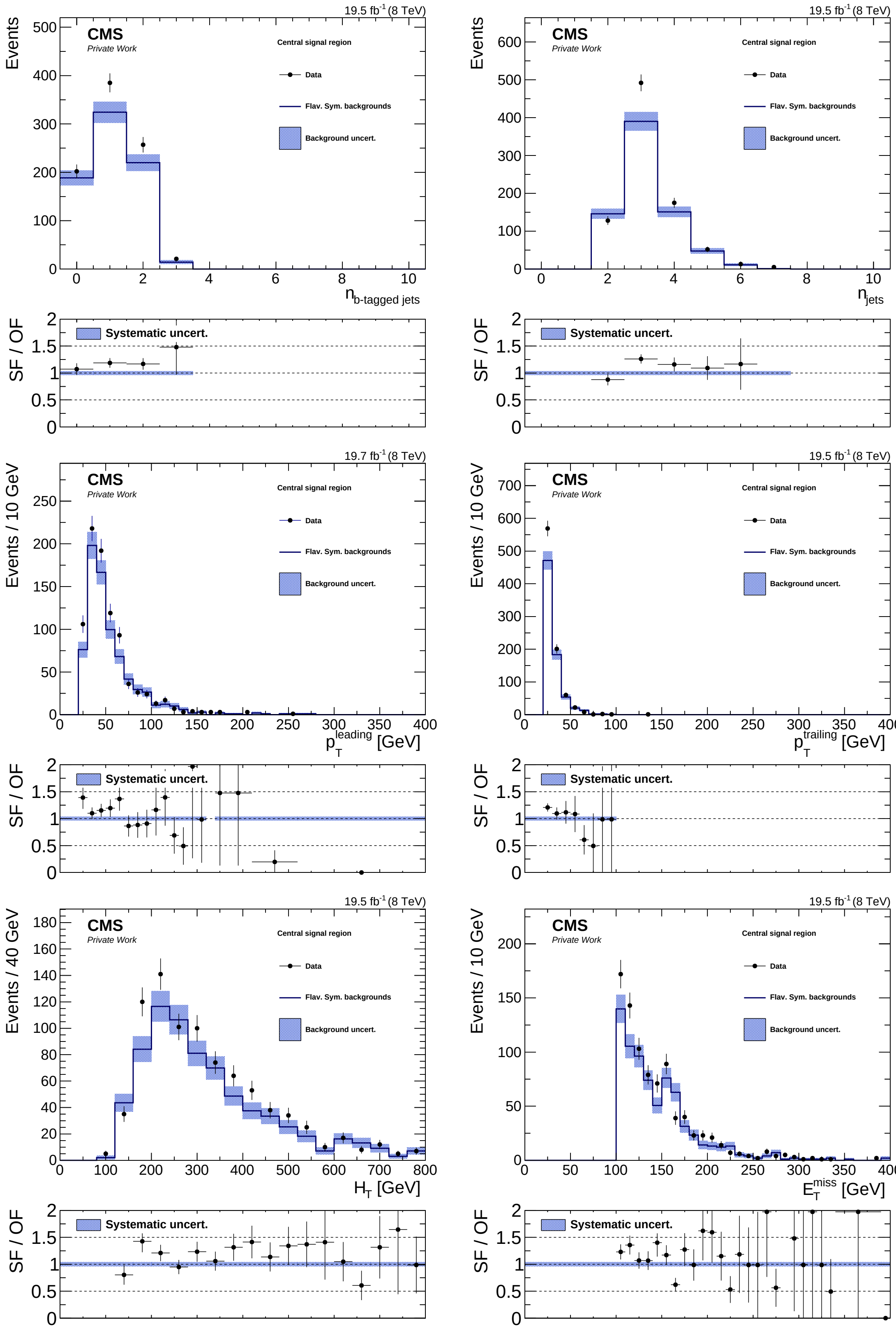

Figure 6.3.: Distribution of $m_{\ell\ell}$ in the signal region for the central (left) and forward (right) dilepton selection. The data is shown as black dots, while the total background prediction from data is shown as a blue histogram. The blue error bars indicate the combined statistical and systematic background uncertainty in each bin. The contribution from backgrounds containing a Z boson is shown as a green histogram. The dashed lines indicates the boundaries of the three mass bins. Beneath the plot the ratio of data to the background prediction is shown. The error bars include the statistical uncertainties of data and background, while the blue band indicates the systematic uncertainties on the background.

6.2.1. "Fixed-edge" and "slepton-edge" models

In the design of the simplified models, the properties of the excess observed a low invariant masses are used as the guiding principle. As the excess is observed at relatively low values of H_{T}, the mass of the initially produced sparticles also has to be rather small. Pair production of third generation squarks allows to evade the existing limits on the masses of the gluino and first and second generation squarks. This choice is further motivated by the presence of at least one b-tagged jets in the events of the excess. Bottom squarks are chosen to avoid the larger multiplicity of final state particles associated with the production of top quarks in the decays of stop quarks.

The bottom squarks decay into a bottom quark and a $\tilde{\chi}_2^0$ with a branching fraction of 100%. The decays of the $\tilde{\chi}_2^0$ differ between the two models. In the "fixed-edge" model, it decays into an off-shell Z boson and a $\tilde{\chi}_1^0$ in 100% of the cases. The Z boson decays with its SM branching ratios, producing light leptons in about 7% of the cases. The $m_{\tilde{b}}$-$m_{\tilde{\chi}_2^0}$-plane is scanned, varying the masses of the two particles in steps of 25 GeV. The mass of the $\tilde{\chi}_1^0$ is fixed to be 70 GeV below that of the $\tilde{\chi}_2^0$ to produce an edge in the $m_{\ell\ell}$ spectrum at this value. Therefore this model is specifically suited to study the excess observed in the low-mass region.

As a mass difference between the two neutralinos larger than the Z boson mass would only result in the production of on-shell Z bosons in this model, the "slepton-edge" model introduces selectrons and smuons as additional new particles. The mass of these sleptons is assumed to be degenerate and set to lie halfway between the two neutralinos: $m_{\tilde{l}} = m_{\tilde{\chi}_1^0} + 0.5(m_{\tilde{\chi}_2^0} - m_{\tilde{\chi}_1^0})$. The branching fractions of the $\tilde{\chi}_2^0$ are chosen such that the decay in an off- or on-shell Z boson or a slepton and a lepton occur with 50% probability each. The Z boson again decays according to its SM branching fraction while the slepton always decays into a lepton and the $\tilde{\chi}_1^0$. Again the $m_{\tilde{b}}$-$m_{\tilde{\chi}_2^0}$-plane is scanned in steps of 25 GeV, while the $m_{\tilde{\chi}_1^0}$ is set to be 100 GeV, allowing for edges in the $m_{\ell\ell}$ spectrum also above the Z boson mass. The signal simulation is normalized to theory cross sections calculated at NLO in α_s, including the leading logarithmic contributions of the next higher order [71, 72, 73, 74, 75, 76].

Selection efficiencies

The impact of branching fractions, detector acceptance, and selection efficiencies on the different signal points is shown in Figure 6.4 for the example of the central signal region for the fixed-edge (left) and slepton-edge (right) models. Because of the much larger branching fraction into lepton pairs in the case of the slepton-edge model, the overall acceptance$\times$efficiency is an order of magnitude larger in this case. As the event kinematics vary strongly depending on the sparticle masses, the efficiency strongly depends on the position of the signal point in the $m_{\tilde{b}}$-$m_{\tilde{\chi}_2^0}$ plane. In general, the efficiency is low along the diagonal, where little energy is available for the decay products. Another notable feature is a decrease in efficiency around $\tilde{\chi}_2^0$ masses of about $225\,\mathrm{GeV}$ in the case of the slepton-edge model. This is caused by the gaps in the signal acceptance between the three invariant mass regions of the counting experiment. No such effect is visible for the fixed-edge case because the signal is concentrated in the low-mass region in this model.

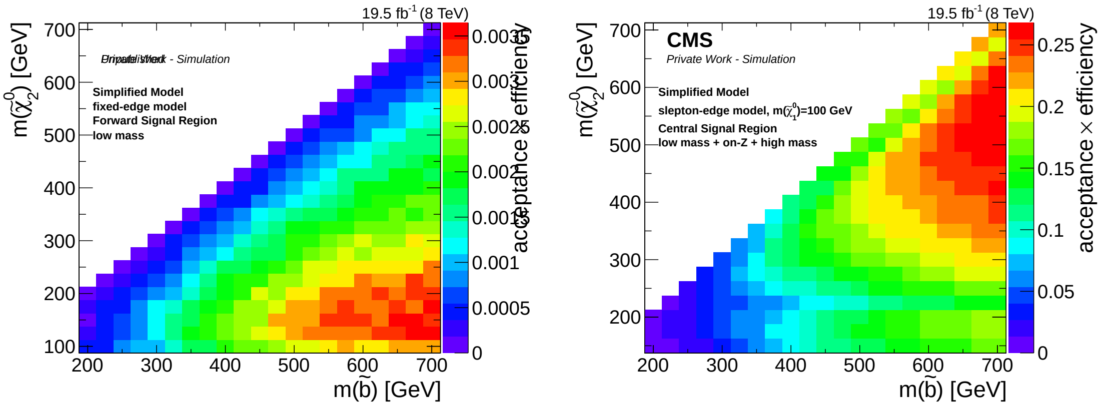

Figure 6.4.: Signal acceptance×efficiency in the $m_{\tilde{b}}$-$m_{\tilde{\chi}_2^0}$ plane for the fixed-edge (left) and slepton-edge (right) model for the central signal region.

Systematic uncertainties

A variety of systematic uncertainties in the signal modelling have to taken into account. The integrated luminosity is measured with a precision of 2.6% [77]. Variations of the parton distribution functions (PDF) according to the PDF4LHC recommendations [78, 79, 42, 43, 44] result in an uncertainty of 0–6% in the signal acceptance. Uncertainties related to lepton efficiencies are of the size of 1% per lepton. Furthermore, the corrections of the lepton efficiency differences between fast and full detector simulation amount to another 1% per lepton. The dilepton trigger efficiencies are measured with a precision of 5%, as described in section 5.1.2. Uncertainties on the muon momentum scale have negligible impact on the signal acceptance, whereas the uncertainty in the electron energy scale is 0.6% for central and 1.5% for forward leptons. Jet energy scale uncertainties [25] result in an uncertainty in the signal yield of 0–8%. The uncertainties in the modeling of the objects in the events are propagated to the $E_{\mathrm{T}}^{\mathrm{miss}}$ measurements, resulting in and uncertainty in the signal acceptance of 0–8%. Here the contributions from the jet energy scale uncertainties are dominant. Uncertainties in the modeling of initial-state radiation (ISR) [80] are propagated to the event selection and result in an uncertainty of 0–14% in the signal yield. The uncertainty associated with pileup reweighting is evaluated by shifting the inelastic cross section by $\pm 5\%$, resulting in an uncertainty on the signal acceptance of about 1%. The uncertainties are summarized in Table 6.5.

The combined systematic uncertainties are shown in Figure 6.5. For the most part of the $m_{\tilde{b}}$-$m_{\tilde{\chi}_2^0}$ plane it ranges from 5-7%. However, close to the diagonal this increases, caused by a larger impact of JES and ISR uncertainties. This is due to the overall lower jet p_{T} in this region, increasing the probability for threshold effects around the jet p_{T} requirement of $40\,\mathrm{GeV}$. The largest uncertainties are observed for both low masses of the $\tilde{b}$ and $\tilde{\chi}_2^0$, exceeding 20% for the fixed-edge model and reaching 15% for the slepton-edge model.

Table 6.5.: Summary of systematic uncertainties for the signal efficiency.

Uncertainty source	Impact on signal yield [%]
Luminosity	2.6
PDFs on acceptance	0–6
Lepton identification/isolation	2
Fast simulation lepton identification/isolation	2
Dilepton trigger	5
Lepton energy scale	0–5
$E_{\mathrm{T}}^{\mathrm{miss}}$	0–8
Jet energy scale/resolution	0–8
ISR modeling	0–14
Additional interactions	1

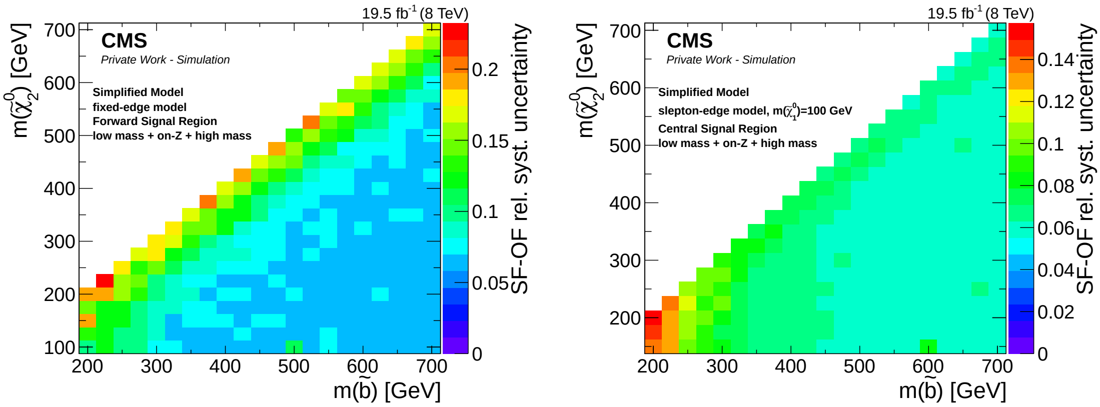

Figure 6.5.: Systematic uncertainty on the signal yield in the central signal region in the $m_{\tilde{b}}$-$m_{\tilde{\chi}_2^0}$ plane for the fixed-edge (left) and slepton-edge (right) model.

6.2.2. Statistical interpretation

The results of the counting experiment are translated into exclusion limits by testing the compatibility of the signal plus background $(s+b)$ and background only (b) hypothesis, treating each signal point in the parameter scans as a separate signal hypothesis. For this purpose, a likelihood function is defined [69]

$$\mathcal{L}(data|\mu,\theta) = \text{Poisson}(data|\mu \cdot s(\theta) + b(\theta)) \cdot p(\tilde{\theta}|\theta), \tag{6.1}$$

where μ is a signal strength parameter, $\mu = 0$ corresponding to the background only hypothesis and $\mu > 0$ to the $s + b$ hypothesis, and $p(\tilde{\theta}|\theta)$ parametrizes the nuisance parameters θ, with $\tilde{\theta}$ being the nominal value of these parameters. Based on these likelihoods, a test statistic is defined utilizing a profile likelihood ratio:

$$\tilde{q_\mu} = -2ln\frac{\mathcal{L}(data|\mu,\hat{\theta}_\mu)}{\mathcal{L}(data|\hat{\mu},\hat{\theta})}, \tag{6.2}$$

where the $\hat{\theta}_\mu$ represent the maximum likelihood estimators for the nuisance parameters for a given μ, whereas $\hat{\mu}$ and $\hat{\theta}$ indicate the global maximum of the likelihood. The likelihoods themselves consist of a poisson distribution multiplied by some parametrization of the nuisance parameters. The distribution of the test statistics is then sampled dicing pseudo-experiments for some $\mu > 0$ and $\mu = 0$, representing the $s + b$ and b hypotheses that are tested. The p-values p_{s+b} and p_b are defined as the probability to obtain a value of the test statistics as large or larger than the one observed in data for the given hypothesis. To obtain an upper limit on the signal cross section the value of μ is chosen where $\mathrm{CL_s} = \frac{p_{s+b}}{p_b}$ equals 0.05, corresponding to a 95% confidence level (CL). In the calculation, all six bins of the counting experiment are combined. Nuisance parameters are modelled with log-normal distributions and all uncertainties are assumed to be uncorrelated among each other but fully correlated among the different bins.

The resulting exclusion limits are shown in Figure 6.6. The left plot shows the exclusion limit in the $m_{\tilde{b}}$-$m_{\tilde{\chi}_2^0}$ plane for the fixed-edge model. As this model is specifically tuned to provide signals consistent with the excess observed in the low-mass central signal region, the observed limits deviates from the expected one by about $75\,\mathrm{GeV}$. Given the assumption of this model, $\tilde{b}$ masses up to about $375\,\mathrm{GeV}$ are excluded, depending on the mass of the $\tilde{\chi}_2^0$.

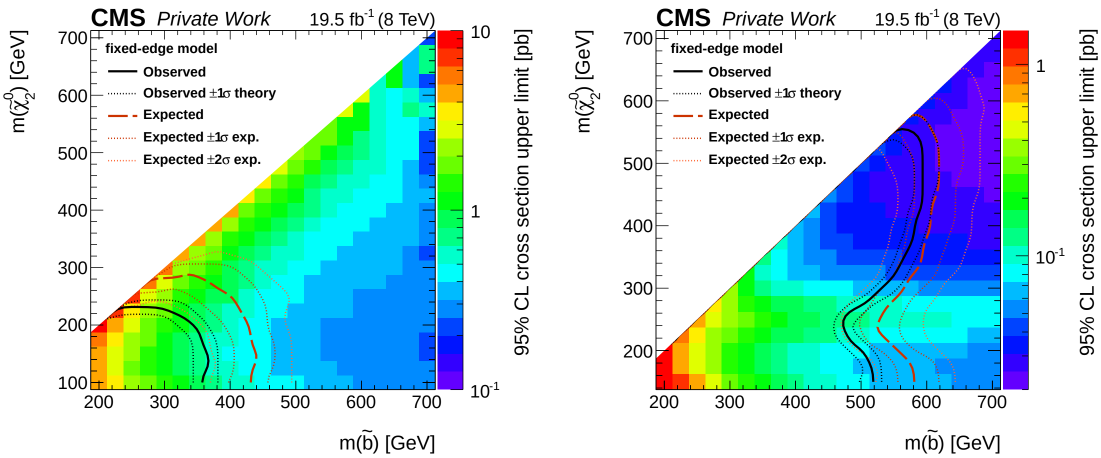

Figure 6.6.: Exclusion limits in the $m_{\tilde{b}}$-$m_{\tilde{\chi}_2^0}$ plane for the fixed-edge (left) and slepton-edge (right) model. For each signal point the upper cross section limit is shown colour coded. The intersection of the theoretical with the excluded cross section is shown as a solid black line, with every signal point to the left and below the curve being excluded. The $1-\sigma$ uncertainty interval on the observed limit is shown as dotted black lines. The expected limit together with the $1-$ and $2-\sigma$ interval are shown as brownish solid and dashed lines.

7. Search for an kinematic edge

A fit to the $m_{\ell\ell}$ distribution is performed in search of the characteristic edge signature described in section **??**. Different functions are used to model the contributions of the potential signal, flavour-symmetric backgrounds, and backgrounds containing a Z boson. To fully exploit the available information, an unbinned maximum-likelihood fit is performed simultaneously to the $e^{\pm}e^{\mp}$, $\mu^{\pm}\mu^{\mp}$, and $e^{\pm}\mu^{\mp}$ event samples for both the signal and forward dilepton selection in the signal region.

7.1. Background and signal models

7.1.1. Model for Z backgrounds

The background model for events containing a Z boson contains of two components: one model for the Z boson peak and one for the contribution of the Drell–Yan continuum. The latter one is a simple falling exponential. The peak model consists of a Breit-Wigner function with mean and widths fixed to the DPG values for the Z boson, convolved with a double-sided crystal ball function [81]. The first component models the physical peak while the latter accounts for the detector resolution and radiative corrections to the Z lineshape. The double-sided crystal ball itself consists of a Gaussian core and exponential falloffs to both sides of the peak, parametrized as

$$\mathcal{P}_{DSCB}(m_{\ell\ell}) = \begin{cases} A_1(B_1 - \frac{m_{ll}-\mu_{CB}}{\sigma_{CB}})^{-n_1} & \text{if } \frac{m_{ll}-\mu_{CB}}{\sigma_{CB}} < -\alpha_1 \\ \exp\left(-\frac{(m_{ll}-\mu_{CB})^2}{2\sigma_{CB}^2}\right) & \text{if } -\alpha_1 < \frac{m_{ll}-\mu_{CB}}{\sigma_{CB}} < \alpha_2 \\ A_2(B_2 + \frac{m_{ll}-\mu_{CB}}{\sigma_{CB}})^{-n_2} & \text{if } \frac{m_{ll}-\mu_{CB}}{\sigma_{CB}} > \alpha_2 \end{cases}$$

where σ_{CB} and μ_{CB} are the parameters of the central Gaussian and the n_i and α_i govern the transition to and the shape of the exponential falloff. The A_i and B_i are substitutions for

$$A_i = \left(\frac{n_i}{|\alpha_i|}\right)^{n_i} \cdot \exp\left(-\frac{|\alpha_i|^2}{2}\right) \quad \text{and} \quad B_i = \frac{n_i}{|\alpha_i|} - |\alpha_i|.$$

Taking into account also the exponential function described the Drell–Yan continuum, the full description is therefore

$$\mathcal{P}_{DY}(m_{\ell\ell}) = (1 - f_{exp})\mathcal{P}_{exp}(m_{\ell\ell}) + f_{exp}\int \mathcal{P}_{DSCB}(m_{\ell\ell})\mathcal{P}_{BW}(m_{\ell\ell} - m')dm',$$

where f_{exp} is the fraction that the exponential component contributes to the full PDF. A full list of the parameters of the model is given in Table 7.1.

Table 7.1.: List of all parameters of the model for Drell–Yan backgrounds for the fit in the Drell–Yan control region. Given are intial values, allowed ranges and the status of the parameters. A set of these parameters exists for both the central and forward dilepton selection.

	parameter	status	initial value	minimum	maximum
$\mathbf{p}_Z^{ee}$	$m_\mathrm{Z}[\mathrm{GeV}]$	fixed	91.1876	-	-
	$\sigma_\mathrm{Z}[\mathrm{GeV}]$	fixed	2.4952	-	-
	$\mu_{CB}^{ee}[\mathrm{GeV}]$	floating	3.0	-10	10
	σ_{CB}^{ee}	floating	1.6	0	20
	α_1^{ee}	floating	1.16	0	10
	α_2^{ee}	floating	2.5	0	10
	n_1^{ee}	floating	2.9	0	20
	n_2^{ee}	floating	1.04	0	20
	f_{exp}^{ee}	floating	0.9	0	1
	$\mu_{exp}^{ee}[\mathrm{GeV}^{-1}]$	floating	-0.02	-0.1	0
$\mathbf{p}_Z^{\mu\mu}$	$m_\mathrm{Z}[\mathrm{GeV}]$	fixed	91.1876	-	-
	$\sigma_\mathrm{Z}[\mathrm{GeV}]$	fixed	2.4952	-	-
	$\mu_{CB}^{\mu\mu}[\mathrm{GeV}]$	floating	3.0	-10	10
	$\sigma_{CB}^{\mu\mu}$	floating	1.6	0	20
	$\alpha_1^{\mu\mu}$	floating	1.16	0	10
	$\alpha_2^{\mu\mu}$	floating	2.5	0	10
	$n_1^{\mu\mu}$	floating	2.9	0	20
	$n_2^{\mu\mu}$	floating	1.04	0	20
	$f_{exp}^{\mu\mu}$	floating	0.9	0	1
	$\mu_{exp}^{\mu\mu}[\mathrm{GeV}^{-1}]$	floating	-0.02	-0.1	0

Table 7.2.: Fitted $m_{\ell\ell}$ resolution in the central and forward dilepton selections for $e^{\pm}e^{\mp}$ and $\mu^{\pm}\mu^{\mp}$ pairs.

	$e^{\pm}e^{\mp}$	$\mu^{\pm}\mu^{\mp}$
Central	$1.71 \pm 0.03\,\mathrm{GeV}$	$1.44 \pm 0.01\,\mathrm{GeV}$
Forward	$2.70 \pm 0.04\,\mathrm{GeV}$	$2.01 \pm 0.03\,\mathrm{GeV}$

This model is fitted to the data in the Drell–Yan control region separately for $e^{\pm}e^{\mp}$ and $\mu^{\pm}\mu^{\mp}$ events after flavour-symmetric backgrounds are subtracted using OF events. Afterwards, all parameters of the model are fixed and only the normalization is left floating in the fit in the signal region. The resulting fits are shown in Figure 7.1 and are a good description of the distribution in all cases.

From the Gaussian core component of the double-sided crystal ball the $m_{\ell\ell}$ resolution in the different channels is obtained, which is used as an input in the modelling of a potential signal. The resulting resolution values are shown in Table 7.2. The fitted values range form about $1.4\,\mathrm{GeV}$ to $2.7\,\mathrm{GeV}$ depending on lepton flavour and rapidity. In general it is smaller for $\mu^{\pm}\mu^{\mp}$ pairs and for lepton pairs in the central part of the detector.

7.1.2. Model for flavour-symmetric backgrounds

Nominal parametrization

Flavour-symmetric models are described with a model consisting of three parts. The rising flank of the distribution is modelled with a power law, the peak region with a fourth order polynomial and the falling flank with an exponential falloff.

$$\mathcal{P}_{FS}(m_{\ell\ell}) = \begin{cases} \mathcal{P}_{FSE,1}(m_{\ell\ell}) = c_1 \cdot m_{\ell\ell}^{\alpha} & \text{if } 20\,\text{GeV} < m_{\ell\ell} < m_{\ell\ell}^{(1)} \\ \mathcal{P}_{FS,2}(m_{\ell\ell}) = \sum_{i=0}^{3} c_{2,i} \cdot m_{\ell\ell}^{i} & \text{if } m_{\ell\ell}^{(1)} < m_{\ell\ell} < m_{\ell\ell}^{(2)} \\ \mathcal{P}_{FS,3}(m_{\ell\ell}) = c_3 \cdot e^{-\beta m_{\ell\ell}} & \text{if } m_{\ell\ell}^{(2)} < m_{\ell\ell} < 300\,\text{GeV} \end{cases}$$

where $m_{\ell\ell}^{(1)}$ and $m_{\ell\ell}^{(2)}$ are the transition points between the different parts of the model. The model is required to be normalized and also to be continuously differentiable in $m_{\ell\ell}^{(1)}$ and $m_{\ell\ell}^{(2)}$, reducing the number of free parameters to five. A full list of the parameters and their properties is given in Table 7.3.

A variety of alternative models for the flavour-symmetric has been explored to validate the results obtained with the model described above.

Parametrization from 2011 analysis

This parametrization was used in a previous version of the analysis [82]:

$$\mathcal{P}_{FSE}(m_{\ell\ell}) = c_1 m_{\ell\ell}^{\alpha} e^{-\beta m_{\ell\ell}}$$

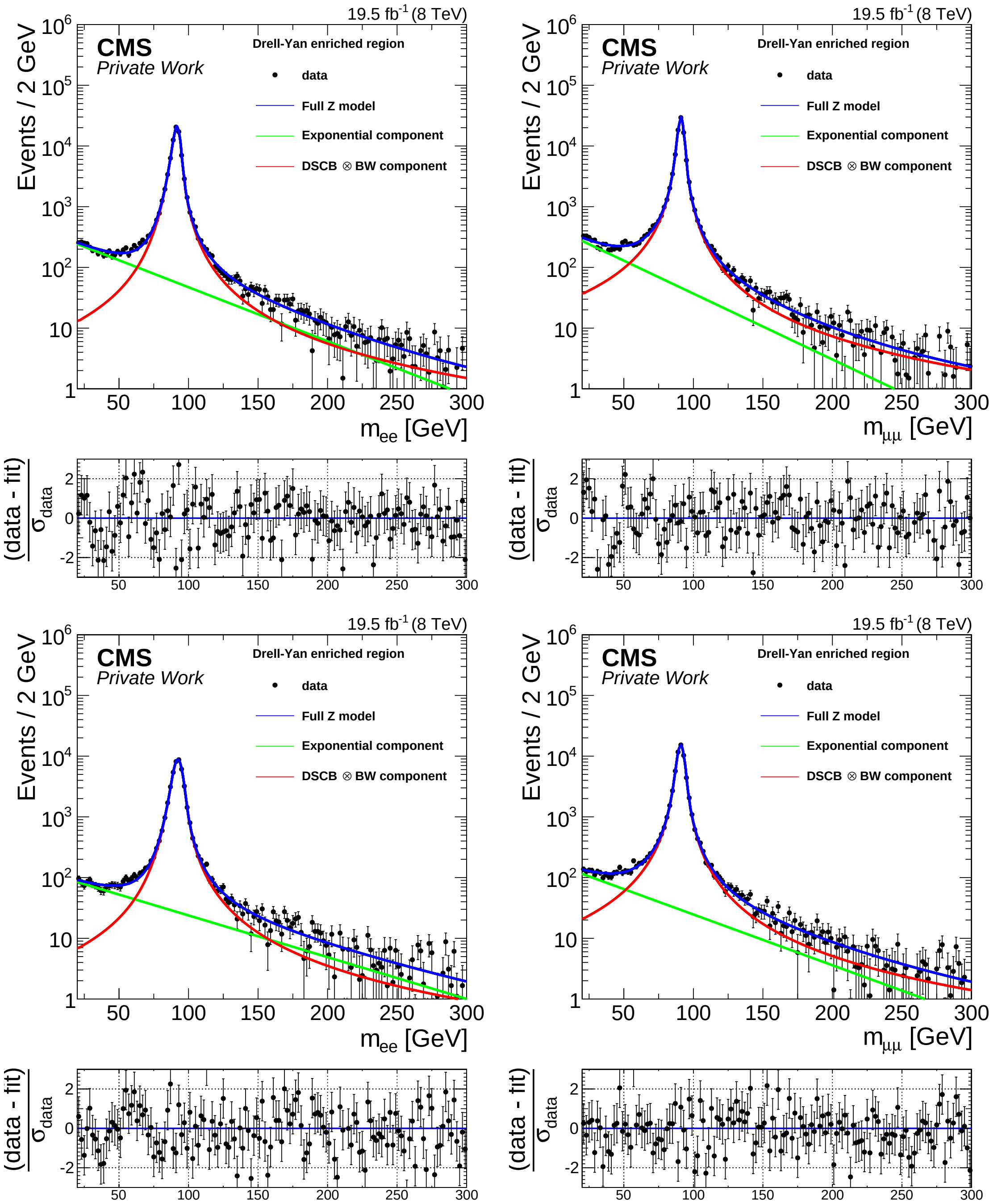

Figure 7.1.: Fit to the $m_{\ell\ell}$ distribution in the Drell–Yan control region separately for $e^{\pm}e^{\mp}$ (left) and $\mu^{\pm}\mu^{\mp}$ (right) events in the central (top) and forward (bottom) dilepton selection. The data is shown as black points while the resulting fit is shown in blue. The red and green lines show the contributions of the continuum model and the peak model to the combined fit.

Table 7.3.: List of all parameters of the model for flavour-symmetric backgrounds. Given are intial values, allowed ranges and the status of the parameters. A set of these parameters exists for both the central and forward dilepton selection.

	parameter	status	initial value	minimum	maximum
	$m_{\ell\ell}^{(1)}$[GeV]	floating	50	20	80
	$m_{\ell\ell}^{(2)}$[GeV]	floating	120	100	160
$\mathbf{p}_{FS}$	$c_{2,0}$	floating	-1800	-5000	5000
	$c_{2,1}$	floating	120	-400	400
	$c_{2,2}$	fixed	1	-	-
	$c_{2,3}$	floating	$2.5 \cdot 10^{-3}$	$1 \cdot 10^{-4}$	$1 \cdot 10^{-2}$

It was found to not describe the distrubtion of flavour-symmetric backgrounds after lepton p_{T} cuts had been raised with respect to the analysis of the 2011 dataset, but is still a useful tool for fit performance studies, as the low number of parameters reduce the runtime of the fit, allowing for tests using a large number of toy datasets.

Sum of three Gaussians

In this case the sum of three Gaussians is chosen as an analytical parametrization of the flavour-symmetric backgrounds. The free parameters of the shape are the means and widths of the Gaussians.

$$\mathcal{P}_{FS}(m_{\ell\ell}) = Gauss(mean_1, \sigma_1) + Gauss(mean_2, \sigma_2) + Gauss(mean_3, \sigma_3)$$

The shape is found to well describe the flavour-symmetric background and to be in good agreement with the default parametrization.

Binned Subtraction

As an alternative to analytical functions, the binned dilepton-mass distribution in the OF channel is directly used as template of the distribution of flavour-symmetric backgrounds in the same-flavour channels. This results in a bin-by-bin subtraction of the flavour-symmetric background estimation from same-flavour yields taking into account the $R_{\mathsf{SF/OF}}$ correction factor, similar to the counting experiment.

This approach has the advantage of not needing any prior knowledge on the shape of the flavour-symmetric background. It is however more susceptible to statistical fluctuations, as they are not smoothed out. In order to minimize the impact of these fluctuations, a bin width of 20 GeV is chosen. This method is not suited to provide quantitative results because the statistical uncertainties on shape are not considered in the fit after it has been fixed on the OF data.

Smoothed Subtraction
Similarly to the binned subtraction, the opposite flavour data distribution is directly used to predict the background in the same flavour distribution. The shape is constructed by adding one Gaussian distribution at the corresponding value of $m_{\ell\ell}$ for each event in the dataset using a one-dimensional kernel pdf (*RooKeysPdf* class in RooFit). In this approach, the probability density function for a sample of a random variable of size n is estimated by a kernel density

$$\hat{f}_h(x) = \frac{1}{nh}\sum_{i=1}^{n} K(\frac{x-x_i}{h}). \tag{7.1}$$

Here K is the so called kernel, for which a normal distribution is chosen, and h is a smoothing parameter[83]. The width of the gaussians is adapted depending on the density of entries at a given point. For both borders, the low-$m_{\ell\ell}$ and the high-$m_{\ell\ell}$ border, parts the gaussians extending beyond the considered range of m_{ll} are mirrored back into the considered range to get the correct integral. Again,this method is not suited to provide quantitative results because no uncertainties on the background shape can be included because it is already fixed prior to the fit.

7.1.3. Signal model

While the shape of the signal depends on the details of the signal model, deviations from a simple triangular shape are small compared to the detector resolution. The signal is therefore modelled by such a triangle, convolved with a Gaussian distribution. The width of the Gaussian $\sigma_{\ell\ell}$ depends on the detector resolution in the corresponding channel and is obtained from the fit to the Z boson peak in the Drell–Yan control region described in Section 7.1.1. The model can be parametrized as

$$\mathcal{P}_S(m_{\ell\ell}) = \frac{1}{\sqrt{2\pi\sigma_{\ell\ell}}}\int_0^{m_{\ell\ell}^{edge}} y\cdot\exp\left(-\frac{(m_{\ell\ell}-y)^2}{2\sigma_{\ell\ell}^2}\right)dy,$$

with the endpoint of the triangle $m_{\ell\ell}^{edge}$ as the only free parameter.

To cross check the dependence of the results on the parametrization of the signal, two additional signal shapes are defined. Here the linear dependence on $m_{\ell\ell}$ is replaced by quartic dependencies with different signs, resulting in concave and convex shapes instead of the simple triangle:

$$\mathcal{P}_S^{\text{concave}}(m_{\ell\ell}) = \frac{1}{\sqrt{2\pi\sigma_{\ell\ell}}}\int_0^{m_{\ell\ell}^{edge}} y^4\cdot\exp\left(-\frac{(m_{\ell\ell}-y)^2}{2\sigma_{\ell\ell}^2}\right)dy,$$

$$\mathcal{P}_S^{\text{convex}}(m_{\ell\ell}) = \frac{1}{\sqrt{2\pi\sigma_{\ell\ell}}}\int_0^{m_{\ell\ell}^{edge}} (m_{\ell\ell}^{edge,4}-(y-m_{\ell\ell}^{edge})^4)\cdot\exp\left(-\frac{(m_{\ell\ell}-y)^2}{2\sigma_{\ell\ell}^2}\right)dy.$$

The parameters of the signal model are listed in Table 7.4.

Table 7.4.: List of all parameters of the signal model. Given are intial values, allowed ranges and the status of the parameters. A set of these parameters exists for both the central and forward dilepton selection.

	parameter	status	initial value	minimum	maximum
$\mathbf{p}_S^{ee}$	$m_{\ell\ell}^{edge}$[GeV]	floating	varying	30	300
	σ_{CB}^{ee}[GeV]	fixed	see Table 7.2	-	-
$\mathbf{p}_S^{\mu\mu}$	$m_{\ell\ell}^{edge}$[GeV]	floating	varying	30	300
	$\sigma_{CB}^{\mu\mu}$[GeV]	fixed	see Table 7.2	-	-

7.2. Combined model

The full models fitted to the different event categories are constructed by adding yield parameters for each component. For opposite flavour events, the model is simply given by

$$\mathcal{P}_{OF}(m_{\ell\ell}) = N_{FS} \cdot \mathcal{P}_{FS}(m_{\ell\ell}).$$

For $e^{\pm}e^{\mp}$ and $\mu^{\pm}\mu^{\mp}$ events, also yield parameters for the Drell–Yan background and the signal models have to be introduced.

$$\begin{aligned}
\mathcal{P}_{ee}(m_{\ell\ell}) &= N_{FS}^{ee} \cdot \mathcal{P}_{FS}(m_{\ell\ell}) + N_Z^{ee} \cdot \mathcal{P}_{Z,ee}(m_{\ell\ell}) + N_S^{ee} \cdot \mathcal{P}_S(m_{\ell\ell}, \sigma_{ee}) \\
\mathcal{P}_{\mu\mu}(m_{\ell\ell}) &= N_{FS}^{\mu\mu} \cdot \mathcal{P}_{FS}(m_{\ell\ell}) + N_Z^{\mu\mu} \cdot \mathcal{P}_{Z,\mu\mu}(m_{\ell\ell}) + N_S^{\mu\mu} \cdot \mathcal{P}_S(m_{\ell\ell}, \sigma_{\mu\mu})
\end{aligned}$$

To reduce the number of free parameters, a universal fraction of $e^{\pm}e^{\mp}$ events in both backgrounds and the signal is assumed and expressed as $0 < f_{ee} < 1$. Also the flavour-symmetric yields in the two SF channels are connected to that in the OF channel via $R_{\mathsf{SF/OF}}$, which allows to construct the following relations:

$$\begin{aligned}
N_S^{ee} &= f_{ee} \cdot N_S, & N_S^{\mu\mu} &= (1 - f_{ee}) \cdot N_S, \\
N_Z^{ee} &= f_{ee} \cdot N_Z, & N_Z^{\mu\mu} &= (1 - f_{ee}) \cdot N_Z, \\
N_{FS}^{ee} &= f_{ee} \cdot R_{\mathsf{SF/OF}} \cdot N_{FS}, & N_{FS}^{\mu\mu} &= (1 - f_{ee}) \cdot R_{\mathsf{SF/OF}} \cdot N_{FS}.
\end{aligned}$$

The systematic uncertainty on $R_{\mathsf{SF/OF}}$ is included in the fit as a constraint in form of a Gaussian PDF with mean and width set to the values measured in section 5.1.3:

$$\mathcal{G}\left(R_{\mathsf{SF/OF}}; R_{\mathsf{SF/OF}}^{\mathsf{measured}}, \sigma_{R_{\mathsf{SF/OF}}}^{\mathsf{measured}}\right).$$

The full likelihood of the model as a function of $m_{\ell\ell}$ for a given set of parameters $\mathbf{p}$ that is fit to the data in the six channels ($e^{\pm}e^{\mp}$,$\mu^{\pm}\mu^{\mp}$, and OF for central and forward lepton selection) is constructed by multiplying the PDFs of the different channels and is given by

$$
\begin{aligned}
\mathcal{L}(m_{\ell\ell};\mathbf{p}) = & \prod_{\text{i = central,forward}} \mathcal{N}_i \\
\times & \prod_{e^{\pm}e^{\mp},i} \left[N_{FS}^{ee,i}\cdot\mathcal{P}_{FS}^{i}(m_{\ell\ell};\mathbf{p}_{FS}^{i}) + N_{Z}^{ee,i}\cdot\mathcal{P}_{Z}^{i}(m_{\ell\ell};\mathbf{p}_{Z}^{ee,i}) + N_{S}^{ee,i}\cdot\mathcal{P}_{S}^{i}(m_{\ell\ell};\mathbf{p}_{S}^{ee,i})\right] \\
\times & \prod_{\mu^{\pm}\mu^{\mp},i} \left[N_{FS}^{\mu\mu,i}\cdot\mathcal{P}_{FS}^{i}(m_{\ell\ell};\mathbf{p}_{FS}^{i}) + N_{Z}^{\mu\mu,i}\cdot\mathcal{P}_{Z}^{i}(m_{\ell\ell};\mathbf{p}_{Z}^{\mu\mu,i}) + N_{S}^{\mu\mu,i}\cdot\mathcal{P}_{S}^{i}(m_{\ell\ell};\mathbf{p}_{S}^{\mu\mu,i})\right] \\
\times & \prod_{e^{\pm}\mu^{\mp},i} \left[N_{FS}^{OF,i}\cdot\mathcal{P}_{FS}^{i}(m_{\ell\ell};\mathbf{p}_{FS}^{i})\right] \\
\times & \mathcal{G}^{i}\left(R_{\mathsf{SF/OF}}^{i}\right),
\end{aligned}
$$

where the different $\mathbf{p}_x^i$ denote the sets of free parameters of the models the $\mathcal{N}_i$ are Poisson factors taking into account the normalization of the different samples. These factors take the form of

$$\mathcal{N}_i = \frac{(N_{FS}^{\ell\ell,i} + N_{Z}^{\ell\ell,i} + N_{S}^{\ell\ell,i})^{N_i^{\ell\ell}} e^{-(N_{FS}^{\ell\ell,i}+N_{Z}^{\ell\ell,i}+N_{S}^{\ell\ell,i})}}{N_i^{\ell\ell}!}$$

for $\ell\ell = e^{\pm}e^{\mp}, \mu^{\pm}\mu^{\mp}$ and

$$\mathcal{N}_i = \frac{(N_{FS}^{\ell\ell,i})^{N_i^{\ell\ell}} e^{-(N_{FS}^{\ell\ell,i})}}{N_i^{\ell\ell}!}$$

for $\ell\ell = e^{\pm}\mu^{\mp}$, with i = Central, Forward. The $N_i^{\ell\ell}$ is the number of observed events in the respective channel.

A full overview over all parameters of the model is shown in Table 7.5. In total, the model has 59 parameters, of which 21 are free parameters in the signal region, 34 describe the Drell–Yan model and four are the mean values and widths of $R_{\mathsf{SF/OF}}$ used in the constraints.

7.3. Fit validation

7.3.1. Fit performance studies using toy MC

The performance of the fit is studied using toy datasets. These are generated by fitting the background shape for flavour-symmetric backgrounds to OF events in simulation. From this shape new opposite-flavour datasets are generated, fluctuating the normalization using a Poisson distribution. Electron-electron and muon-muon datasets are generated from the sum of the shape for flavour-symmetric backgrounds and Z peak model. The normalization of this shape is given by the normalization for flavour-symmetric backgrounds multiplied by $R_{\mathsf{SF/OF}}$ plus the combined JZB and E_T^{miss}-template predictions. This yield is split into the $e^{\pm}e^{\mp}$ and $\mu^{\pm}\mu^{\mp}$ datasets according to the measured $R_{ee/\mathsf{OF}}$ and $R_{\mu\mu/\mathsf{OF}}$ values. Each of the two yields is fluctuated independently according to a Poisson distribution when dicing the toy MC. If desired, a signal is injected in the same-flavour datasets using the nominal signal shape in a

Table 7.5.: List of parameters of the full fit model. For more details on the parameter sets $\mathbf{p}_{FS}$, $\mathbf{p}_{Z}$, and $\mathbf{p}_{S}$ see Tables 7.1, 7.3, and 7.4. For yield parameters the initial value and allowed range are calculated from the observed yields N_{SF} and N_{SF} in the signal region for both the central (C) and forward (F) dilepton selection.

parameter	status	initial value	minimum	maximum
		Normalization parameters		
N_{FS}^{C}	floating	$0.7 \cdot N_{OF}^{C}$	0	$2 \cdot N_{OF}^{C}$
N_{FS}^{F}	floating	$0.7 \cdot N_{OF}^{F}$	0	$2 \cdot N_{OF}^{F}$
N_{S}^{C}	floating	0	$-2 \cdot (N_{OF}^{C} - 0.8 \cdot N_{SF}^{C})$	$2 \cdot (N_{OF}^{C} - 0.8 \cdot N_{SF}^{C})$
N_{S}^{F}	floating	0	$-4 \cdot (N_{OF}^{F} - 0.8 \cdot N_{SF}^{F})$	$4 \cdot (N_{OF}^{FS} - 0.8 \cdot N_{SF}^{F})$
N_{Z}^{C}	floating	pred. from data	0	$N_{SF}^{C}(81\,\text{GeV} < m_{\ell\ell} < 101\,\text{GeV})$
N_{Z}^{F}	floating	pred. from data	0	$N_{SF}^{F}(81\,\text{GeV} < m_{\ell\ell} < 101\,\text{GeV})$
		Shape parameters		
$\mathbf{p}_{Z}^{C}$	mixed	see Table 7.1		
$\mathbf{p}_{Z}^{F}$	mixed			
$\mathbf{p}_{FS}^{C}$	mixed	see Table 7.3		
$\mathbf{p}_{FS}^{F}$	mixed			
$\mathbf{p}_{S}^{C}$	mixed	see Table 7.4		
$\mathbf{p}_{S}^{F}$	mixed			
		Constraint parameters		
$R_{SF/OF}^{C}$	constrained	$R_{SF/OF}^{C,\text{meas.}}$	$R_{SF/OF}^{C,\text{meas.}}$ - $4 \cdot \sigma_{R_{SF/OF}}^{C,\text{meas.}}$	$R_{SF/OF}^{C,\text{meas.}} + 4 \cdot \sigma_{R_{SF/OF}}^{C,\text{meas.}}$
$R_{SF/OF}^{F}$	constrained	$R_{SF/OF}^{F,\text{meas.}}$	$R_{SF/OF}^{F,\text{meas.}}$ - $4 \cdot \sigma_{R_{SF/OF}}^{F,\text{meas.}}$	$R_{SF/OF}^{F,\text{meas.}} + 4 \cdot \sigma_{R_{SF/OF}}^{F,\text{meas.}}$

similar fashion. To reflect that the signal yield is expected to be higher in the central dilepton selection, the signal contribution in the forward selection is chosen to be smaller by a factor of three. The combined fit is performed on each of the datasets generated in this fashion. As the nominal background shape is quite resource intensive, the parametrization from the 2011 analysis is used in these studies in order to generate sufficient statistics, after verifying that this has no significant impact of the results. In general around 1000 toys are generated for each configuration.

Studies without signal injection

The edge fit is performed on toys generated from the background models. In one case the toys are fitted with a floating edge position, in the other it fixed at $70\,\mathrm{GeV}$. In contrast to the fit on data, which only searches for excesses, negative signal yields are allowed in these studies to symmetrize the signal yield distributions. Figure 7.2 shows resulting distributions. On the left side, the number of fitted signal events divided by the fitted uncertainty for the central dilepton selection is shown. In the case of the fixed edge the fit results are distributed following a unit Gaussian centred around zero, as expected in absence of a signal. For the case of a floating edge position however, the distribution exhibits two peaks, symmetrically below and above zero. This is a manifestation of the look-elsewhere-effect (LEE) introduced by the degree of freedom of the edge position. On the right side of Figure 7.2, the distributions of the fitted values of $R_{\mathrm{SF/OF}}$ are shown, again for the central selection. In both cases the value used in the generation of the toys of 1.013 is well reproduced. Also, the width of the distribution is identical in both cases, illustrating that the floating edge position does not introduce biases apart from favouring results with a higher number of signal events.

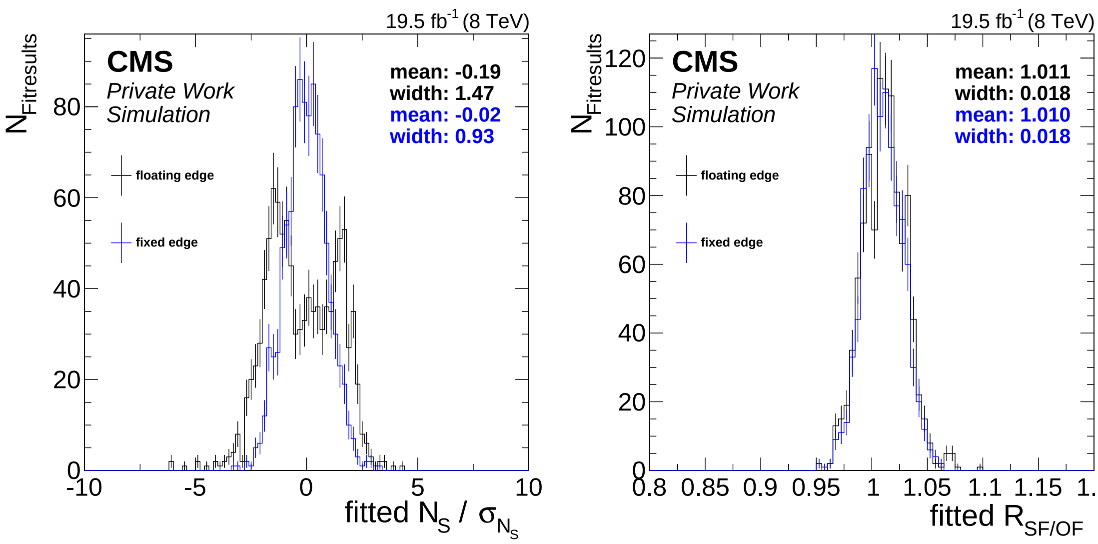

Figure 7.2.: Distribution of fit observables in toy studies for a background only scenario. Shown are the fitted number of signal events divided by their uncertainty in the central region (left) and the corresponding fitted values of $R_{\mathrm{SF/OF}}$ (right). Shown are results for a floating edge (black) and a fixed edge position (blue).

The distribution of the fitted edge position versus the initial value is shown in Figure 7.3. The initial values has been randomized between 0 and $300\,\mathrm{GeV}$. To ensure that the initial value is inside the allowed range for $m_{\ell\ell}^{edge}$, diced values below $35\,\mathrm{GeV}$ are set to this value. In absence of a signal a strong correlation between the initial and observed value of $m_{\ell\ell}^{edge}$ is observed. This suggests that the fit tends to converge to the next local minimum of the negative log-likelihood. It is therefore necessary to choose a suitable initial value close to the global minimum before the fit is performed.

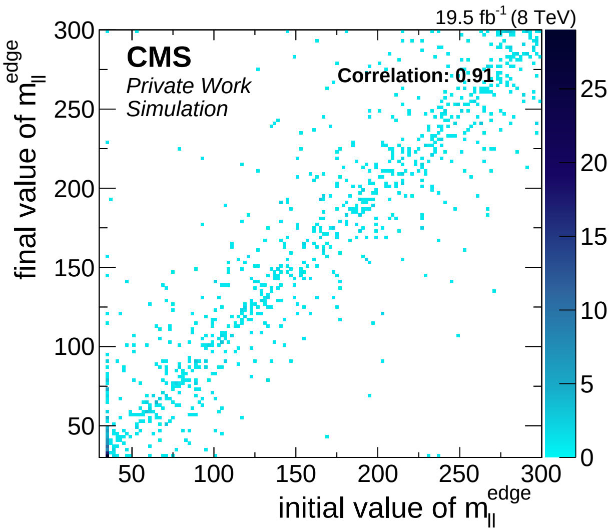

Figure 7.3.: Distribution of fitted versus initial values of $m_{\ell\ell}^{edge}$ in the case of the randomized initial values for toys without an injected signal.

As an additional check, toys are generated with $R_{\mathrm{SF/OF}}$ shifted by $\pm1\sigma$. These toys are fitted with the Gaussian constraint to the central value and the results are shown in Figure 7.4. The same distributions are shown as above. In the case of the signal yield divided by its uncertainty, the double peak structure observed in the nominal configuration changes to a single peak that is shifted to negative signal yields for the toys generated with lower and to positive signal yields for those generated with higher values of $R_{\mathrm{SF/OF}}$. For the fitted values of $R_{\mathrm{SF/OF}}$, the width of the distribution is unchanged, but the systematic shifts in the generation of the toys is reflected in their means. However, the observed shifts of the mean (0.025 and -0.023) are smaller than those introduced the generation of the toys (±0.037, the uncertainty of $R_{\mathrm{SF/OF}}$), suggesting that part of the systematic shift is absorbed by the fit by introducing a signal contribution.

Toy studies with signal injection

The fit performance in the presence of a signal is tested by injection a signal of 125 events with and edge position of 70 GeV in the central region and again a third of that number in the forward signal region. Figure 7.5 shows the resulting distribution of fit results for a selection of observables in the central signal region. The distribution of the number of signal events is well described by a Gaussian with a mean of about 126 events, very close to the injected number, and a width of 41 events. Divided by the fitted uncertainty this gives a unit Gaussian with a mean of about 2.9. The edge position is also Gaussian distributed, with a mean of about $70\,\mathrm{GeV}$, also reproducing the injected value very well, with a width of about $1.8\,\mathrm{GeV}$. Comparing the distribution of $R_{\mathsf{SF/OF}}$ with that in Figure 7.2, it can be seen that the presence of a signal does not bias the result towards higher values.

To study the dependence of the fit result on the edge position, toys are generated with a signal of 125 events in the central signal region injected for different values of $m_{\ell\ell}^{edge}$ between 40 and 200 GeV in steps of 10 GeV. For each configuration, about 1000 fits are performed. The initial value of $m_{\ell\ell}^{edge}$ is chosen to coincide with the generated one. The distributions of the fitted $m_{\ell\ell}^{edge}$ and number of signal events for each generated $m_{\ell\ell}^{edge}$ are shown in Figure 7.6. In the case of the fitted $m_{\ell\ell}^{edge}$ on the left side, the generated value is in general very well reproduced by the fit. The best results are obtained for low values of $m_{\ell\ell}^{edge}$, as the signal shape is much steeper and easier to separate from the background as for higher values. Towards higher values the spread of the results and especially the probability for very large deviation from the generated value increases, before they decrease slightly towards very high values of the generated $m_{\ell\ell}^{edge}$. A notable feature is observed for generated values of 100 GeV, where for a small number of fits the fitted value is very close to the Z boson mass. Similar behaviour is also observed for the number of fitted signal events. Here the relative size of the deviation

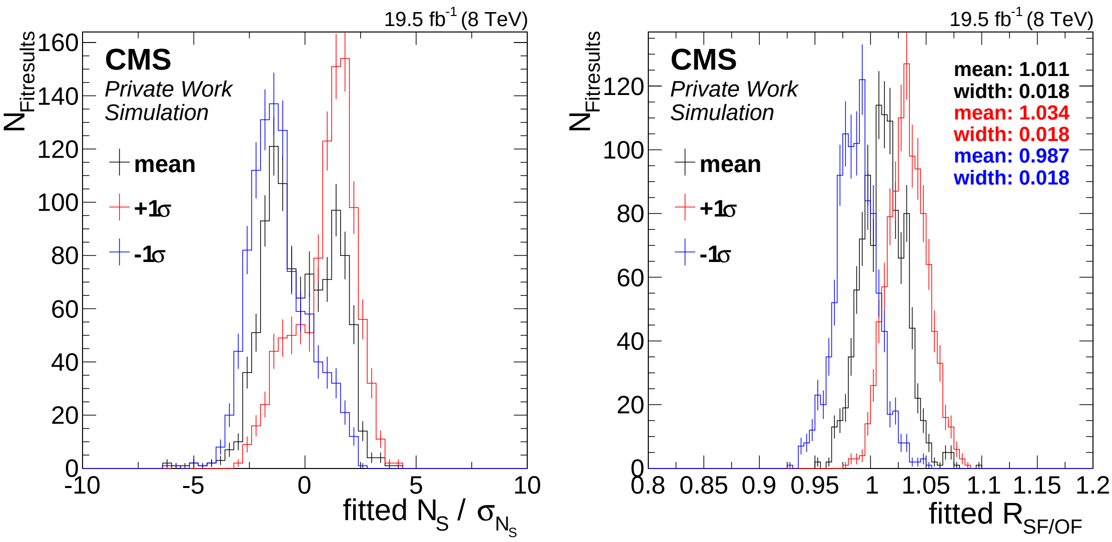

Figure 7.4.: Distribution of fit observables in toy studies for background only toys with fixed edge position. Shown are the fitted number of signal events in the central region (left) and the fitted number of signal events divided by the fitted uncertainty in the central region (right).

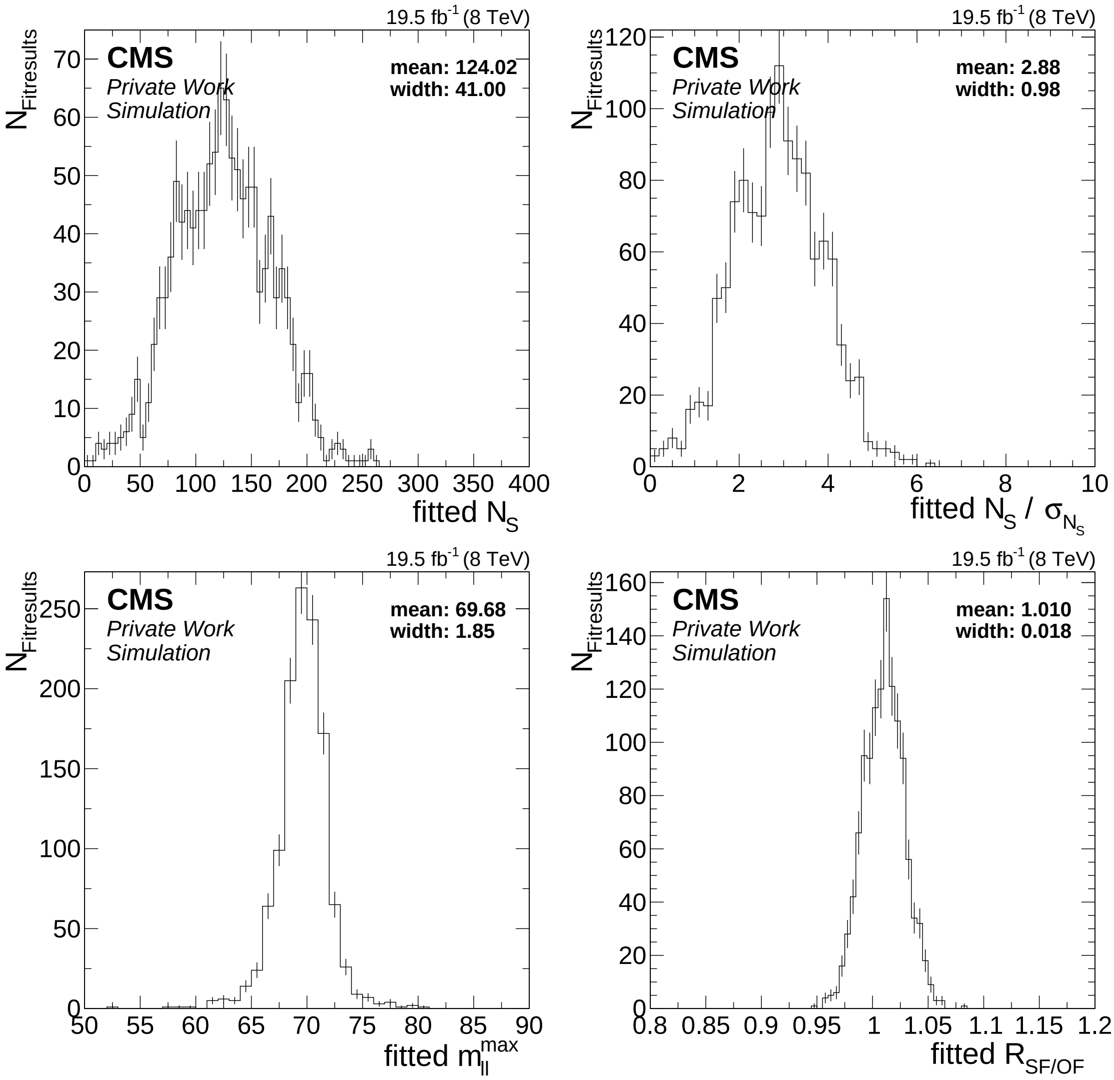

Figure 7.5.: Distribution of fit observables in toy studies with a signal injected. Shown are the fitted number of signal events in the central region (upper left), the fitted number of signal events divided by the fitted uncertainty in the central region (upper right), the fitted edge position (lower left) and the fitted $R_{\mathrm{SF/OF}}$ in the central region (lower right).

form the generated value is much larger, as the event yields are fluctuated in the generation of the toys.

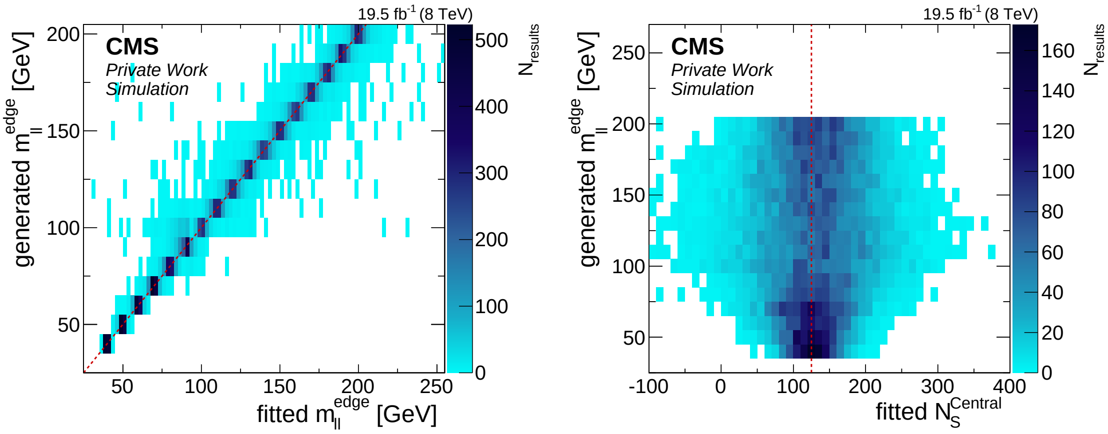

Figure 7.6.: Distributions of the fitted $m_{\ell\ell}^{edge}$ (left) and the number of signal events (right) for each generated $m_{\ell\ell}^{edge}$. The frequency of the results is colour-coded, darker colours indicating higher values. The dashed red lines indicate the points at which the fitted result matches the generated value.

The width of the distribution of the fitted $m_{\ell\ell}^{edge}$ is shown on the left side of Figure 7.7. It is quantified both with the root mean square (RMS) of the distribution and the width of a Gaussian fitted in a range of $\pm 3\,\mathrm{GeV}$ around the generated value. The first is sensitive to the non-Gaussian tails of the distribution while the latter is a measure of the core resolution. For generated values of $m_{\ell\ell}^{edge}$ of $40\,\mathrm{GeV}$, the two values are the same, but quickly deviate for higher edge positions. The Gaussian width rises from about $1\,\mathrm{GeV}$ to about $2-2.5\,\mathrm{GeV}$ for edge position above $80\,\mathrm{GeV}$ and is roughly constant for higher edge positions. The RMS reaches values of $4\,\mathrm{GeV}$ for edges below the Z mass. For $\mathrm{m}_{\ell\ell}^{\mathrm{edge}} = 100\,\mathrm{GeV}$ it is much larger, caused by the bias towards the Z mass observed in Figure 7.6. Above the Z peak the RMS of the distribution is stable at $8\,\mathrm{GeV}$ before it drops off again at very high edge positions.

The right side of Figure 7.7 shows the means and widths of fits of Gaussian functions to the distributions of $N_S^{central}$, again as a function of the generated $m_{\ell\ell}^{edge}$. The distributions do not exhibit significant non-Gaussian tails, so the RMS value is not shown in this case. The injected value of 125 events reproduced within about 8 events for all values of $m_{\ell\ell}^{edge}$. The width increases with $m_{\ell\ell}^{edge}$ from roughly 25 to 65 events at $m_{\ell\ell}^{edge}$ of $100\,\mathrm{GeV}$ and decreases slightly for higher values.

To test deviations from the assumed signal shape, toys are generated with and signal injected at $\mathrm{m}_{\ell\ell}^{\mathrm{edge}} = 70\,\mathrm{GeV}$ and a size of 125 events, but following the convex and concave signal shapes described in section 7.1.3. They are then fitted using the nominal triangular signal shape. Resulting distributions are shown in Figure 7.8. When fitting a concave signal with the triangular shape a bias towards higher signal yields of 20 events is introduced, together with a preference of slightly higher values for $m_{\ell\ell}^{edge}$. This higher signal yield is achieved by systematically reducing the value of $R_{\mathsf{SF/OF}}$. Less strong effects are observed in the case of a convex signal. Here a bias towards a reduced signal yield of about 10 events is present, together with a much wider distribution of the fitted $m_{\ell\ell}^{edge}$. In this case, no change in the distribution of the fitted $R_{\mathrm{SF/OF}}$ compared to the nominal signal shape is observed.

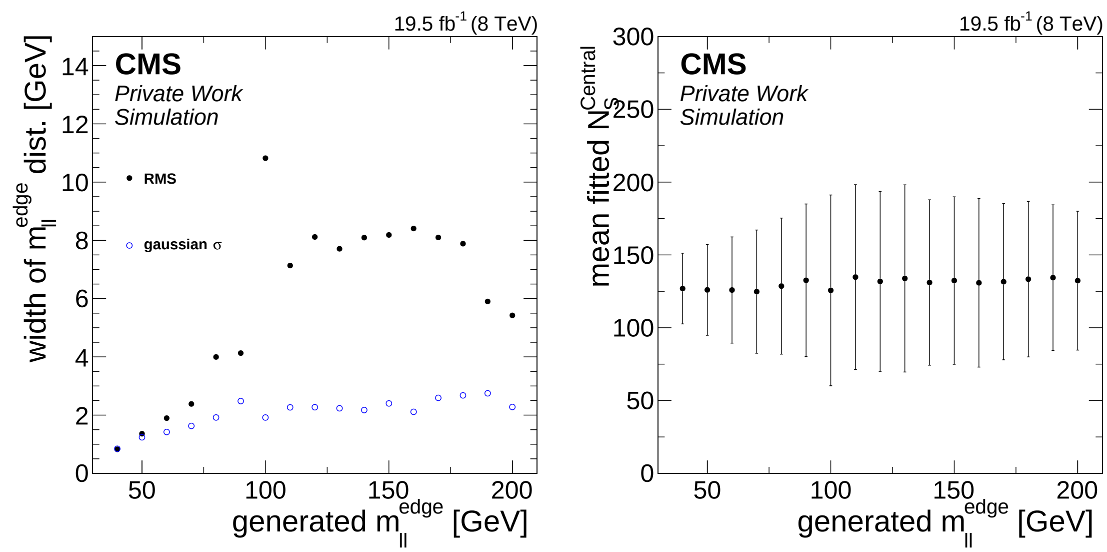

Figure 7.7.: Fitted idths of the $m_{\ell\ell}^{edge}$ (left) and means and widths $N_S^{central}$ distributions (right) as a function of the generated $m_{\ell\ell}^{edge}$.

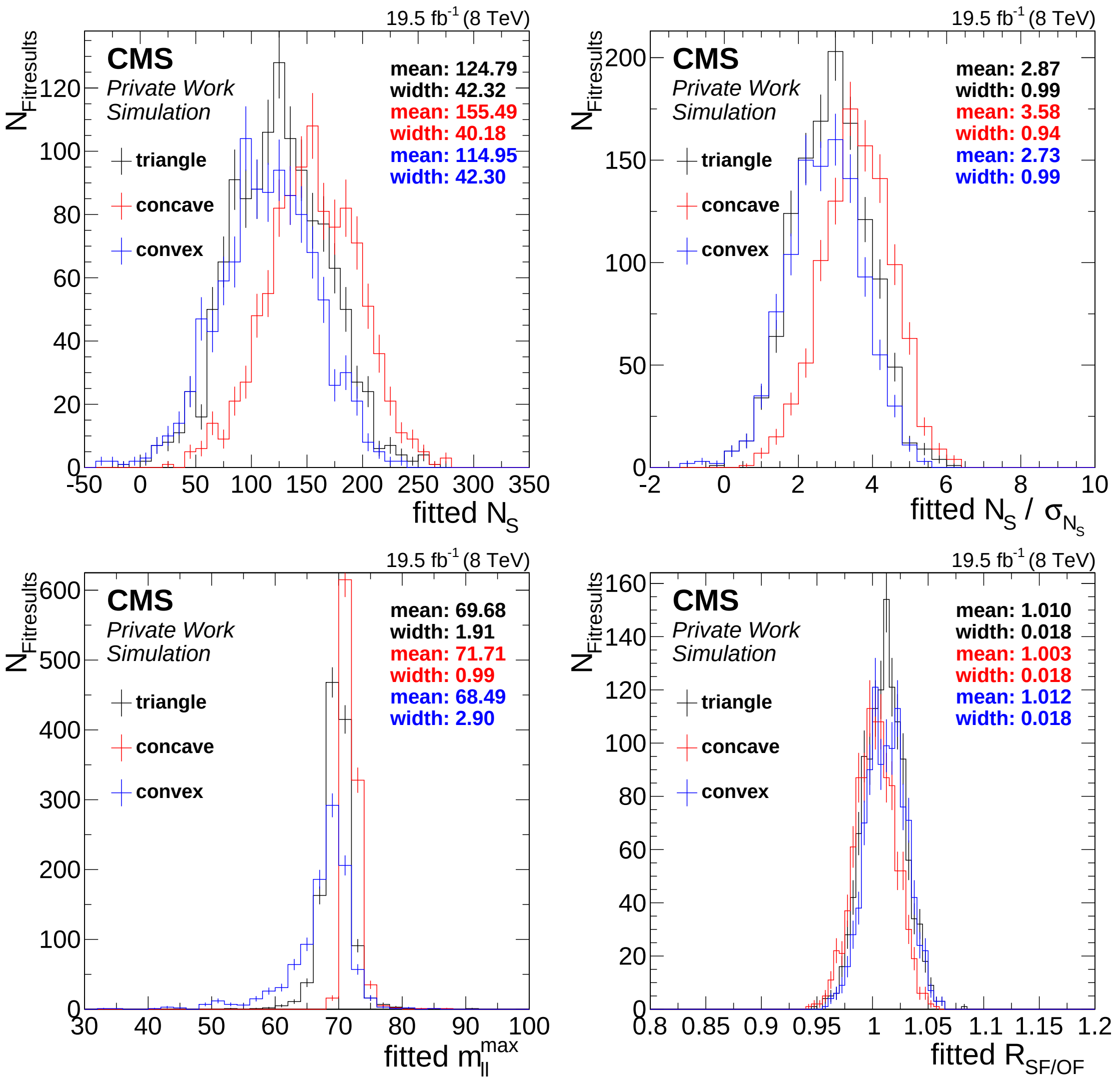

Figure 7.8.: Distribution of fit observables in toy studies with signals following different distributions. Toys are generated using the nominal (black) as well as the concave (red) and convex (blue) signal shape. Shown are the fitted number of signal events in the central region (upper left), the fitted number of signal events divided by the fitted uncertainty in the central region (upper right), the fitted edge position (lower left) and the fitted $R_{\text{SF/OF}}$ in the central region (lower right).

7.4. Results

The result of the fit performed in the signal region on data is shown in Figure 7.9. Shown are the $m_{\ell\ell}$ distributions in the SF and OF channels for the central and forward dilepton selection. The quantitative results are shown in Table 7.6. Similar to the counting experiment, an excess of events is observed below the Z boson peak in the central signal region. The best fit value for the position of an edge is found to be $82.4\,\mathrm{GeV}$, with an signal yield of 140±43 events. No significant contribution of a signal is found in the forward region, where the fitted signal yield is 1±22 events. In the central region the fitted value of $R_{\mathrm{SF/OF}}$ is slightly larger than the initial value, indicating that the fit absorbs some fraction of the excess into the background prediction. However, the difference is small compared to the fitted uncertainty and the uncertainty on the predicted value. In the forward region, the fitted value is smaller than the initial value, but also this deviation is well within the uncertainties.

Table 7.6.: Results of the fit in search for a kinematic edge in the signal region.

	Central	Forward
Drell–Yan background	170±23	55±15
Flav. Sym. background in OF	2293±45	792±25
$R_{\mathrm{SF/OF}}$	1.024±0.027	1.012±0.042
signal events	140±43	1±22
$m_{\ell\ell}^{edge}$ [GeV]	$82.4^{+2.1}_{-3.3}$	
local significance [σ]	2.5	

A scan of the log-likelihood as a function of the edge position $m_{\ell\ell}^{egde}$ is shown in Figure 7.10. The values have been shifted to set the minimum to zero. The curve exhibits a sharp drop at the best fit value for $m_{\ell\ell}^{egde}$, which is indeed the global minimum over the considered mass range.

The local fit significance is calculated applying Wilk's Theorem [84], which states that the distribution of $-2(log(L_1) - log(L_0))$ ($-2\Delta(log(L))$ in short) is distributed as a χ^2 distribution with n degrees of freedom, where n is the number of free parameters of the signal model and L_0 and L_0 are the likelihood values of the background only and the signal plus background hypothesis. The p-Value of a result can then be obtained by simply integrating this χ^2 distribution for values larger than the one observed in data. However, Wilk's Theorem does not hold in cases where one parameter of the signal model is not defined in the background only model. This is the case for signal models including the position of a bump, or in this case an edge, as a free parameter.

The applicability of Wilk's theorem is demonstrated using the toy fits described in Section 7.3.1. They can also be used to calculate directly the significance and are also able to provide global results. Considered are toy dataset without signal injection. The fits are performed both with a floating edge position and fixed $m_{\ell\ell}^{edge}$. Figure **??** shows the resulting distributions of $-2\Delta(log(L))$ for the both scenarios. The χ^2 distributions for 2 and 3 degrees of freedom are

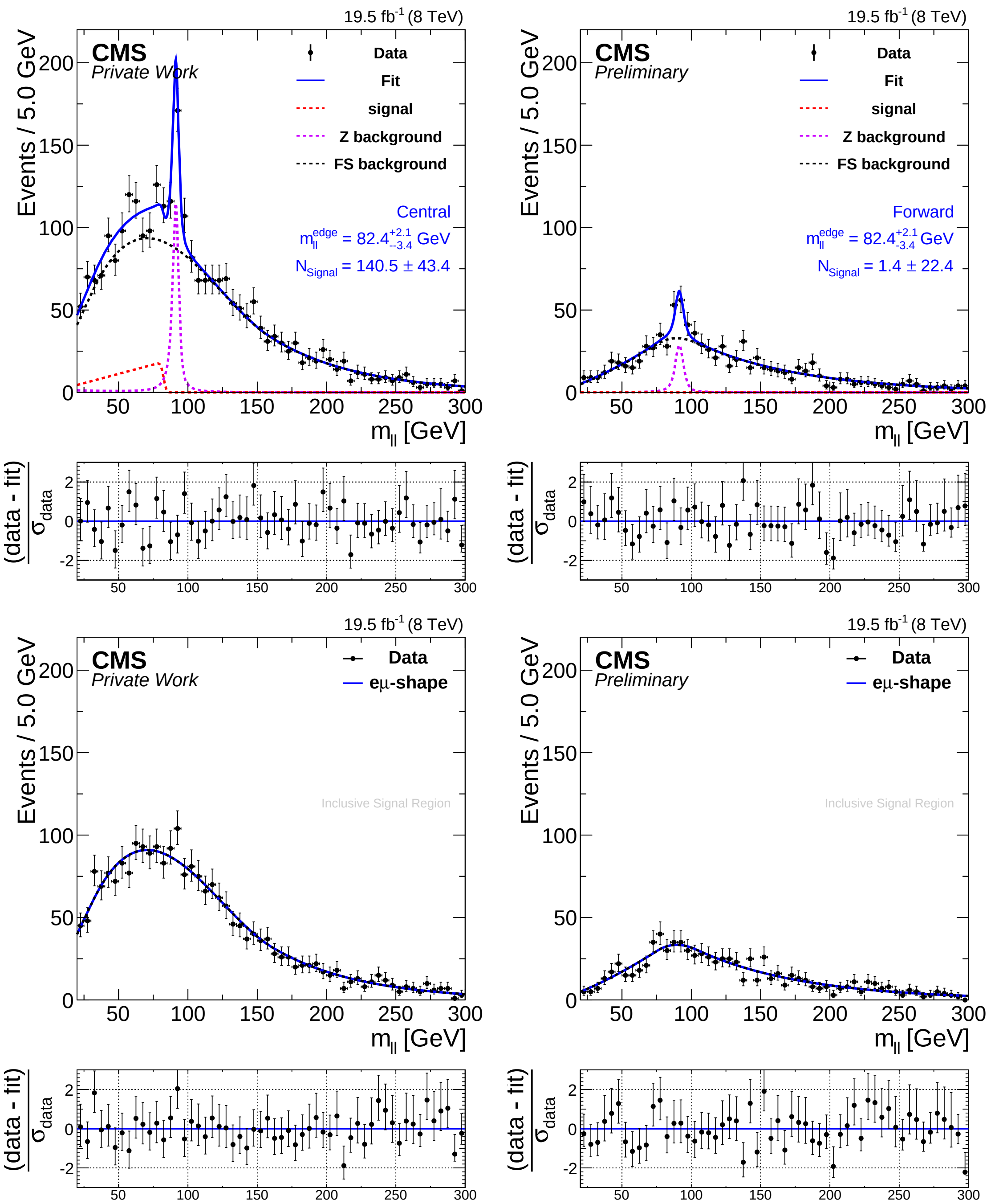

Figure 7.9.: Fit results in the signal region. Shown are the $m_{\ell\ell}$ distributions in SF (top) and OF (bottom) events for the central (right) and forward (left) dilepton selection. The fit is shown as a solid blue line while the different components are shown as dashed line, the signal model in red, the Drell–Yan model in violet and the flavour-symmetric model in black.

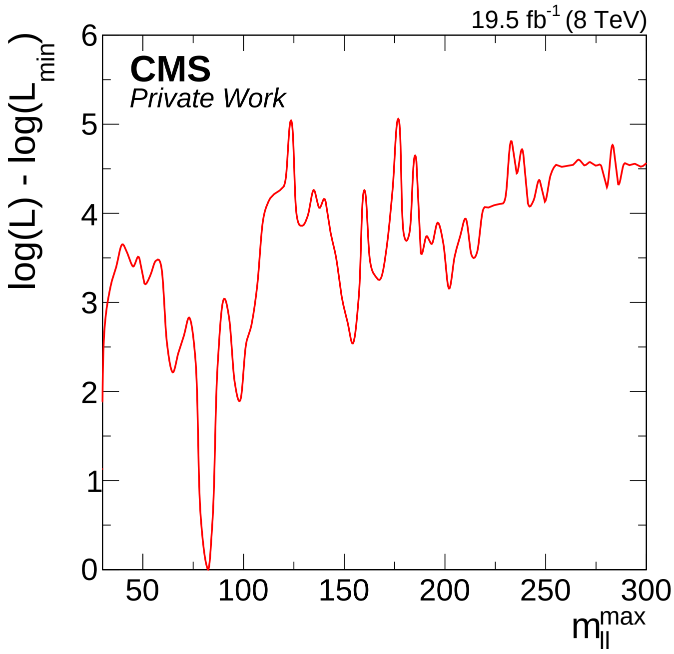

Figure 7.10.: Scan of the observed log-likelihood in the signal region subtracted by the minimal value as a function of $m_{\ell\ell}^{max}$.

shown for illustration. In the case of the fixed edge the results of the fits follow the distribution for 2 degrees of freedom, as expected from the presence of N_S^{central} and N_S^{forward}. This proves the applicability of Wilk's theorem for this case. The floating edge position however clearly does not simply act as an additional degree of freedom as the distribution of the toy results is shifted to higher values of $-2\Delta(log(L))$, indicating that Wilk's theorem does indeed not hold for this type of models. The p-Value of the fit result is in both cases given by the fraction of results for with $-2\Delta(log(L))$ exceeds the one observed on data. The result for a fixed edge can then be interpreted as a local p-Value while the ones for a floating edge gives a global p-Value taking into account the so called "Look-elsewhere-effect" [85]. However, as the signal yield is allowed to be negative, the resulting p-Values have to be reduced by a factor of two to take into account that we only consider positive signals to have physical meaning [85]. This corrected p-Value is translated into a significance interpreting it as the one-sided tail probability of a unit Gaussian. The resulting uncorrected p-Values are $0.012^{+0.004}_{-0.003}$, corresponding to 2.5σ, in the local and $0.091^{+0.009}_{-0.009}$, corresponding to 1.7σ, in the global case.

As the applicability of Wilk's theorem has been established, local p-Values and significances can be calculated analytically from the χ^2 function for two degrees of freedom. The p-Value is defined as the integral of the function above the value of $-2\Delta(log(L))$ observed on data for a fit performed with fixed edge position. Performing such a fit on data with $m_{\ell\ell}^{edge}$ set to the observed value, this results in a p-Value of 0.014, corresponding to a significance of 2.5σ. This is well compatible with the result observed using toy MC. The local significances reported in Table 7.6 and those discussed in the following are calculated using the analytical calculation as it is much faster and not affected by statistical uncertainties. Also the toys have the small caveat that a different background shape as in the nominal fit is used.

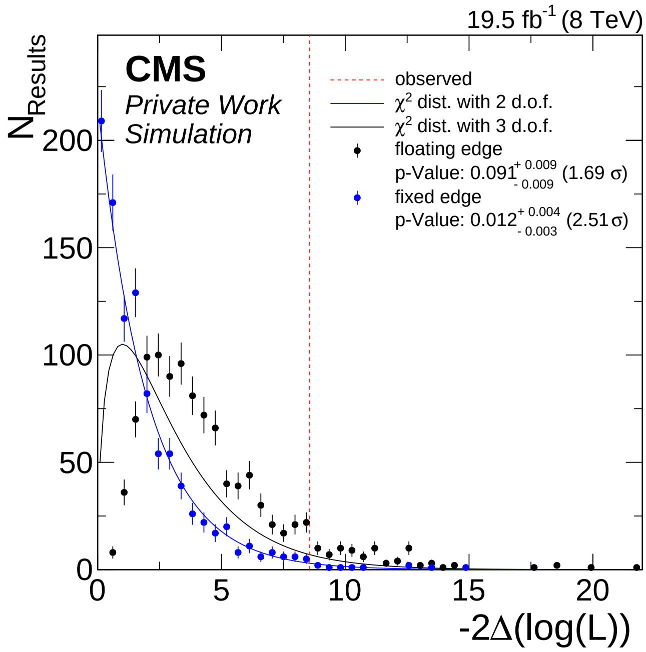

Figure 7.11.: Calculation of the fit significance using background only toy MC. Shown are the distribution of $-2\Delta(log(L))$ for fits with floating (black) and fixed (blue) edge position. Also shown are χ^2 distributions for 2 (blue) and 3 (black) degrees of freedoms. The dashed red line indicates the value of $-2\Delta(log(L))$ observed on data in case of a floating edge.

As further validation of the result on data, the results obtained with different parametrization of the flavour-symmetric background are compared to the nominal result in Table 7.7. For the sake of clarity, only yields in the central signal region are shown. However, similar agreement is observed also in the forward signal region. In general, there is good agreement between all considered parametrizations. The best agreement is seen in the number of fitted flavour-symmetric events in the OF sample, which is expected as here the fit is mist simple, consisting only of one the shape for flavour-symmetric backgrounds. Good agreement is also observed for $m_{\ell\ell}^{egde}$ and the number of signal events, which are stable against the choice of background model. The most differences are observed for $R_{\mathrm{SF/OF}}$ and the yield of the Z model. Here the fit can trade one against the other, depending on the parametrization of the flavour-symmetric background. Here the largest deviations are observed for the shape used in the analysis of the $7\,\mathrm{TeV}$ dataset. As this shape is known to not satisfactorily described the flavour-symmetric background, it is encouraging to see that the fit result is stable against such biases. The observed local significance is very similar among all analytical parametrizations. In the case of the KDE and the binned parametrization, the shape of the distribution is not free in the fit, as discussed above, excluding the statistical uncertainty of the OF sample from the fit and resulting in an systematically larger local significance.

To compare the fit result with that of the counting experiment, the fitted event yields in the low-mass region for central dilepton events have been derived. They are shown in Table **??**, together with the background predictions and observed yield of the counting experiment in that region. Also the fitted yield for Drell–Yan backgrounds in the on-Z region is compared to

Table 7.7.: Comparison of edge fit results in the signal region for different parametrizations of the flavour-symmetric background. Results are given for the central signal region only. Similar agreement between the parametrization is observed also in the forward signal region.

	N_Z	N_{FS}	$R_{\text{SF/OF}}$	N_S	$m_{\ell\ell}^{edge}$ [GeV]	local σ
nominal	170±23	2293±45	1.024±0.027	140±43	$82.4^{+2.1}_{-3.3}$	2.5
sum of Gaussians	168±24	2292±44	1.023±0.027	146±50	$82.1^{+2.2}_{-3.7}$	2.7
kernel density estimation	154±22	2296±43	1.028±0.026	141±41	$81.7^{+2.3}_{-3.4}$	3.1
histogram	140±23	2296±43	1.029±0.026	153±41	$83.0^{+1.7}_{-2.4}$	3.5
2011 shape	181±23	2290±43	1.020±0.026	146±46	$82.8^{+1.9}_{-2.5}$	2.7

the prediction. The fitted yield exceeds that of the prediction by 26 events, a difference that is well covered by the uncertainties of the fit and the prediction. In the low-mass region good agreement between counting experiment and fit is observed, also. The Drell–Yan background is again fitted higher than expected from the prediction, as the ratio between the off-shell component and the peak is fixed and the normalization of this model is determined dominantly on the Z boson peak. In the fit the contribution of flavour-symmetric backgrounds is increased, caused by the increased value of $R_{\text{SF/OF}}$. This is reflected in a signal yield that is lower by 11 events. For all considered components the use of shape information has allowed for reduced uncertainties on the event yields, most notably on the yield for flavour-symmetric backgrounds.

Table 7.8.: Comparison of the fit result and the result of the counting experiment in the low mass region for central leptons. The PDFs contributing to the fit model are integrated in the region $20 < m_{\ell\ell} < 70$ GeV to obtain the fitted yields in this interval. Also the yield in the on-Z region is calculated and compared to the prediction.

	Fit	Counting experiment
on-Z region		
Drell–Yan background	145±19	119±21
low-mass region		
Drell–Yan background	10±1	8±2
Flav. Sym. background	760±14	746±37
signal events	98±30	109±48

8. Outlook to LHC Run II

9. Conclusion

A. Data and Monte Carlo Samples

process	sample
$t\bar{t} \to b\bar{b}l\nu l\nu$	/TTJets_FullLeptMGDecays_8TeV-madgraph-tauola/Summer12_DR53X-PU_S10_START53_V7C-v2/AODSIM
$t\bar{t} \to b\bar{b}q\bar{q}l\nu$	/TTJets_SemiLeptMGDecays_8TeV-madgraph-tauola/Summer12_DR53X-PU_S10_START53_V7C-v1/AODSIM
$t\bar{t} \to b\bar{b}q\bar{q}q\bar{q}$	/TTJets_HadronicMGDecays_8TeV-madgraph/Summer12_DR53X-PU_S10_START53_V7A_ext-v1/AODSIM
$Z/\gamma^* \to l^+l^-$ 10 GeV $< m_{ll} <$ 50 GeV	/DYJetsToLL_M-10To50filter_8TeV-madgraph/Summer12_DR53X-PU_S10_START53_V7A-v1/AODSIM
$Z/\gamma^* \to l^+l^-$ $m_{ll} >$ 50 GeV	/DYJetsToLL_M-50_TuneZ2Star_8TeV-madgraph-tarball/Summer12_DR53X-PU_S10_START53_V7A-v1/AODSIM
$W \to l\nu$	/WJetsToLNu_TuneZ2Star_8TeV-madgraph-tarball/Summer12_DR53X-PU_S10_START53_V7A-v2/AODSIM
$ZZ \to l^+l^-q\bar{q}$	/ZZJetsTo2L2Q_TuneZ2star_8TeV-madgraph-tauola/Summer12_DR53X-PU_S10_START53_V7A-v1/AODSIM
$ZZ \to l^+l^-\nu\nu$	/ZZJetsTo2L2Nu_TuneZ2star_8TeV-madgraph-tauola/Summer12_DR53X-PU_S10_START53_V7A-v3/AODSIM
$ZZ \to l^+l^-l^+l^-$	/ZZJetsTo4L_TuneZ2star_8TeV-madgraph-tauola/Summer12_DR53X-PU_S10_START53_V7A-v1/AODSIM
$WZ \to l\nu l^+l^-$	/WZJetsTo3LNu_TuneZ2_8TeV-madgraph-tauola/Summer12_DR53X-PU_S10_START53_V7A-v1/AODSIM
$WZ \to qq'l^+l^-$	/WZJetsTo2L2Q_TuneZ2star_8TeV-madgraph-tauola/Summer12_DR53X-PU_S10_START53_V7A-v1/AODSIM
$WW \to l\nu l\nu$	/WWJetsTo2L2Nu_TuneZ2star_8TeV-madgraph-tauola/Summer12_DR53X-PU_S10_START53_V7A-v1/AODSIM
t s-Channel	/T_s-channel_TuneZ2star_8TeV-powheg-tauola/Summer12_DR53X-PU_S10_START53_V7A-v1/AODSIM
t t-Channel	/T_t-channel_TuneZ2star_8TeV-powheg-tauola/Summer12_DR53X-PU_S10_START53_V7A-v1/AODSIM
t tW-Channel	/T_tW-channel-DR_TuneZ2star_8TeV-powheg-tauola/Summer12_DR53X-PU_S10_START53_V7A-v1/AODSIM
$\bar{t}$ s-Channel	/Tbar_s-channel_TuneZ2star_8TeV-powheg-tauola/Summer12_DR53X-PU_S10_START53_V7A-v1/AODSIM
$\bar{t}$ t-Channel	/Tbar_t-channel_TuneZ2star_8TeV-powheg-tauola/Summer12_DR53X-PU_S10_START53_V7A-v1/AODSIM
$\bar{t}$ tW-Channel	/Tbar_tW-channel-DR_TuneZ2star_8TeV-powheg-tauola/Summer12_DR53X-PU_S10_START53_V7A-v1/AODSIM
WWW	/WWWJets_8TeV-madgraph/Summer12_DR53X-PU_S10_START53_V7A-v1/AODSIM
$WW\gamma$	/WWGJets_8TeV-madgraph/Summer12_DR53X-PU_S10_START53_V7A-v1/AODSIM
WWZ	/WWZNoGstarJets_8TeV-madgraph/Summer12_DR53X-PU_S10_START53_V7A-v1/AODSIM
WZZ	/WZZNoGstarJets_8TeV-madgraph/Summer12_DR53X-PU_S10_START53_V7A-v1/AODSIM
$t\bar{t}\gamma$	/TTGJets_8TeV-madgraph/Summer12_DR53X-PU_S10_START53_V7A-v1/AODSIM
$t\bar{t}W$	/TTWJets_8TeV-madgraph/Summer12_DR53X-PU_S10_START53_V7A-v1/AODSIM
$t\bar{t}Z$	/TTZJets_8TeV-madgraph_v2/Summer12_DR53X-PU_S10_START53_V7A-v1/AODSIM
$t\bar{t}WW$	/TTWWJets_8TeV-madgraph/Summer12_DR53X-PU_S10_START53_V7A-v1/AODSIM
$t\bar{t}$	/TTJets_MassiveBinDECAY_TuneZ2star_8TeV-madgraph-tauola/Summer12_DR53X-PU_S10_START53_V7A-v1/AODSIM
$t\bar{t}$, $m_{top} =$ 166.5 GeV	/TTJets_mass166_5_TuneZ2star_8TeV-madgraph-tauola/Summer12_DR53X-PU_S10_START53 V7A-v1/AODSIM
$t\bar{t}$, $m_{top} =$ 169.5 GeV	/TTJets_mass169_5_TuneZ2star_8TeV-madgraph-tauola/Summer12_DR53X-PU_S10_START53 V7A-v1/AODSIM
$t\bar{t}$, $m_{top} =$ 175.5 GeV	/TTJets_mass175_5_TuneZ2star_8TeV-madgraph-tauola/Summer12_DR53X-PU_S10_START53 V7A-v1/AODSIM
$t\bar{t}$, $m_{top} =$ 178.5 GeV	/TTJets_mass178_5_TuneZ2star_8TeV-madgraph-tauola/Summer12_DR53X-PU_S10_START53 V7A-v1/AODSIM
$t\bar{t}$, Matching scale up	/TTJets_matchingup_TuneZ2star_8TeV-madgraph-tauola/Summer12_DR53X-PU_S10_START53 V7A-v1/AODSIM
$t\bar{t}$, Matching scale down	/TTJets_matchingdown_TuneZ2star_8TeV-madgraph-tauola/Summer12_DR53X-PU_S10_START53 V7A-v1/AODSIM
$t\bar{t}$, Factorization scale up	/TTJets_scaleup_TuneZ2star_8TeV-madgraph-tauola/Summer12_DR53X-PU_S10_START53 V7A-v1/AODSIM
$t\bar{t}$, Factorization scale down	/TTJets_scaledown_TuneZ2star_8TeV-madgraph-tauola/Summer12_DR53X-PU_S10_START53 V7A-v1/AODSIM

Table A.1.: Bla

B. Dependencies of $r_{\mu e}$

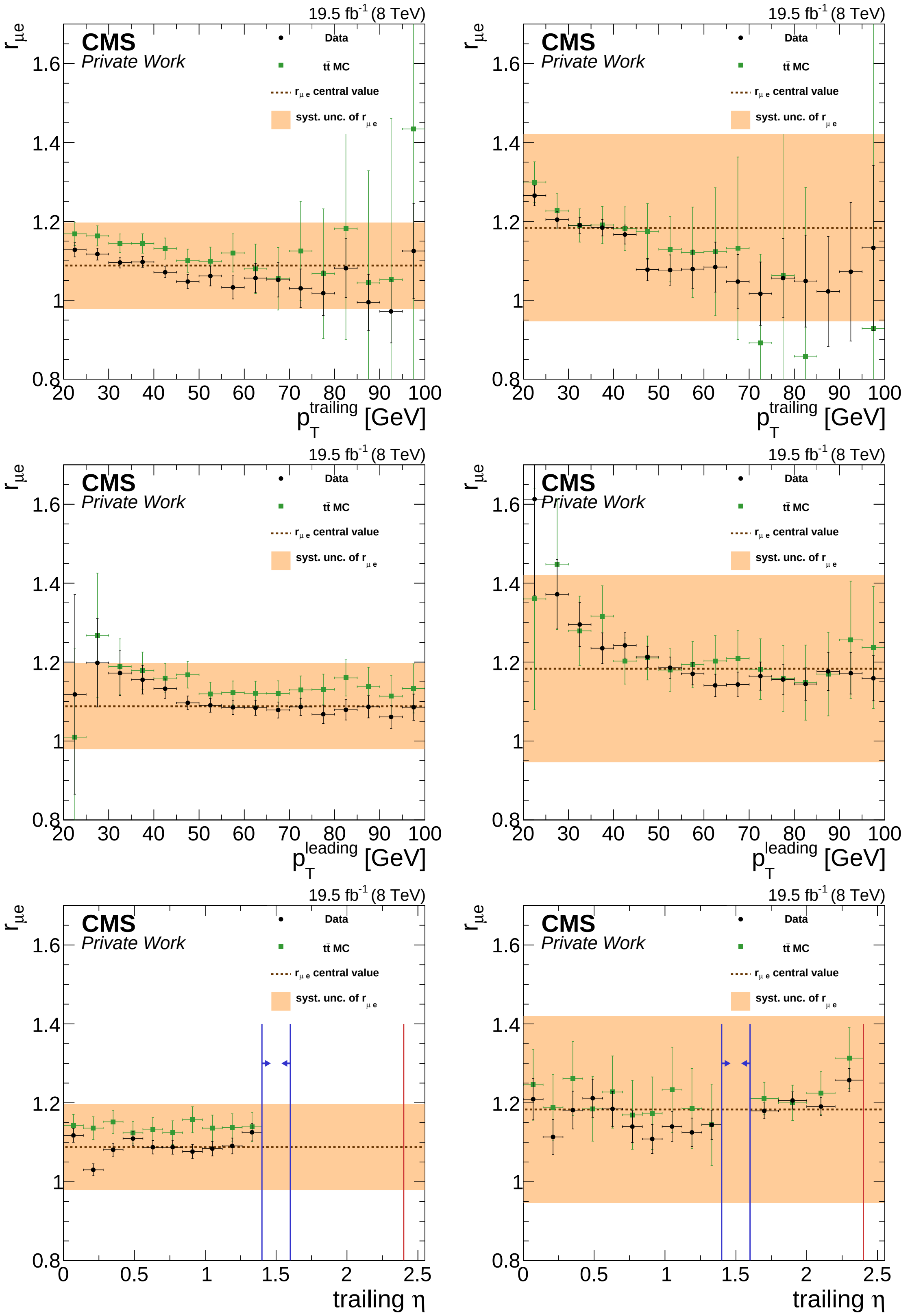

Figure B.1.: Dependencies of $r_{\mu e}$ on the p_{T} of the trailing (top) and the leading (middle) lepton, as well as $|\eta|$ of the trailing lepton (bottom) for the central (left) and forward (right) lepton selection. The results on data are shown in black while $t\bar{t}$ simulation is shown in green. The central value is shown as a brown dashed line while the systematic uncertainty is shown as an orange band.

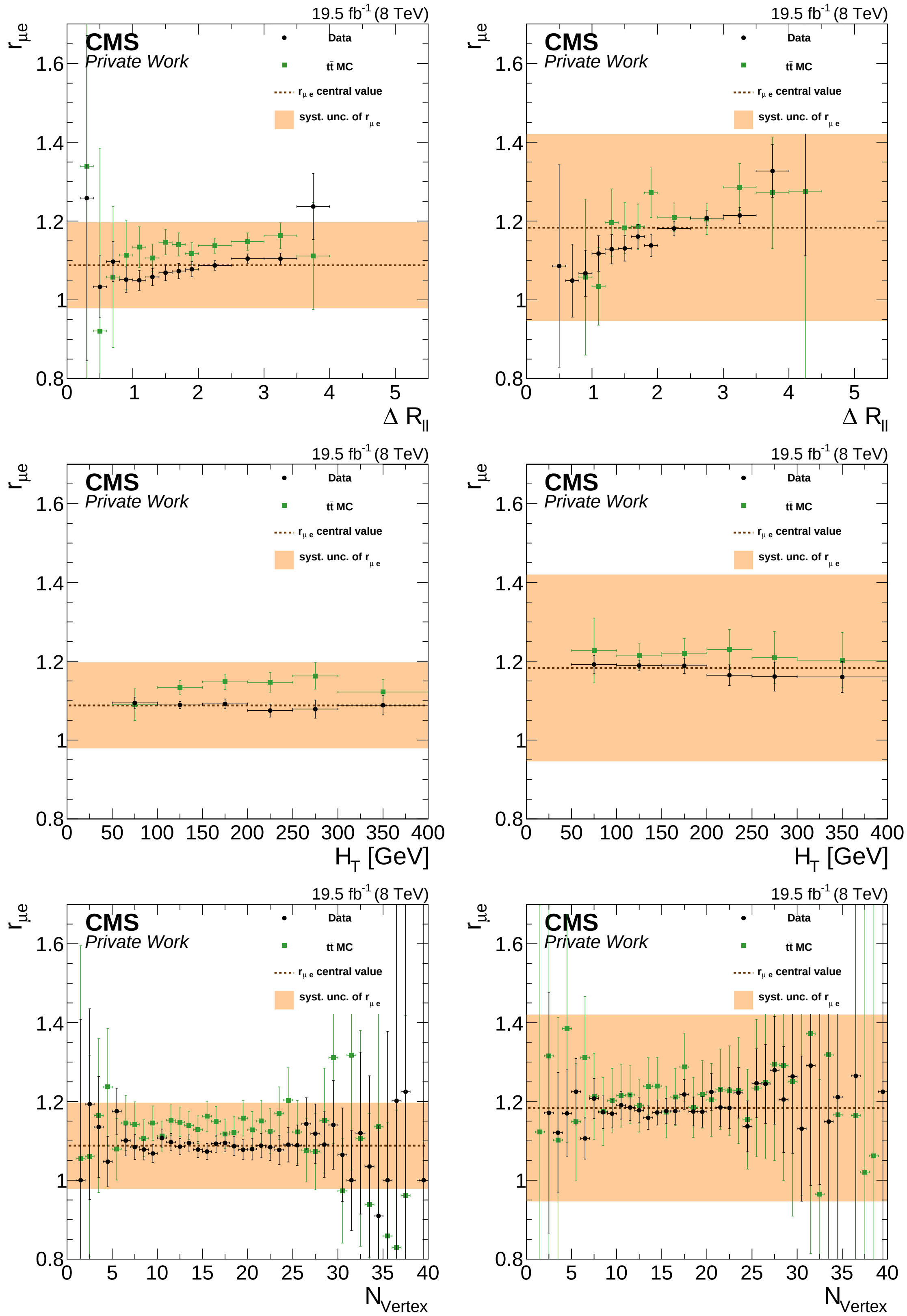

Figure B.2.: Dependencies of $r_{\mu e}$ on $\Delta R(ll)$ (top), H_T (middle), and N_{vertex} (bottom) for the central (left) and forward (right) lepton selection. The results on data are shown in black while $t\bar{t}$ simulation is shown in green. The central value is shown as a brown dashed line while the systematic uncertainty is shown as an orange band.

C. Dependencies of R_T

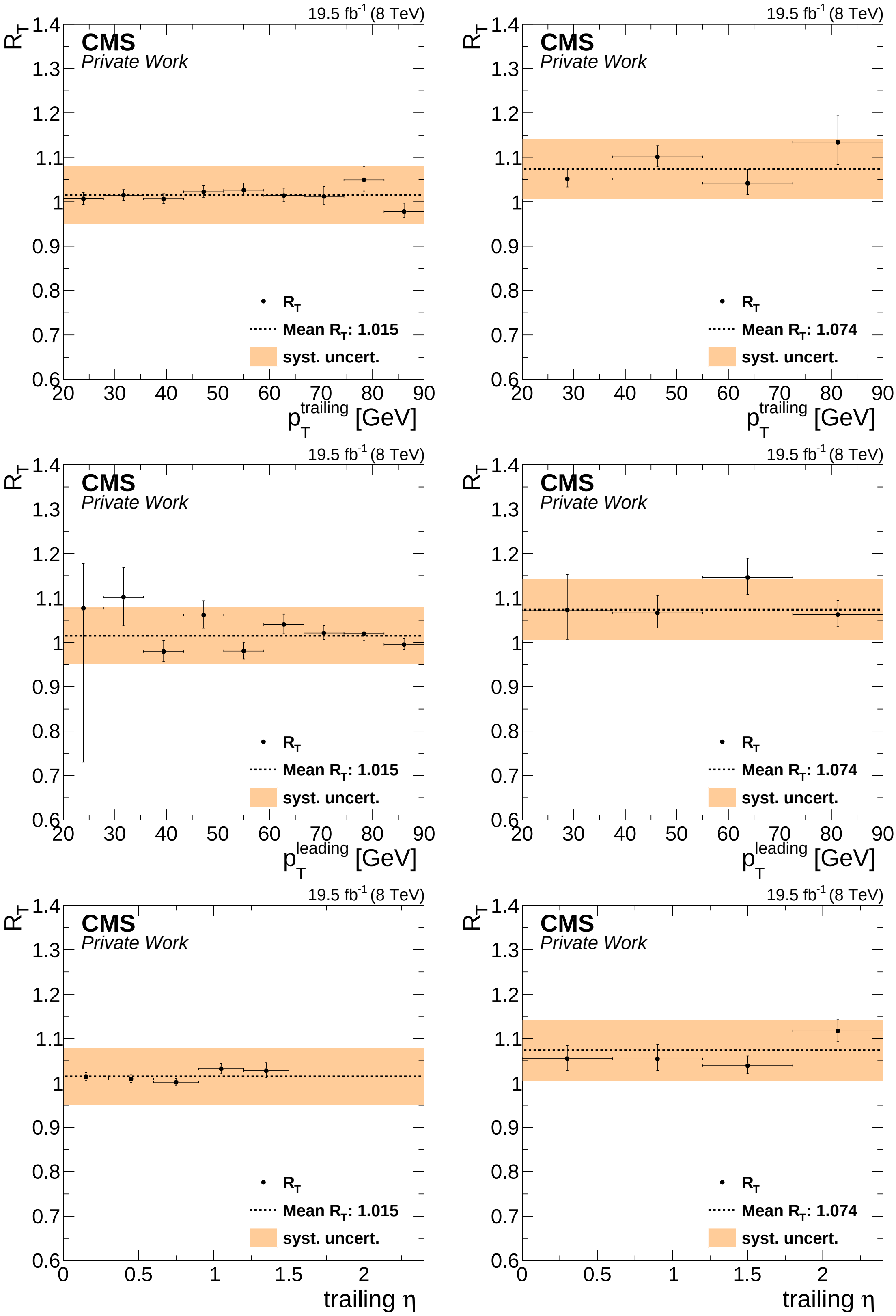

Figure C.1.: Dependencies of R_T on leading lepton p_{T} (top), trailing lepton p_{T} (middle), and $|\eta|$ of the trailing lepton (bottom) for the central (left) and forward (right) lepton selection. The results on data are shown in black. The central value is shown as a black dashed line while the systematic uncertainty is shown as an orange band.

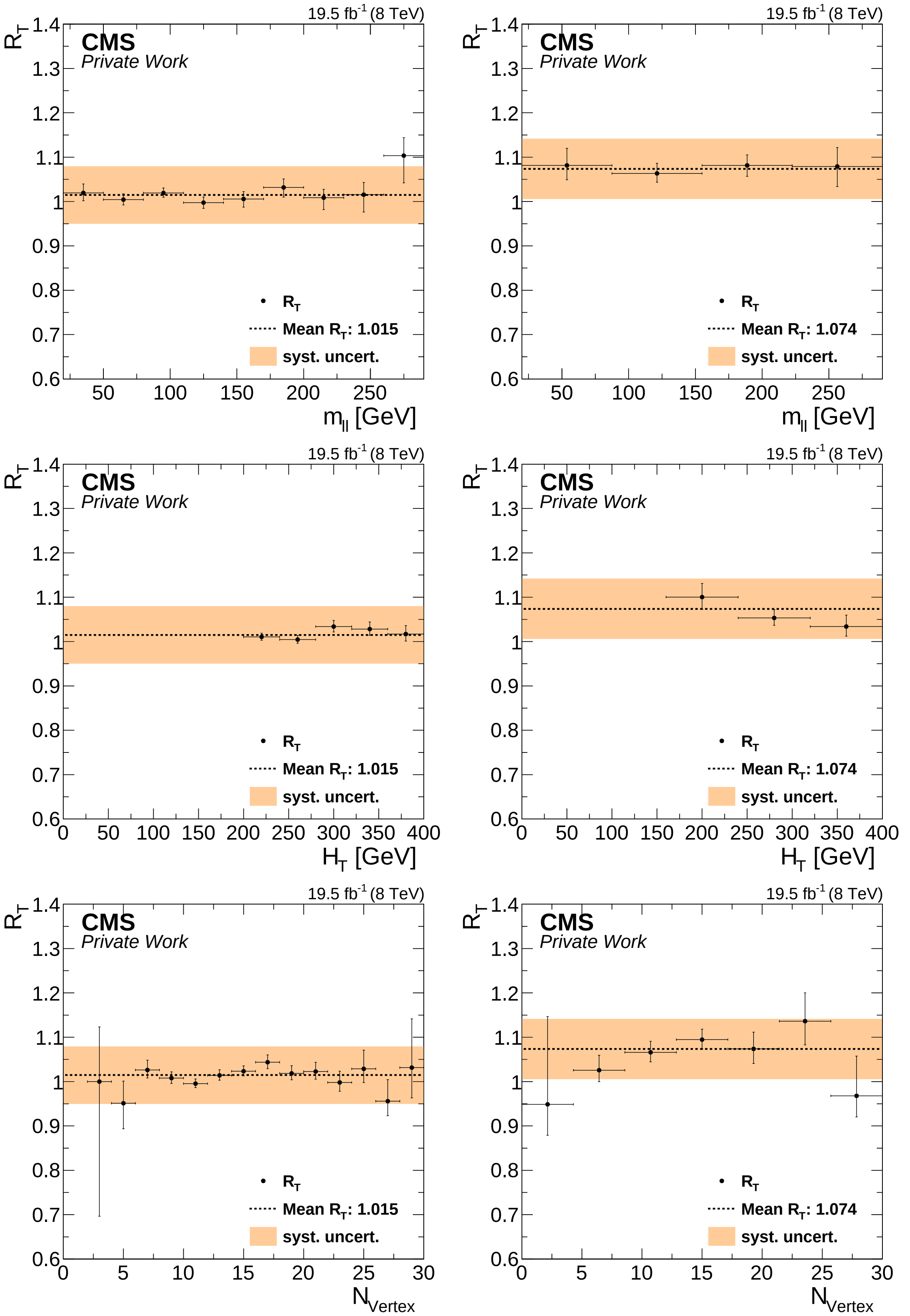

Figure C.2.: Dependencies of R_T on $m_{\ell\ell}$ (top), H_T (middle), and N_{vertex} (bottom) for the central (left) and forward (right) lepton selection. The results on data are shown in black. The central value is shown as a black dashed line while the systematic uncertainty is shown as an orange band.

Bibliography

[1] Lyndon Evans and Philip Bryant. LHC Machine. *Journal of Instrumentation*, 3(08):S08001, 2008.

[2] CMS Collaboration. The CMS experiment at the CERN LHC. *Journal of Instrumentation*, 3(08):S08004, 2008.

[3] ATLAS Collaboration. The ATLAS Experiment at the CERN Large Hadron Collider. *Journal of Instrumentation*, 3(08):S08003, 2008.

[4] LHCb Collaboration. The LHCb Detector at the LHC. *Journal of Instrumentation*, 3(08):S08005, 2008.

[5] Particle kickers. https://cds.cern.ch/record/1706606/. Accessed: 2014-08-06.

[6] CMS Collaboration. Public CMS Luminosity Information. https://twiki.cern.ch/twiki/bin/view/CMSPublic/LumiPublicResults?rev=101. Accessed: 2014-08-06.

[7] CMS detector design. http://cms.web.cern.ch/news/cms-detector-design. Accessed: 2014-08-08.

[8] CMS Collaboration. Electromagnetic calorimeter calibration with 7 TeV data. 2010. CMS Physics Analysis Summary EGM-10-003.

[9] CMS Collaboration. Performance of CMS muon reconstruction in pp collision events at $\sqrt{s}$ = 7 TeV CHECK FOR JOURNAL PUBLICATION. *J. Instrum.*, 7(arXiv:1206.4071. CMS-MUO-10-004. CERN-PH-EP-2012-173):P10002. 81 p, Jun 2012. Comments: Submitted to the Journal of Instrumentation.

[10] W. Adam et al. The CMS high level trigger. *Eur.Phys.J.*, C46:605–667, 2006.

[11] G. Bauer et al. The CMS High Level Trigger System: Experience and Future Development. *Journal of Physics: Conference Series*, 396(1):012008, 2012.

[12] CMS HLT config browser. http://j2eeps.cern.ch/cms-project-confdb-hltdev/browser/. Accessed: 2014-10-09.

[13] Serguei Chatrchyan et al. Description and performance of track and primary-vertex reconstruction with the CMS tracker CHECK FOR JOURNAL PUBLICATION. 2014.

[14] R. Frühwirth. Application of kalman filtering to track and vertex fitting. *Nuclear Instruments and Methods in Physics Research Section A: Accelerators, Spectrometers, Detectors and Associated Equipment*, 262(2.3):444 – 450, 1987.

[15] CMS Software Guide on Iterative Tracking. https://twiki.cern.ch/twiki/bin/

view/CMSPublic/SWGuideIterativeTracking?rev=9. Accessed: 2014-10-11.

[16] CMS Collaboration. Performance of cms muon reconstruction in cosmic-ray events. *Journal of Instrumentation*, 5(03):T03022, 2010.

[17] Particle-flow commissioning with muons and electrons from J/Psi and W events at 7 TeV. Technical Report CMS-PAS-PFT-10-003, CERN, 2010. Geneva, 2010.

[18] S. Baffioni, C. Charlot, F. Ferri, D. Futyan, P. Meridiani, et al. Electron reconstruction in CMS. *Eur.Phys.J.*, C49:1099–1116, 2007.

[19] CMS Collaboration. Review of clustering algorithms and energy corrections in ECAL. *CMS Internal Note IN-10-008*, Mar 2010.

[20] W. Adam, R. Frühwirth, A. Strandlie, and T. Todorov. Reconstruction of electrons with the Gaussian-sum filter in the CMS tracker at the LHC. *Journal of Physics G: Nuclear and Particle Physics*, 31(9):N9, 2005.

[21] Particle-Flow Event Reconstruction in CMS and Performance for Jets, Taus, and MET. Technical Report CMS-PAS-PFT-09-001, CERN, 2009. Geneva, Apr 2009.

[22] Matteo Cacciari, Gavin P. Salam, and Gregory Soyez. The Anti-k(t) jet clustering algorithm. *JHEP*, 0804:063, 2008.

[23] Matteo Cacciari, Gavin P. Salam, and Gregory Soyez. FastJet User Manual. *Eur.Phys.J.*, C72:1896, 2012.

[24] Matteo Cacciari and Gavin P. Salam. Dispelling the N^3 myth for the k_t jet-finder. *Phys.Lett.*, B641:57–61, 2006.

[25] The CMS collaboration. Determination of jet energy calibration and transverse momentum resolution in cms. *Journal of Instrumentation*, 6(11):P11002, 2011.

[26] Serguei Chatrchyan et al. Identification of b-quark jets with the CMS experiment. *JINST*, 8:P04013, 2013.

[27] Results on b-tagging identification in 8 TeV pp collisions. Feb 2013.

[28] The CMS collaboration. Missing transverse energy performance of the cms detector. *Journal of Instrumentation*, 6(09):P09001, 2011.

[29] MET performance in 8 TeV data. Technical Report CMS-PAS-JME-12-002, CERN, Geneva, 2013.

[30] CMS Collaboration. *CMS Physics: Technical Design Report Volume 1: Detector Performance and Software*. Technical Design Report CMS. CERN, Geneva, 2006. There is an error on cover due to a technical problem for some items.

[31] CMS Software Guide on the CMSSW Application Framework. https://twiki.cern.ch/twiki/bin/view/CMSPublic/WorkBookCMSSWFramework?rev=13. Accessed: 2014-

10-26.

[32] Ian Bird. Computing for the large hadron collider. *Annual Review of Nuclear and Particle Science*, 61(1):99–118, 2011.

[33] Worldwide LHC Computing Grid . http://wlcg.web.cern.ch/. Accessed: 2014-10-26.

[34] D. Spiga, S. Lacaprara, W. Bacchi, M. Cinquilli, G. Codispoti, M. Corvo, A. Dorigo, A. Fanfani, F. Fanzago, F. Farina, M. Merlo, O. Gutsche, L. Servoli, and C. Kavka. The cms remote analysis builder (crab). 4873:580–586, 2007.

[35] W Adam, V Adler, B Hegner, L Lista, S Lowette, P Maksimovic, G Petrucciani, S Rappoccio, F Ronga, R Tenchini, and R Wolf. PAT: The CMS Physics Analysis Toolkit. *Journal of Physics: Conference Series*, 219(3):032017, 2010.

[36] R. Brun and F. Rademakers. ROOT - An Object Oriented Data Analysis Framework. *Nucl. Inst. & Meth. in Phys. Res. A*, 389:81–86, 1996. See also http://root.cern.ch/.

[37] A Afaq, A Dolgert, Y Guo, C Jones, S Kosyakov, V Kuznetsov, L Lueking, D Riley, and V Sekhri. The cms dataset bookkeeping service. *Journal of Physics: Conference Series*, 119(7):072001, 2008.

[38] K.A. Olive et al. (Particle Data Group). *Chin. Phys. C*, 38(090001), 2014.

[39] F. Halzen and A. Martin. *Quarks and Leptons: An Introductory Course in Modern Particle Physics*. John Wiley & Sons, 1984.

[40] F.D. Aaron et al. Combined Measurement and QCD Analysis of the Inclusive e+- p Scattering Cross Sections at HERA. *JHEP*, 1001:109, 2010.

[41] J. Pumplin, D.R. Stump, J. Huston, H.L. Lai, Pavel M. Nadolsky, et al. New generation of parton distributions with uncertainties from global QCD analysis. *JHEP*, 0207:012, 2002.

[42] Richard D. Ball, Valerio Bertone, Stefano Carrazza, Christopher S. Deans, Luigi Del Debbio, et al. Parton distributions with LHC data. *Nucl.Phys.*, B867:244–289, 2013.

[43] A.D. Martin, W.J. Stirling, R.S. Thorne, and G. Watt. Parton distributions for the LHC. *Eur.Phys.J.*, C63:189–285, 2009.

[44] Hung-Liang Lai, Marco Guzzi, Joey Huston, Zhao Li, Pavel M. Nadolsky, et al. New parton distributions for collider physics. *Phys.Rev.*, D82:074024, 2010.

[45] V. N. Gribov and L. N. Lipatov. Deep inelastic electron scattering in perturbation theory. *Sov. J. Nucl. Phys.*, 15:438–450, 1972.

[46] G. Altarelli and G. Parisi. Asymptotic Freedom in Parton Language. *Nucl.Phys.*, B126:298, 1977.

[47] Y. L. Dokshitzer. Calculation of the Structure Functions for Deep Inelastic Scattering

and e^+e^- Annihilation by Perturbation Theory in Quantum Chromodynamics. *Sov. Phys. JETP*, 46:641–653, 1977.

[48] Johan Alwall, Michel Herquet, Fabio Maltoni, Olivier Mattelaer, and Tim Stelzer. MadGraph 5 : Going Beyond. *JHEP*, 1106:128, 2011.

[49] Torbjorn Sjöstrand, Stephen Mrenna, and Peter Z. Skands. PYTHIA 6.4 Physics and Manual. *JHEP*, 05:026, 2006.

[50] Stefan Hoeche, Frank Krauss, Nils Lavesson, Leif Lonnblad, Michelangelo Mangano, et al. Matching parton showers and matrix elements. 2006.

[51] Paolo Nason. A new method for combining nlo qcd with shower monte carlo algorithms. *Journal of High Energy Physics*, 2004(11):040, 2004.

[52] Simone Alioli, Paolo Nason, Carlo Oleari, and Emanuele Re. NLO single-top production matched with shower in POWHEG: s- and t-channel contributions. *JHEP*, 0909:111, 2009.

[53] Emanuele Re. Single-top Wt-channel production matched with parton showers using the POWHEG method. *Eur.Phys.J.*, C71:1547, 2011.

[54] Rick Field. Min-Bias and the Underlying Event at the LHC. *Acta Phys.Polon.*, B42:2631–2656, 2011. Tune $Z2^*$ is a variation of Tune $Z2$ described in this reference.

[55] S. Jadach, Z. WaĚ§s, R. Decker, and J.H. KĂźhn. The τ decay library tauola, version 2.4. *Computer Physics Communications*, 76(3):361 – 380, 1993.

[56] S. Agostinelli et al. GEANT4: A Simulation toolkit. *Nucl.Instrum.Meth.*, A506:250–303, 2003.

[57] S Abdullin, P Azzi, F Beaudette, P Janot, A Perrotta, and the CMS Collaboration. The fast simulation of the cms detector at lhc. *Journal of Physics: Conference Series*, 331(3):032049, 2011.

[58] S. et al Chatrchyan. Measurement of the $t\bar{t}$ production cross section in the dilepton channel in pp collisions at $\sqrt{s} = 8$ TeV. *Journal of High Energy Physics*, 2014(2), 2014.

[59] Ye Li and Frank Petriello. Combining QCD and electroweak corrections to dilepton production in FEWZ. *Phys.Rev.*, D86:094034, 2012.

[60] John M. Campbell, R. Keith Ellis, and Ciaran Williams. Vector boson pair production at the LHC. *JHEP*, 1107:018, 2011.

[61] Nikolaos Kidonakis. Differential and total cross sections for top pair and single top production. pages 831–834, 2012.

[62] J. Alwall, R. Frederix, S. Frixione, V. Hirschi, F. Maltoni, O. Mattelaer, H.-S. Shao, T. Stelzer, P. Torrielli, and M. Zaro. The automated computation of tree-level and next-to-leading order differential cross sections, and their matching to parton shower

simulations. *Journal of High Energy Physics*, 2014(7), 2014.

[63] M.V. Garzelli, A. Kardos, C.G. Papadopoulos, and Z. Trocsanyi. t $\bar{t}$ W^{+-} and t $\bar{t}$ Z Hadroproduction at NLO accuracy in QCD with Parton Shower and Hadronization effects. *JHEP*, 1211:056, 2012.

[64] Measurement of the inclusive top-quark pair + photon production cross section in the muon + jets channel in pp collisions at 8 TeV. Technical Report CMS-PAS-TOP-13-011, CERN, Geneva, 2014.

[65] L Tuura, A Meyer, I Segoni, and G Della Ricca. Cms data quality monitoring: Systems and experiences. *Journal of Physics: Conference Series*, 219(7):072020, 2010.

[66] K Rose. Deterministic annealing for clustering, compression, classification, regression, and related optimization problems. *Proceedings of the IEEE*, 8, 1998.

[67] R Frühwirth, Wolfgang Waltenberger, and Pascal Vanlaer. Adaptive Vertex Fitting. Technical Report CMS-NOTE-2007-008, CERN, Geneva, Mar 2007.

[68] Serguei Chatrchyan et al. Search for physics beyond the standard model in events with a Z boson, jets, and missing transverse energy in pp collisions at $\sqrt{s} = 7$ TeV. *Phys.Lett.*, B716:260–284, 2012.

[69] CMS and ATLAS Collaborations. Procedure for the LHC Higgs boson search combination in Summer 2011. *CMS-NOTE-2011-005, ATL-PHYS-PUB-2011-011*.

[70] Christian Schomakers. Studies of simplified models and projection to $\sqrt{s}$=13 TeV for the CMS SUSY dilepton edge search.

[71] Wim Beenakker, R. Höpker, M. Spira, and P. M. Zerwas. Squark and gluino production at hadron colliders. *Nucl. Phys. B*, 492:51, 1997.

[72] Anna Kulesza and L. Motyka. Threshold resummation for squark-antisquark and gluino-pair production at the LHC. *Phys. Rev. Lett.*, 102:111802, 2009.

[73] Anna Kulesza and L. Motyka. Soft gluon resummation for the production of gluino-gluino and squark-antisquark pairs at the LHC. *Phys. Rev. D*, 80:095004, 2009.

[74] Wim Beenakker, Silja Brensing, Michael Krämer, Anna Kulesza, Eric Laenen, and Irene Niessen. Soft-gluon resummation for squark and gluino hadroproduction. *JHEP*, 12:041, 2009.

[75] Wim Beenakker, Silja Brensing, Michael Krämer, Anna Kulesza, Eric Laenen, Leszek Motyka, and Irene Niessen. Squark and gluino hadroproduction. *Int. J. Mod. Phys. A*, 26:2637, 2011.

[76] Michael Krämer, Anna Kulesza, Robin van der Leeuw, Michelangelo Mangano, Sanjay Padhi, Tilman Plehn, and Xavier Portell. Supersymmetry production cross sections in pp collisions at $\sqrt{s} = 7$ TeV. 2012.

[77] CMS Collaboration. CMS Luminosity Based on Pixel Cluster Counting - Summer 2013 Update. *CMS Physics Analysis Summary*, pages CMS–PAS–LUM–13–001 (2013).

[78] Sergey Alekhin, Simone Alioli, Richard D. Ball, Valerio Bertone, Johannes Blumlein, et al. The PDF4LHC Working Group Interim Report. 2011.

[79] Michiel Botje, Jon Butterworth, Amanda Cooper-Sarkar, Albert de Roeck, Joel Feltesse, et al. The PDF4LHC Working Group Interim Recommendations. 2011.

[80] Serguei Chatrchyan et al. Search for top-squark pair production in the single-lepton final state in pp collisions at $\sqrt{s} = 8$ TeV. *Eur .Phys. J. C*, 73:2677, 2013.

[81] M. Oreglia. A study of the reactions $\psi' \to \gamma\gamma\psi$. *Ph.D. thesis, Stanford University, SLAC Report SLAC-R-236*, 1980.

[82] Serguei Chatrchyan et al. Search for new physics in events with opposite-sign leptons, jets, and missing transverse energy in pp collisions at $\sqrt{s} = 7$ TeV. *Phys. Lett. B*, 718:815, 2013.

[83] Kyle S. Cranmer. *kernel estimation in high-energy physics.* Comput.Phys.Commun., *136:98–207, 2001.*

[84] S. S. Wilks. The large-sample distribution of the likelihood ratio for testing composite hypotheses. The Annals of Mathematical Statistics, *9(1):60–62, 03 1938.*

[85] Eilam Gross and Ofer Vitells. Trial factors for the look elsewhere effect in high energy physics. The European Physical Journal C, *70(1-2):525–530, 2010.*